Theory and Simulation of Texture Selection Mechanisms in Mesophase Carbon Fibers

by

Dinesh Sharma

Department of Chemical Engineering
Mcgill University, Montreal, Canada

Date: January, 2003

A Thesis submitted to the Faculty of Graduate Studies and Research in Partial fulfillment of the requirements for the degree of Master of Science

National Library
of Canada

Acquisitions and
Bibliographic Services

395 Wellington Street
Ottawa ON K1A 0N4
Canada

Bibliothèque nationale
du Canada

Acquisisitons et
services bibliographiques

395, rue Wellington
Ottawa ON K1A 0N4
Canada

Your file Votre référence
ISBN: 0-612-88365-5
Our file Notre référence
ISBN: 0-612-88365-5

Canada

FOR MY PARENTS

Abstract

Carbon fiber precursors are spun from carbonaceous mesophases using standard melt spinning techniques. These melt spun carbon fibers exhibit a multitude of cross sectional fiber textures. The two widely reported textures in literature are planar radial (PR) and planar polar (PP). This thesis uses a mesoscopic model, based on the classical Landau de-Gennes theory of liquid crystals and adapted here to carbonaceous mesophases, to study the steady state and transient phenomena involved in the mesophase carbon fiber texture formation. The model is successfully able to capture the microstructure and the formation of the PR and PP textures. A phase diagram for classical PR and PP textures has been constructed cylindrical carbon fibers in terms of temperature and fiber radius, thus estabilishing the processing conditions and geometric factors that lead to the selection of these textures. The multi-path formation process of the planar polar texture through defect splitting, direct planar polar formation, and defect annihilation has been thoroughly characterized. A detailed analysis of defect core structure for defects of strengths $s = +1$ and $s = +1/2$ has be undertaken. The effect of various parameters namely temperature, elastic anisotropy, and fiber radii on the defect core structures of commonly observed fiber textures has been studied. The model is well suited for studying the defect core textures which are in the nano range and could be applied to the new emerging field of nano fibers. The results of this thesis provide us with knowledge for optimization and control of mesophase carbon fiber texture, and lay the ground work for the study of nano scale phenomena in nano fibers.

Résumé

Les fibres de carbone sont filées à partir de mésophases carbonées utilisant les techniques standard de filage à chaud. En coupe, ces fibres de carbone filées fondues exhibent une multitude de textures. Les deux textures les plus abondamment reportée dans la littérature sont: la planaire radiale PR et la planaire polaire PP. Dans cette thèse un modèle mésoscopique basé sur la théorie classique des cristaux liquides de Landau-de Gennes, et adaptée aux mésophases carbonées, est utilisé pour étudier les phénomènes d'états d'équilibres et transitoires impliqués dans la formation des textures des fibres de carbone. Un diagramme de phase pour les textures classiques PR et PP des mésophases carbonées cylindriques a été construit en fonction de la température et du diamètre de la fibre, établissant de ce fait les conditions de traitement et les facteurs géométriques menant à la sélection des textures. Le procédé de formation à trajet multiple de la texture planaire polaire à été complètement caractérisé dans les cas d'un dédoublement de défauts, d'une formation directe, et d'une annihilation de défauts. Une analyse détaillée a été menée sur la structure du noyau des défauts d'ordre s=+1 et s= +1/2. L'effet de paramètres tel que la température, l'anisotropie élastique, et le rayon des fibres a été étudié pour la texture des défauts couramment observés dans les fibres. Le modèle est bien adapté pour l'étude de la texture des défauts qui se trouve à l'échelle nanoscopique et pourrait être de ce fait appliqué au secteur émergent des fibres nanoscopiques. Les résultats de cette thèse nous fournissent des connaissances pour l'optimisation et le contrôle des textures des mésophases de fibre de carbone et établie les fondations d'une étude texturale sur les fibres nanoscopiques.

Acknowledgements

I wish to express my sincere gratitude and appreciation to my thesis advisor, Professor A.D. Rey for his encouragement, guidance, patience and active interest throughout the course of this project. His guidance and encouragement were indispensable in the completion of this thesis. I will always be indebted to him for what I have learned, not only in science but also regarding dedication and perseverence.

I would like thank Dr. Arvinder Pal Singh for his support and lively discussions during the early part of this project. Extreme gratitude is also felt towards Ms. Marika Asimakopulos for her moral support and for putting up with all my erratic moods. Additional thanks to the entire numerical simulation research group, Gino De Luca, Susanta Das, Ae-Gyeong Cheong, Luiz Lima, and Dana Radu for their frequent encouragement and good cheer. Of course, many thanks to my parents and siblings for believing in me and their unconditional love. I would also like to thank all those people that have not been mentioned but have had a hand in completion of this project.

Finally, I would like to thank the Donors of Petroleum Research Fund (PRF), administered by the American Chemical Society, for support of this research.

Table of Contents

List of Symbols

Upper Case Letters

S	Uniaxial scalar order parameter
S_{ini}	Uniaxial scalar order parameter for initial condition
S_{eq}	Equilibrium scalar order parameter for a given temperature
P	Biaxial scalar order parameter
P_{ini}	Biaxial scalar order parameter for initial condition
$\mathbf{Q}$	Tensor order parameter
$\mathbf{Q}_{\mathrm{ini}}$	Tensor order parameter for initial condition
A, B, C	Temperature dependent phenomenological coefficients
K_{11}, K_{22}, K_{33}	Frank elastic constants
F_{D}	Frank distortion energy
L_1, L_2, L_3	Landau coefficients
F^{h}	Homogeneous (Phase Transition) free energy contribution
F^{e}	Deformation (Elastic) free energy contribution
T	Absolute temperature
T^*	Reference temperature just below the nematic-isotropic phase transition
U	Nematic potential
$\overline{\mathrm{D}_{\mathrm{r}}}$	Rotational diffusivity coefficient
D_{r}	Isotropic diffusivity
$\widetilde{L}_2$	Dimensionless elastic anisotropy
R	Ratio of short-range order elasticity to long range order elasticity

H	Fiber radius
$\mathrm{L_e}$	External length scale
$\mathrm{L_i}$	Internal length scale
R	Weighted residual
$\underline{\underline{J}}$	Jacobian matrix
U_i	Lumped unknown coefficient
W	Energy of deformation of a defect of strength +1
W_c	Core energy of a defect of strength +1
$\mathscr{F}_{12}$	Attractive force per unit length between two wedge disclinations of +1/2 strength

Lower Case Letters

$\boldsymbol{s}$	Strength of a defect
$\boldsymbol{d}$	Dimensionality of a defect
$\mathbf{n}, \mathbf{m}, \mathbf{l}$	Orthogonal triad of vectors representing eigenvectors of **Q**
$\mathbf{n}_{\mathrm{ini}}, \mathbf{m}_{\mathrm{ini}}, \mathbf{l}_{\mathrm{ini}}$	Orthogonal triad of vectors representing eigenvectors of **Q** for initial condition
$\mathbf{n}_{\mathrm{bc}}, \mathbf{m}_{\mathrm{bc}}, \mathbf{l}_{\mathrm{bc}}$	Orthogonal triad of vectors representing eigenvectors of **Q** for boundary condition
$\mathbf{a}$	Vector denoting unit normal to the discs
k	Boltzman's constant
c	Number density of discs
t	Time
$\tilde{\mathrm{t}}$	Dimensionless time
u_{a}	Approximate solution to the differential equation

u_j	Unknown coefficients
w_i	Weight function
v, w	Vector quantities
$\bar{u}_j$	Nodal values of u
r	Fiber radius
r_c	Defect core radius
d	Distance between two wedge disclinations of +1/2 strength
(x, y, z)	Cartesian coordinate system
i, j	Summation indices

Greek Letters

$\lambda_n, \lambda_m, \lambda_l$	Three eigenvalues of tensor **Q** corresponding to **n**, **m**, **l**
δ	Unit Tensor
η	Viscosity of the material
$\gamma(\mathbf{Q})$	Rotational Viscosity Coefficient
ξ	Characteristic defect core length scale
τ_i	Internal time scale
τ_e	External time scale
α	Scalar quantity
φ_j	Global test and trial functions
(ξ, η)	Local orthogonal coordinate system for isoparametric mapping
ζ	Small thermal fluctuations in orientation
β^2	Biaxiality parameter

List of Figures

Chapter 1

Introduction

1.1 Thesis Motivation

Materials are probably more deep-seated in our culture than most of us realize. Transportation, housing, clothing, communication, recreation and food production – virtually every segment of our everyday lives is influenced to one degree or another by materials. Material engineers use the understanding of structure-property relations to produce better materials with pre-determined properties. Today we are consistently on the look out for better materials to replace traditional materials. Carbon fibers belong to such a class of material, which are becoming increasingly popular for their desirable properties.

High performance carbon fibers possess exceptional mechanical and thermal transport properties. They exhibit ultrahigh Young's modulus; low density; extremely high thermal conductivity; and negative thermal coefficient of expansion. They are increasingly being employed in the construction of next generation composite materials for aerospace, electronics and the automotive industries. The superior set of product property profile of carbon fibers depends on their microstructure that evolves during their spinning [1, 2] and is a strong function of the operating conditions, geometry and material precursor properties. There has been a great interest in understanding the texture evolution of carbon fibers in response to various parametric conditions. This thesis is one such endeavor-specifically to understand the texture evolution of mesophase pitch-based carbon fibers.

1.2 Carbon Fibers

There are three different types of commercial carbon fibers manufactured from three different precursor materials. They are namely rayon carbon fibers, acrylic carbon fibers, and mesophase pitch-based carbon fibers [2,3]. The rayon carbon fibers have relatively low tensile strength and low Young's modulus, and have been used mainly as composites designed for use in rocket and space shuttle applications. The acrylic carbon fibers, commonly known as PAN-based (poly-acrylonitrile) carbon fibers, are copolymers containing acrylonitrile in excess of 85% along with other co-monomers, which are used to improve processability. The PAN-based carbon fibers have high strength, high modulus and semi-conducting properties and are used in a wide variety of applications [3-5]. Pitch-based carbon fibers can be manufactured from two different states of the same precursor material (coal or petroleum pitches): the liquid crystalline state or mesophase, and the isotropic state. The isotropic pitch-based carbon fibers have low modulus and strength. The mesophase pitch-based carbon fibers have ultrahigh strength and modulus, and can be used in the same applications as PAN-based carbon fibers. Figure 1 shows thermal conductivity and electrical resistivity for a number of metals and Amoco series of mesophase pitch-based (suffix 'P') and PAN-based carbon fibers [4]. The thermal conductivity of mesophase carbon fibers is considerably higher than that of copper and PAN carbon fibers. These high values of thermal conductivity are due to the inherent graphitic crystallinity in the well-ordered textures of the mesophase carbon fibers. The thermal conductivity of mesophase carbon fibers is due to phonon conduction as opposed to electronic conduction [5] and is influenced by various factors such as: high degree of crystallinity, large size of crystallites etc. PAN-based carbon fibers cannot exhibit high values of thermal conductivity due to their fibrillar microstructure. Moreover, PAN-based carbon fibers, due to their fibrillar nature, are unable to develop any extended graphitic structure, hence their modulus is considerably less than the theoretical value, a limit which is nearly achieved by mesophase carbon fibers, as shown in Figure 2.

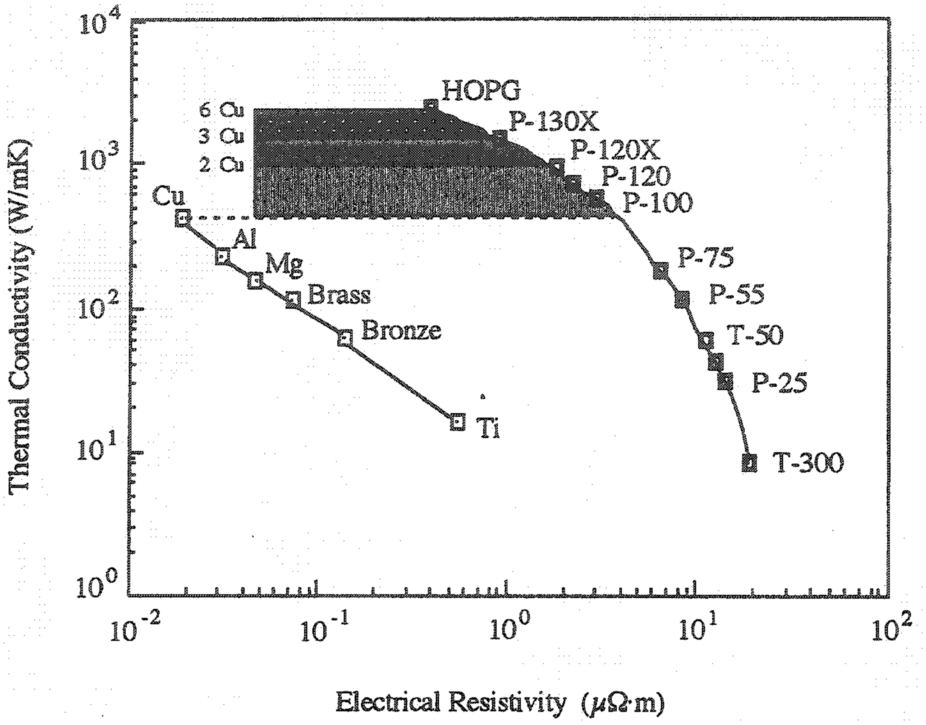

Figure 1: Thermal conductivity versus electrical resistivity product property phase plane for various metals and carbon fibers. The thermal conductivity of mesophase carbon, P-130X, P-120X etc., is considerably higher than that of the most conductive metals like copper. Adapted from [4].

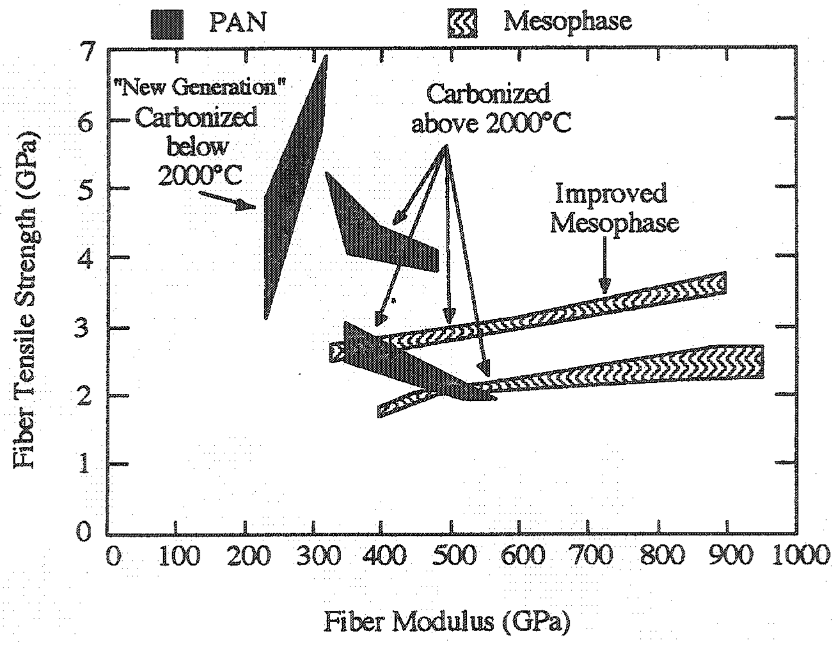

Figure 2: Tensile strength versus modulus of elasticity (stiffness) product property phase plane of various carbon fibers. The PAN-based carbon fibers have considerably higher strength than the mesophase carbon fibers, however the former lack considerably in terms of stiffness. The stiffness of mesophase carbon fibers reaches the theoretical limits of pure graphite. Adapted from [6].

1.3 Carbonaceous Mesophases (Mesophase Pitches)

Raw pitch, a high molecular weight by-product formed during petroleum or coal refining operations, is composed of large polynuclear aromatic hydrocarbon molecules with molecular weights approximately near 2000 [7]. The CMs or MPs are employed as low cost precursor materials in the manufacture of high performance mesophase carbon fibers [8]. There are currently three main processes that are used to produce spinnable MPs. The classical way is the liquid phase pyrolysis of coal tar or petroleum pitches. The second more recent process is the catalytical polymerization of pure aromatic hydrocarbons, such as naphthalene. The third technique, developed recently by Hutchenson et al. [9], uses a solvent in its supercritical state to extract mesophase fractions from isotropic pitches.

Figure 3 shows the thermodynamic and structural changes brought about by heating a non-volatile organic compound, such as coal or petroleum pitch, in the absence of air. The organic component melts in heating and becomes an isotropic pitch or liquid. As the temperature rises over 350^{o} C, optically anisotropic spheres known as spherules, appear in the isotropic matrix [10,11]. The formation of the carbonaceous mesophase follows a nucleation and growth process, typical of metastable thermodynamic systems. Attractive forces among the spherules give rise to droplet coalescence and overall growth of the mesophase. As hydrogenative polymerization reactions continue, the molecules get larger and at an average molecular weight of 2000, they are sufficiently large and flat to favour the formation of a liquid crystalline discotic nematic phase called carbonaceous mesophase or simply mesophase pitch. The mesophase transformation was first observed by Brooks and Taylor [12] as an intermediate phase of spherules with a mosaic structure. The droplets or spherules are easily observed because of their optical anisotropy (figure 4). Selected area electron diffraction patterns indicate that each mesophase spherule possesses at its center a single direction of preferred orientation. The characteristic mesophase mechanism that are involved in establishing the mesophase morphology are spherule precipitation, coalescence of spherules to form a bulk mesophase, and distortion of mesophase by mechanical deformations.

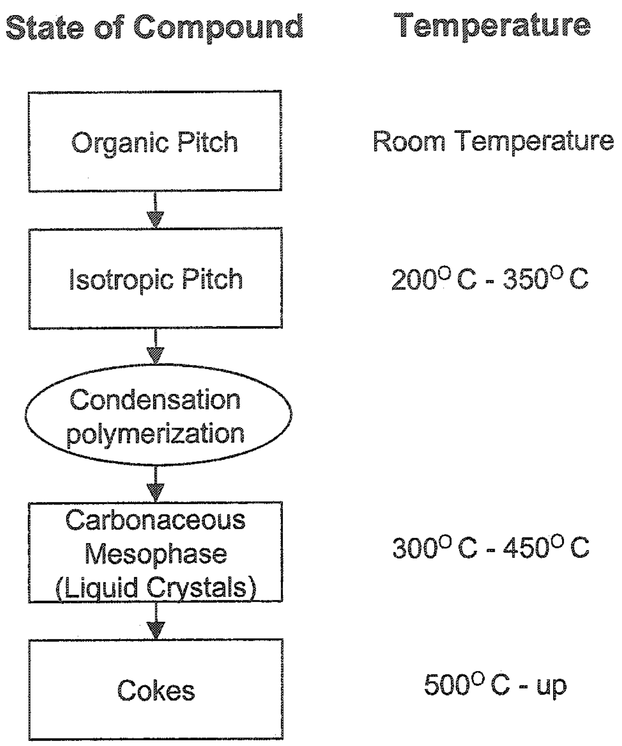

Figure 3: Changes in the non-volatile organic compounds like coal or petroleum pitches brought about by heating in the absence of air. Adapted from [13].

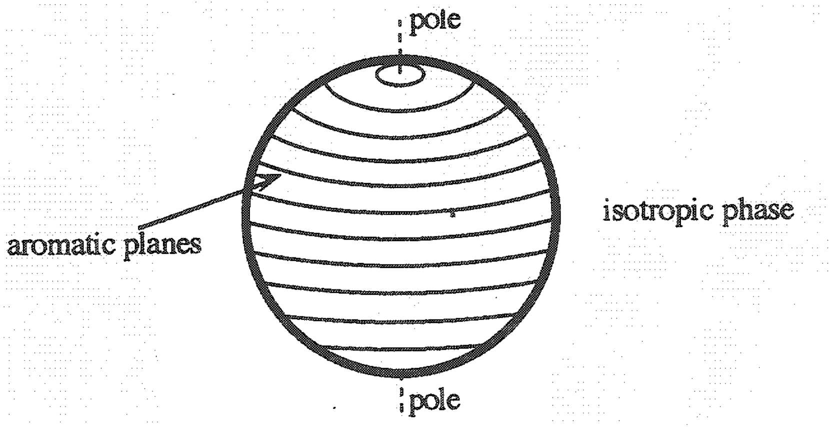

Figure 4: Lamellar structure of mesophase spherule before coalescence. The aromatic planes are normal to the spherule surface. The spherule grows as the aromatic molecules fuse together due to hydrogenative polymerization. Adapted from [12].

Chwastiak and Lewis [14] modified the above simplistic heat soaking process for isotropic pitches by propelling an inert gas into the reaction vessel. An alternative heat soaking mechanism developed by Dienfendorf and Riggs [15] used solvents like benzene and toluene to extract the high molecular components from the isotropic pitch. The extracted portion was then polymerized for only ten minutes at relatively lower temperatures, 230°C to 400°C to yield a 75% to 100% anisotropic pitch. The primary advantage of heat soaking and solvent extraction of natural petroleum pitches is the inexpensive nature of the feedstock, however there are inherent disadvantages as well. First, natural pitch contains heavy impurities that accumulate in the high-density mesophase, which in turn have detrimental effects on the final properties of carbon fibers. Moreover, the composition of a natural isotropic pitch varies depending on the crude oil composition; therefore the properties of the resulting MP also tend to be highly variable. Thirdly, the MPs exhibit broad molecular weight distribution, which hinders spinning.

The other two techniques, namely supercritical fluid extraction and catalytic polymerization, were an effort to alleviate the above mentioned problems. Hutchenson et al. [9] have reported that supercritical fluid extraction, using supercritical toluene, can be employed to fractionate pitches. By continuously varying pressure and/or temperature, thereby changing the solvent strength, selective pitch fractions of relatively narrow molecular weight distribution can be isolated in a cascading process. Such a process offers the potential of producing a uniform product from an ever changing raw material. Catalytic polymerization of synthetic precursors like naphthalene, anthracene, and methyl-naphthalene etc offers another alternative for pitch manufacture [16]. For example, naphthalene can be polymerized in an autoclave with the aid of "super catalyst" HF/BF_3, at temperatures ranging from 260°C to 300°C and under pressures from 2.1 MPa to 3.1 MPa for approximately 4 hours. The contents of the autoclave are heated to 340°C and purged with nitrogen to distill off the catalyst, the unreacted monomer, and other volatile components, thereby leaving 100% anisotropic pitch in the autoclave. However, the resulting mesophase pitches, derived from all of these processes, consist of aromatic disc-like molecules exhibiting discotic liquid crystalline properties. The carbonaceous mesophase consists of disc-like molecules that display long-range orientational order, such that the molecules lie approximately parallel to each other with no point-to-point registry between adjacent molecules. The orientation of each molecule may be defined by its unit normal. A schematic model of carbonaceous mesophase stacking in the bulk is given in figure 5. The model suggests that the stacking size and the possible shapes of the disc-like molecules maybe quite irregular and that material may have vacant sites and holes.

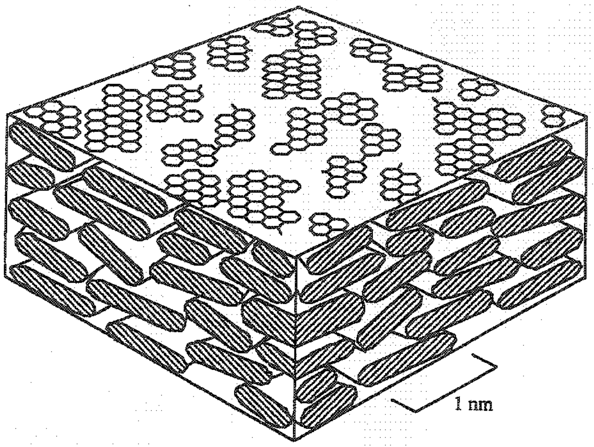

Figure 5: Schematic model representing stacking arrangement of polyaromatic molecules in carbonaceous mesophases or mesophase pitches. The disc-shaped molecules lie more or less parallel to each other. Adapted from [2].

Although the degree of symmetry is the same for a discotic (disc-like) nematic and a conventional rod-like nematic, yet the molecular geometrical differences, for the discotic (rod-like) nematics the axis of symmetry is normal (along) to the long dimension, have important consequences on optical properties, response to external fields such as mechanical stresses, electrical and magnetic fields etc. In this dissertation we focus on the distinguishing microstructural textures of discotic mesophases.

The main microstructural features of the carbonaceous mesophases (uniaxial discotic nematic liquid crystals) are captured by the director $\mathbf{n}$, and the degree of orientation order S. The director $\mathbf{n}$ is a unit vector that describes the unit average molecular orientation of the unit normals to the disc-like molecules, and the degree of orientation order (alignment) S is the measure of the average molecular alignment along $\mathbf{n}$. In discotic nematics the unit normals are more or less aligned in the direction of $\mathbf{n}$. The dispersion of molecular orientation along $\mathbf{n}$ is captured by the magnitude of S ($-\frac{1}{2} \leq S \leq 1$): when $S = 0$ the phase is isotropic, when $S = 1$ all the molecules are perfectly aligned along the direction of $\mathbf{n}$. For normal discotic nematics the order parameter S is restricted to the range $0 \leq S \leq 1$. The basic rheological and the morphological phenomena have to at least include a description of spatial-temporal changes of S and $\mathbf{n}$. In certain circumstances, uniaxiality may be lost and a more complex description that includes biaxial ordering may be necessary.

1.4 Melt Spinning of Carbonaceous Mesophases

Mesophase carbon fibers are manufactured from mesophase pitch in mainly three steps: melt spinning, stabilization and heat treatment. In the melt spinning step, the fibers are drawn using the molten mesophase pitch to achieve preferred orientation in the as-spun fibers. The texture of the fiber depends on a number of variables such as the composition of the pitch, the spin temperature, whether or not the melt pool is stirred, the geometry of the orifice, etc [17, 18]. Figure 6 provides one indication of the effect of the spinning temperature on MP carbon fiber texture and figure 7 shows the effect of spinning temperature on the carbon fiber properties. There are similar strong correlations between the other processing variables and the fiber textures and properties. Thus it is important to understand these underlying correlations to optimize the physical properties of carbon fibers. Figure 8 shows the three steps employed in the spinning of molten mesophase into carbon fibers.

1.4.1 Melt Spinning

A conventional high-speed melt spinning process used for many thermoplastic polymers is employed to convert palletized mesophase pitch into fibers. Normally, an extruder melts and pressurizes the pitch, and pumps it through the spin pack. The molten pitch is filtered before being extruded through a multi-holed spinneret. The pitch is subjected to high extensional and shear stresses as it approaches and flows through the spinneret capillaries. The associated flow-induced torques tend to orient the disc-shaped molecules in a regular transverse pattern.

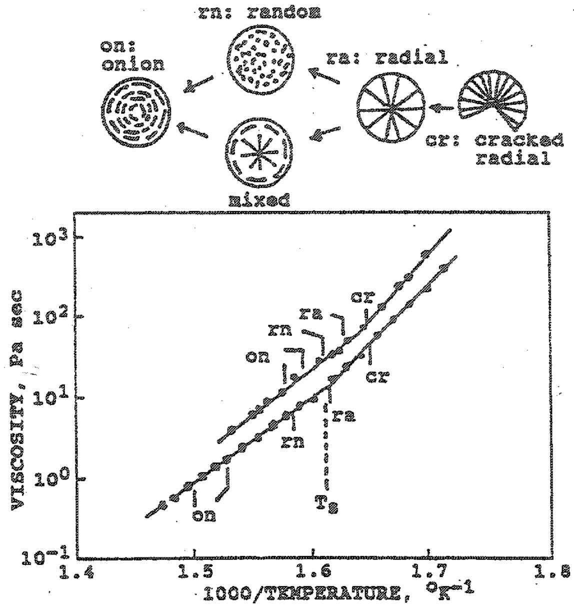

Figure 6: Variation of mesophase fiber texture with melt spinning temperature for two different pitches. Adapted from [2].

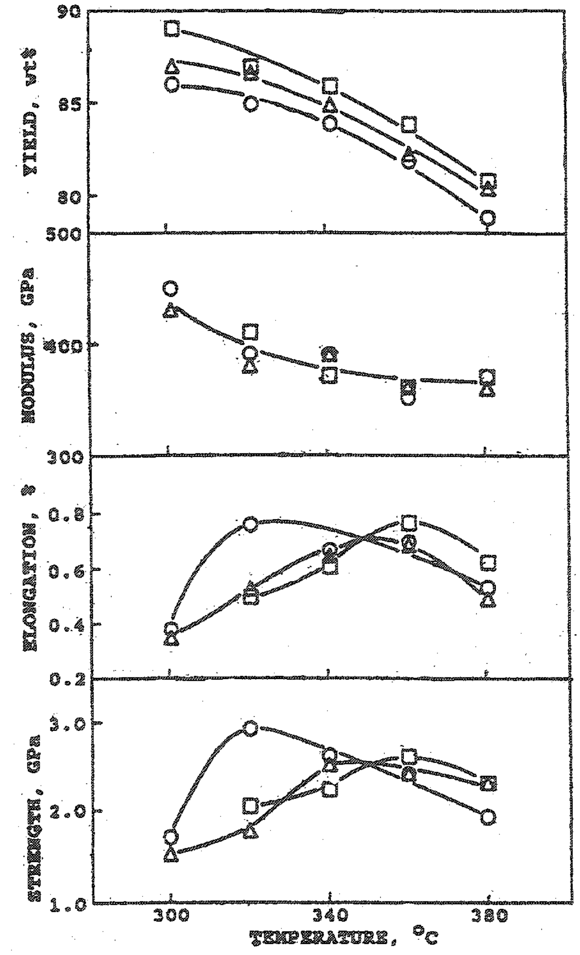

Figure 7: Effect of heating rate and final temperature with a 15 minute soak in air during stabilization on the carbon yield and mechanical properties. Adapted from [2].

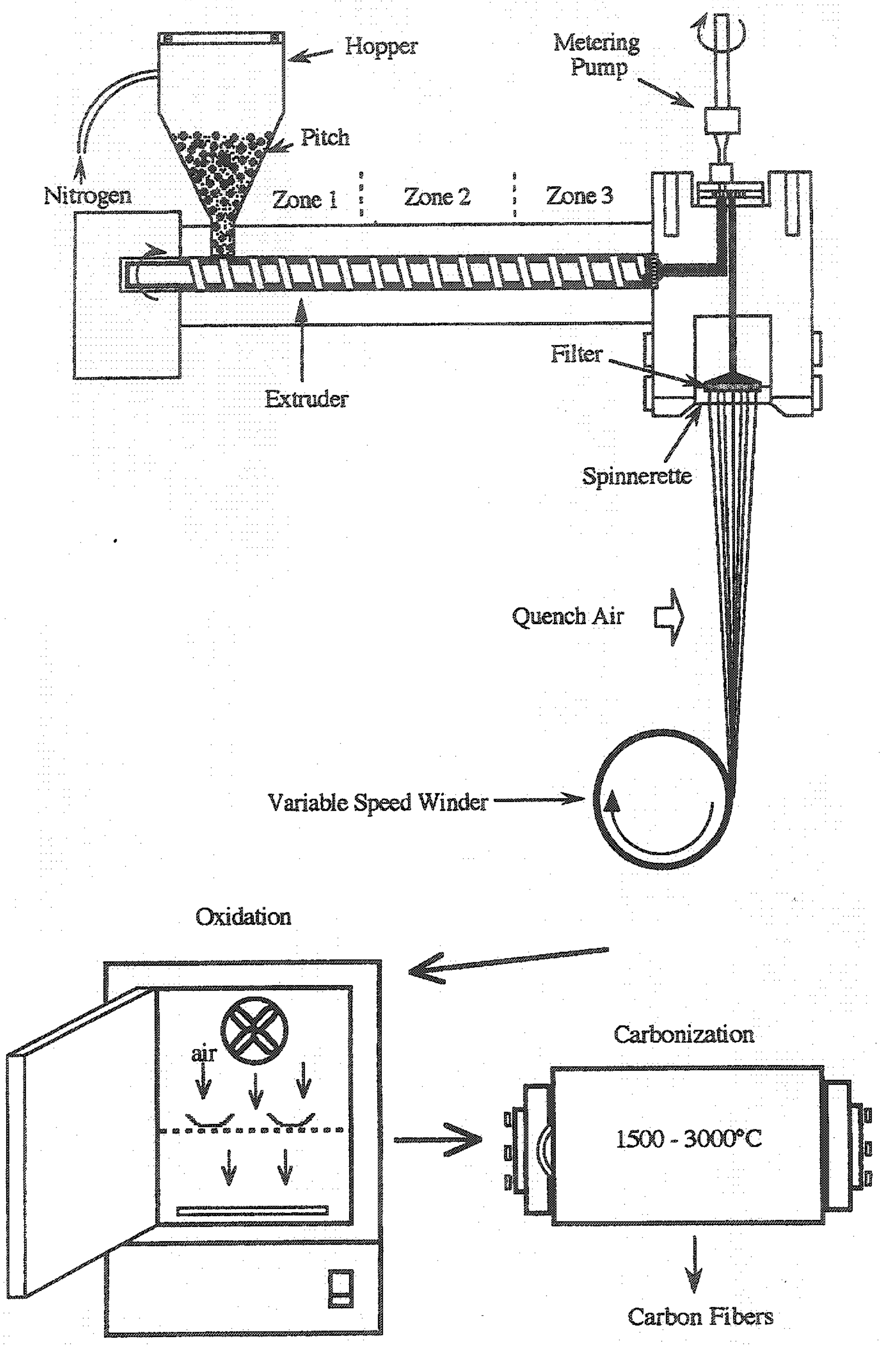

Figure 8: Processing sequence of mesophase carbon fibers, showing continuous conventional melt spinning of mesophase pitch, and subsequent processes: oxidization stabilization, and carbonization. The oxidation, stabilization, and carbonization steps are conducted continuously. Adapted from [1].

As the basic fiber microstructure is determined during the spinning and drawing processes, several spinning process variables have a significant impact on fiber properties (e.g. flow rate, winder speed, spinnerette geometry, etc.). Upon emerging from the spinnerette capillaries, the as-spun fibers are drawn to improve axial orientation and are collected on a wind-up device.

1.4.2 Fiber Stabilization

The as-spun mesophase fibers are extremely weak, and must be heat-treated to develop their ultimate mechanical and thermal properties. The purpose of oxidation is to prevent the fiber from melting during the subsequent carbonization process, thus to "lock in" the structure developed during the extrusion process. The stabilization is accomplished by exposing the fibers to flowing air at a temperature of approximately 300° C for a duration of time ranging from a few minutes to a few hours, depending on the precursor, the fiber size, and the oxidation temperature [1]. During this process, oxygen tends to first react with aliphatic side groups, cross-linking and adding weight to the fiber [19]. If insufficient time is allowed for stabilization, there is a gradient of oxygen across the filament radius, and a skin core texture may result. Fibers thinner than 10μm do not exhibit a skin core texture because of rapid oxygen diffusion, unless the oxygen content of the oxidizing atmosphere is reduced. Because of the length of time required, the oxidation process adds significantly to the overall processing cost for mesophase pitch-based carbon fibers. Once the fibers have been adequately stabilized, carbonization is possible.

1.4.3 Fiber Carbonization

Carbonization or high temperature heat treatment of stabilized fibers may consist of two separate steps: first heating to around 1000°C in order to reduce the rate of gas evolution and then to temperatures between 1200 and 3000°C, depending upon the desired tensile strength and modulus. The tensile strength for MP fibers continuously increases with heat treatment temperature in contrast to PAN-based fibers. The high temperature mesophase pitch-based fibers have a higher modulus and usually a lower tensile strength compared to PAN-based fibers at the same temperature. During carbonization, dislocations in the initial disordered carbon stacks are annealed out, eventually resulting in the formation of a three-dimensional graphite lattice. The graphitization process primarily involves atomic diffusion and crystallite growth.

1.5 Vapor Grown Carbon Fibers

Another method that can be employed to manufacture carbon fibers is vapor grown carbon fiber (VGCF) [30]. VGCFs are prepared by the decomposition of gaseous hydrocarbons at temperatures between 300 and 2500°C in presence of an ultra-fine metallic catalyst (e.g. Fe, Ni, and Co). These carbon fibers are characterized by the high-preferred orientation of graphitic basal planes parallel to the fiber axis, which give high mechanical performance, excellent electrical conductivity and high graphitizability to the fibers. Two methods of forming VGCFs have been developed: seeding catalysts on a substrate and fluidizing catalysts in space. VGCFs maybe grown on several types of substrates (e.g. carbon, silicon, quartz) and from many hydrocarbons (e.g. acetylene, benzene, natural gas, etc.), but in all cases growth is favored in a hydrogen atmosphere. Filament diameter may range from 100nm to several hundred micrometers. The process leads to the formation of fibers having various cross-sections, namely circular, helical, and twisted etc.

Because of the VGCFs unique structure and excellent performance, such as high mechanical, electrical and thermal properties, etc., they are expected in different fields of application as structural and functional materials. Thus, VGCF is emerging in markets as a new type of carbon and graphite whisker and is under extensive study for both basic research and future applications. This type of carbon fiber could be sufficiently low priced in the future to replace ordinary carbon fibers in discontinuous yarn and thus serve as useful filler for composites. Applications have already been developed; for example, the VGCF by modifying the surface has been proved to be an excellent adsorbent with high surface area. In addition, using nanometer sized fibers, thermoplastic composites with electrical conductivity have been fabricated with a microscopically smooth surface, allowing for electrostatic painting [30]. In this thesis however we would be mainly concentrating on the mesophase pitch-based carbon fibers fabricated by melt spinning.

Since mesophase carbon fibers belong to a category of matter called liquid crystals, it is necessary to give some background on liquid crystals.

1.6 General Background on Liquid Crystals

For many organic compounds the phase transition between the solid state and liquid state is not a single-phase transition but they assume one or more intermediate states called mesophases. The mesomorphic phases possess both liquid-like fluidity and solid-like molecular order [20]. The centers of masses of molecules constituting solid crystals are located in a three dimensional periodic lattice, hence they have both orientational as well as positional order. In the case of isotropic liquids, only short-range order prevails among the constituent molecules. The ordering in mesophases (anisotropic liquids) is intermediate between that of a solid and of an isotropic liquid as shown in figure 9. Based on the partial ordering two fundamentally different types of mesophases have been observed [21]. The first type shows a transition from a strongly ordered state to a phase where each molecule commutes between several equivalent orientations. The positional order is still present but the orientational order has disappeared or is strongly reduced, and this phase is called disordered crystal mesophase or plastic crystal. The second type shows a low temperature phase where the positional order is reduced or has even completely disappeared but exhibits long-range orientational order, and this phase is called ordered fluid mesophase or liquid crystal. The shape of the molecule is an important factor for mesomorphism to occur. During early studies of liquid crystals, researchers believed that the molecules must possess a rod-like shape to exhibit thermotropic mesomorphism. It has been discovered in the last two decades that various compounds, both naturally occurring and synthetic, consisting of disc-like molecules can also exhibit thermotropic mesomorphism. Naturally occurring carbonaceous mesophases, which are derived from pyrolysis of coal and petroleum pitches, display discotic liquid crystalline behavior [13]. Our focus will be on the study of discotic nematic liquid crystal material behavior.

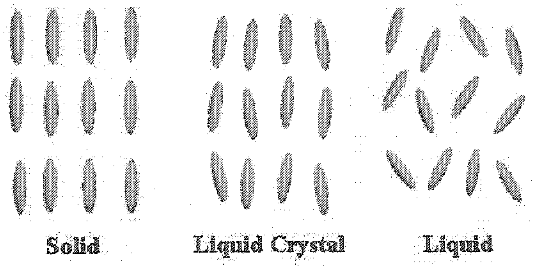

Figure 9: Schematic representation of molecular alignment in a crystalline solid, a liquid crystal, and an isotropic liquid. As is apparent liquid crystals are not as ordered as crystalline solids, yet have some degree of alignment. Adapted from [23].

1.7 Classification of Liquid Crystals

There are two important methods of classifying liquid crystals based on their physical composition or behaviour (i.e. thermotropic and lyotropic) and molecular order or orientation (nematic, cholesteric, smectic). There are two other classifications based on the qualitative differences in the molecules: shape of molecules (rod-like, disc-like) and weight of the constitutive molecules (polymeric liquid crystals and low molecular weight liquid crystals LMWLC)

1.7.1 Classification based on Physical Composition

(a) Thermotropic Liquid Crystals

Single component systems that show mesomorphic behaviour in a definite temperature range , are called thermotropic or non-amphiphilic liquid crystals and are primarily associated with low molecular weight liquid crystals. Every molecule in the thermotropic liquid crystalline phase participates in the long-range ordering. The material exhibits liquid crystalline behavior below transition temperature T_{NI}. The liquid crystalline phase is isotropic above the transition temperature. Thermotropics are of interest for application in electro-optical display, temperature and pressure sensors, organic fibers, and special materials of construction such as bullet-proof jackets, etc. [2]. Most computer and watch displays use a mixture of low molecular weight liquid crystals, such as 8CB(p-octyl-p-cybobiphenyl).

(b) Lyotropic Liquid Crystals

Lyotropics show mesomorphic behaviour in solution and are usually the solution of rigid, high molecular weight molecules in various solvents, with concentration (as opposed to temperature for thermotropics) as the driving force behind the mesomorphic behaviour [3, 21]. The anisotropic behaviour is shown above a particular concentration. A well-known commercial example of lyotropics is Kevlar, which is a solution of poly-p-phenylene terepthalmide in sulphuric acid. The temperature range in which lyotropic liquid crystals are stable depends mainly on the phase concentration. The long-range order is mainly controlled by the rigid rod-like (solute) molecules. Lyotropic liquid crystals are of great interest in living systems, and appear to play an important role in living systems.

1.7.2 Classification Based on Molecular Order

(a) Nematic Liquid Crystals

Figure 10 gives a schematic representation of the molecular order in the nematic phase. The molecules tend to align parallel to each other along some common axis called director **n**. The director is a unit vector (**n.n** = 1), and gives the average preferred orientation. Long-range orientational order and cylindrical

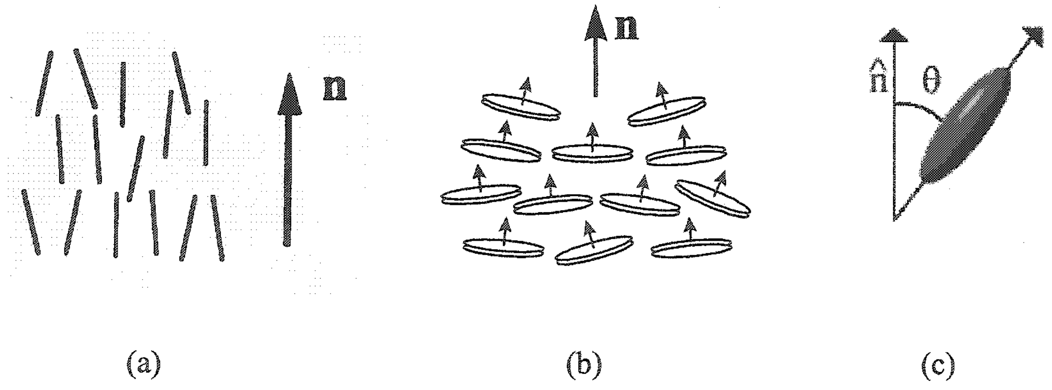

Figure 10: Schematic representation of (a) rod-like nematic liquid crystals, and (b) discotic nematic liquid crystals. The director **n** represents the average preferred orientation of the molecules for (c) rod-like nematics, whereas in discotic nematics **n** is the average preferred orientation of the unit normals to the disc-like molecules.

symmetry are exhibited by this phase. The centres of gravity of the molecules are distributed at random in space. Thus, nematic liquid crystals possess orientational order like that of crystals but positional disorder like that of isotropic fluids. In rod-like nematics, the director **n** represents the average preferred direction of the molecules, as shown in figure 10a. Whereas in the case of disk-like nematics, the director **n** represents the preferred direction of the unit normal to the disk-like constitutent molecules, as shown in figure 10c. The degree of alignment of the individual molecules along the director **n** is given by a scalar quantity known as scalar order parameter S:

$$S = \left\langle \frac{3}{2} \cos^2\theta - \frac{1}{2} \right\rangle \tag{1.1}$$

where θ is the angle between the director **n** and the long axis of each rod-like molecule in rod-like nematics, and between the director **n** and unit normal of each disc-like molecule in discotic nematics. The brackets denote an ensemble average over of the molecules. In an isotropic liquid $S \to 0$ whereas for a perfect crystal $S \to 1$. Typical values for the scalar order parameter of a liquid crystal range from 0.3 to 0.9, with the exact value being determined by temperature in our case. We attempt to elucidate further on the texture transformations of discotic nematic liquid crystals in this thesis.

(b) Cholesteric Liquid Crystals

Cholesteric liquid crystals are typically composed of nematic mesogenic molecules containing a chiral center, which produces intermolecular forces that favour alignment between molecules at a slight angle to one another. This results in formation of a structure, which can be visualized as a stack of very thin 2-D nematic-like layers with the director in each layer twisted with respect to those above and below. In this structure, the directors actually form a continuous helical pattern about the layer normal as illustrated by the black arrows in Figure 11. The lack of long-range translational order imparts fluidity to the cholesteric

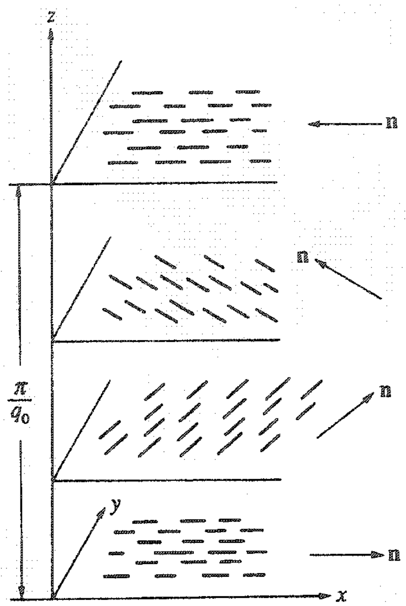

Figure 11: Schematic arrangement of rod-like molecules in a cholesteric liquid crystalline phase. The localized director **n** follows a helical trajectory along the z-axis. Please note that the successive planes are drawn for convenience, and do not have any physical meaning. Adapted from [24].

phase. On a local scale, the cholesteric order is similar to the nematic order, since the molecules tend to align along the director **n**. On a larger scale, the cholesteric director follows a helical path as shown. Thus, an important characteristic of the cholesteric liquid crystals is the pitch, the distance that the cholesteric director traverses to rotate one full turn (360°) in the helix.

(c) Smectic Liquid Crystals

A smectic phase has, in addition to the orientation order of nematics and cholesterics, a single degree of translational order, which results in a layered structure. In the smectic phase, the molecules maintain the general orientational order of nematics, but also tend to align themselves in layers or planes. Motion is restricted to within these planes, and the separate planes are observed to flow past each other. The layer spacing is of the order of 20Å. Smectic phases always occur at temperatures below the nematic range, since they are more ordered. The increased order means that the smectic state is more "solid-like" than the nematic phase. More than twelve smectic phases have been identified, however: the best known are smectic-A and smectic-C. Figure 12 shows the schematics of a smectic-A phase and smectic-C phase. In smectic-A phase the molecule director is aligned perpendicular to the smectic plane (or parallel to the layer normal) and there is no positional order within each layer. Similarly, smectic-B liquid crystal phase orients with the director perpendicular to the smectic plane, but positional order is also present which leads to the molecules being arranged in a network of hexagons within the layer. In the smectic-C phase the molecules are oriented in a similar way but the director is at a constant tilt angle ω measured normally to the smectic plane.

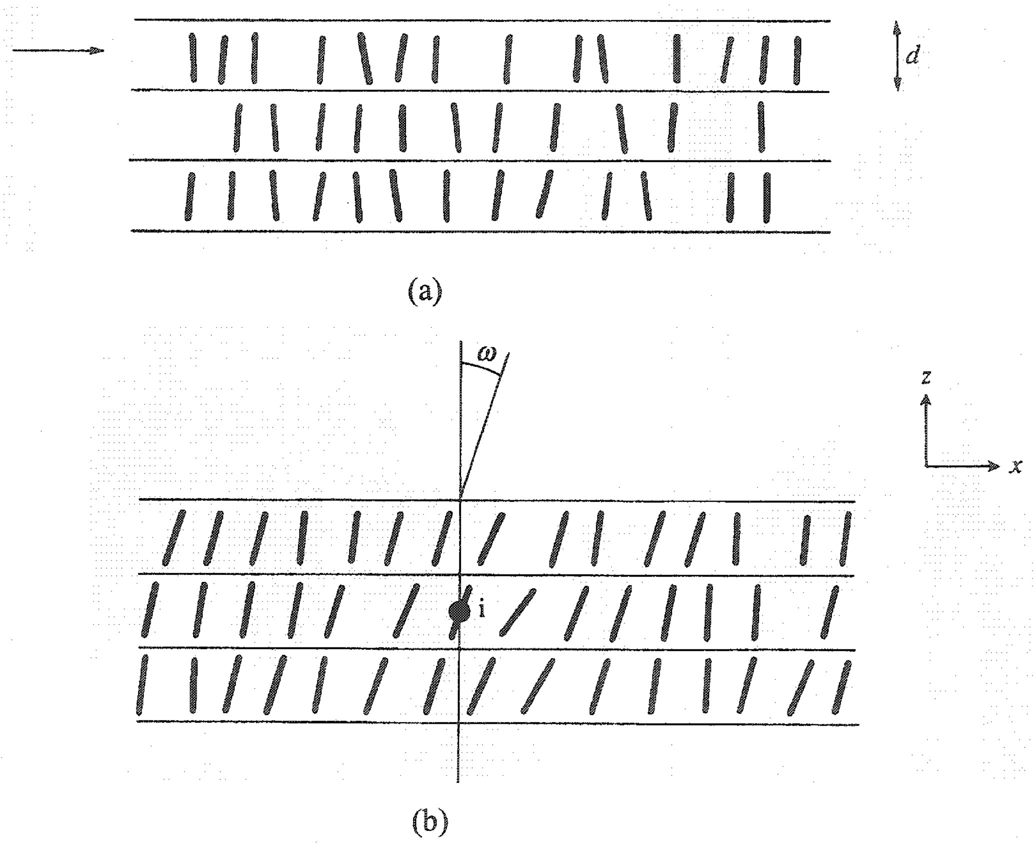

Figure 12: Schematic arrangement of rod-like molecules in (a) Smectic A, and (b) Smectic C liquid crystalline phases. The shown smectic phases have 2-dimensional layered structure. In smectic C phase the constituting molecules are tilted at an angle ω normal to the smectic plane. Adapted from [24].

1.8 Mesophase Pitch-based Carbon Fiber Textures

The carbon fibers melt-spun from mesophase pitch exhibit a spectrum of transverse textures that are associated with various mechanical and thermal transport properties.

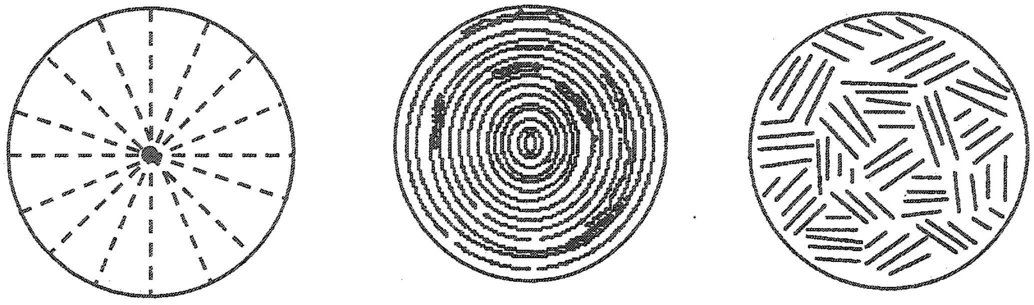

Radial Onion-skin Random

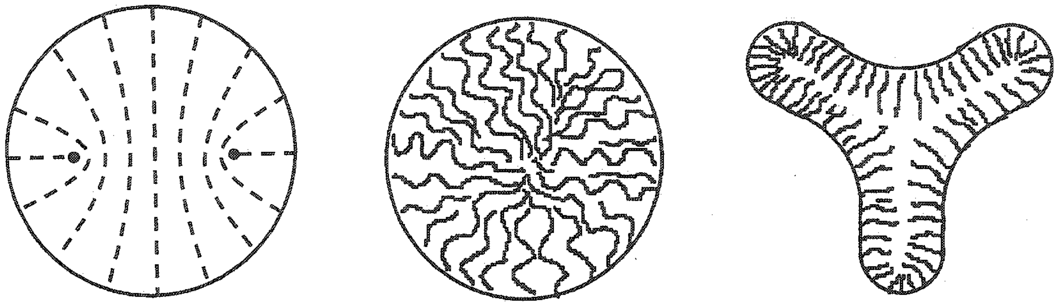

Planar Polar Radial-folded Line-origin

Figure 13: Schematics of the observed mesophase carbon fiber textures. The lines represent the locus of the side view of the disc-like molecules, such that in a radial texture, the discs orient with their unit normals describing circles concentric with the fiber axis, while in an onion-like texture, the discotic molecules themselves follow a circular path concentric with the fiber axis. Adapted from [1].

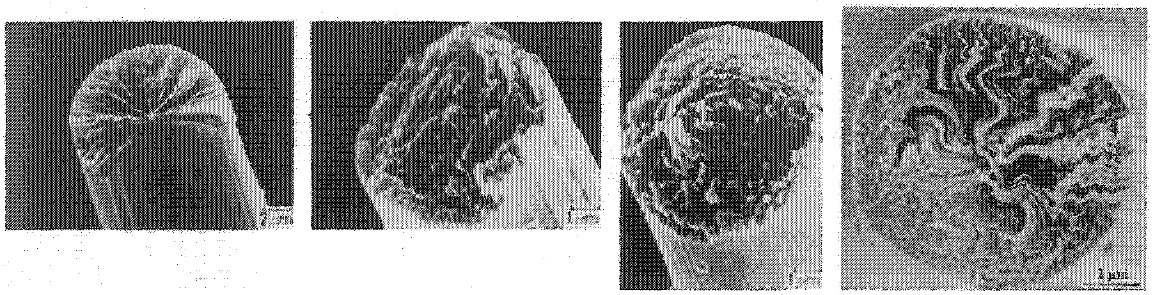

(a) (b) (c) (d)

Figure 14: SEM images of mesophase pitch-based carbon fibers with (a) radial texture, (b) random texture, (c) onion texture, and (d) radial-folded-texture. The fiber diameter range is 5-15 microns. Adapted from [2].

The microstructure is defined by the spatial arrangement of the flat disc-like molecules in fibers of different cross-sectional shapes. The commonly observed transverse textures are random, radial, onion-like, and planar polar or a mixture of these textures across a fiber radius. Figure 13 shows schematically some of the textures reported in the literature. The lines in the figure inside the fiber cross-section represent the loci of the side view of the disc-like molecules. In a radial texture, the discotic molecules orient with their unit normals describing circles concentric with the fiber axis, while in the onion-like texture the discotic molecules themselves follow a circular path concentric with the fiber axis. The scanning electron micrographs (SEM) of radial, random, onion-like, and radial folded are shown in figure 14. The cores of the mesophase carbon fibers may be isotropic or anisotropic, the latter would give rise to a singular defect line running across the fiber core. Although the strength and thermal conductivity of mesophase carbon fibers are generally very high, these properties can vary significantly with fiber textures. For radial textures, the presence of a singular line along the fiber axis introduces a potential fast failure mode by longitudinal crack propagation [25], such failure modes are absent in the onion-like outer layer textures. Commonly, the textures are not perfect and some degree of folding of the crystallites is observed. This appears to improve the resistance of the fiber to crack propagation, and thereby increasing its tensile strength [1]. Folding may be an artifact of the disclinations in the mesophase pitch, which are not annihilated by the strong deformations. Creation of the random texture, no clearly defined morphology, may be due to complete disruption of the flow fields inside the spinneret [26], and such fibers also offer the potential of improved compressive strengths. The fiber microstructure can be controlled by the pretreatment of mesophase pitches, the constitution and spinnability of pitches, the spinning conditions, the spinneret geometry, the processing conditions, the fiber size and shape, and numerous other factors. A great majority of authors attribute the cross-sectional microtextures to spinning [29]. A variable spinneret design and variable melting temperature range are related to the occurrence of various microtextures and to the preferred orientation degree of the final graphitized fiber. When the flow through the spinneret capillary is laminar, radial arrangements are obtained (spinneret devoid of stirrer). The onion or the random microtexture are attributed to the increasingly turbulent flow due to the mobile stirrer increasingly approaching the stirrer die [26]. A decreasing viscosity of the pitch only increases the preferred orientation of the fiber. Many researchers have captured the effect of temperature on the carbon fiber morphology. They have shown that radial texture is preferred at lower temperature and onion texture prevails at higher spinning temperature [27]. This phenomenon of texture transformation of the carbon fiber at different temperature has also been theoretically proved by Wang and Rey [28] by computation simulation of the minimization of the Frank long-range elasticity of the fiber. Matsumoto managed to control the transverse texture by extruding the precursors through capillaries of different diameters. It was shown that larger diameter capillaries yielded onion-skin texture, whereas capillaries with smaller diameters tended to produce radial textures.

1.9 Thesis Objectives

It is apparent that there is a strong structure property relationship for mesophase pitch carbon fibers and the microstructure in turn is closely related to processing conditions. Thus, there is a need to clearly understand the underlying principles that govern the texture transformation in the mesophase carbon fibers.

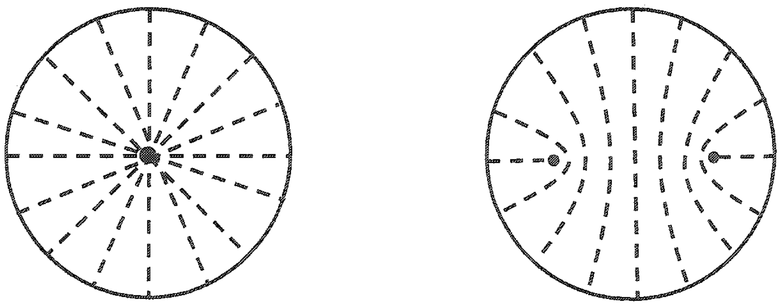

Radial Planar Polar

Figure 15: Schematic of the two characteristic textures namely Planar Radial (PR) and Planar Polar (PP) observed in the carbon fibers. The lines represent the side view of the disc-like molecules. The unit normals to the discs are perpendicular to the solid lines. Adapted from [1, 2].

Figure 15 represents the two characteristic textures that will be the focus of study in this thesis. As a first step we will define the theoretical framework or model by selecting the appropriate constitutive equation that defines our system unambiguously. Theory and simulation of liquid crystalline materials continues to be performed using macroscopic, mesoscopic, and molecular models [3]. Macroscopic models are vector (director) models based on the Frank elasticity and are unsuitable here because of the presence of defects, represented by dark dots in figure 15, which introduces singularities in our system. Therefore we use the tensor model based on well-established Landau-de Gennes theory of liquid crystals [23]. This theory takes into consideration necessary contributions to the free energy namely the homogeneous contribution and the non-homogenous contribution. The main objectives of this study are listed below:

- To characterize using well-established theories and computer simulation the texture formation of the characteristic textures, namely the planar radial (PR) and planar polar (PP).
- To obtain the characteristic phase diagram representing the phase transition between the planar radial (PR) and the planar polar (PP) with respect to the temperature and fiber radius.
- To characterize the driving forces namely the long-range energy (non-homogeneous) and the short-range energy (homogeneous) that promote the selection of PR and PP texture.
- To establish the physical parameters i.e. operating conditions and geometric considerations respectively that lead to the two characteristic textures.

Bibliography

[1] McHugh J.J., "*The development of orientation in mesophase pitch during fiber formation*", Ph.D. Thesis, Clemson University, Clemson, SC, USA (1994)

[2] Peebles L.H., *Carbon Fibers: Formation, Structure, and Properties* (CRC Press, Boca Raton, 1995).

[3] ed. by Priestley E.B., Wojtowicz P.J., Sheng P., *Introduction to Liquid Crystals,* (Plenum Press, New York, 1975).

[4] Kowalsky I.M., "*New high performance domestically produced carbon fibers*", Advanced Materials Technology '87: Volume 32 of the International SAMPE Symposium, Editors: R. Carlson *et al.*, Anaheim, p953 (1987)

[5] Kelly B.T, *Carbon* **5**(3) 247 (1967)

[6] Bacon R., Nelson L.C., Singer L.S., Schulz D.A., Wagoner G., Lewis I.C., Lewis R.T., Strong S.L., Rosen B.W., and Sullivan B.J., "*Spacecraft applications for carbon-carbon—Basic research effort*", Naval Surface Warfare Center Transcript 89-168, Silver Spring, MD (1989).

[7] Singer L.S., Lewis I.C., *Carbon* **16**(6), 417(1978)

[8] Zimmer J.E., White J.L., in "Advances in Liquid Crystals" **5**, 157 (Academic Press, New York, 1982)

[9] Hutchenson K.W., Roebers J.R., and Thies M.C., *Carbon* **29**(2) 215 (1991)

[10] Singer L.S., *Faraday Discuss. Chem. Soc.*, **79**, 265(1985)

[11] Gasparoux H., *Mol. Cryst. Liq. Cryst.*, **63**, 647(1981)

[12] Brooks J.D., Taylor G.H., *Carbon*, **3**, 185(1965)

[13] Otani S., *Mol. Cryst. Liq. Cryst.*, **63**, 249(1981)

[14] Chwastiak S., and Lewis I.C., *Carbon* **16**(2) 156 (1978)

[15] Diefendorf R.J., Riggs D.M., "*Forming optically anisotropic pitches*", U.S. Patent 4,208,267 (1980)

[16] Mochida I., Shimizu S., Korai Y., Otsuke Y., Sakai H., and Fujiyama S., *Carbon* **26**(6) 843 (1988)

[17] Edie D.D., Dunham M.G., *Carbon*, **27**, 647(1989)

[18] Peebles L.H. Jr., *Int. Mater. Rev.*, **39**, 75(1994)

[19] Rand B., in *Handbook of Composites, Volume 1: Strong Fibres*, 495-575, ed. by Watt W., Perov B.V., (North Holland, Amsterdam, 1985).

[20] Chandrasekhar S., *Liquid Crystals,* 2nd Edition, (Cambridge University Press, Cambridge, 1992)

[21] Vertogen G., de Jeu W.H., *Thermotropic Liquid Crystals, fundamentals,* (Springer-Verlag, Berlin, 1988)

[22] PLC, CWRU (2000), Polymer and Liquid Crystals Website, Case Western Reserve University, http://abalone.cwru.edu/tutorial/enhanced/main.htm

[23] de Gennes P.G., *The Physics of Liquid Crystals,* 2nd edition (Clarendon Press, oxford, 1995)

[24] Chandrasekhar S., Sadashiva B.K., and Suresh K.A., *Pramana-J. Phys.* **9** 471 (1977)

[25] Singer L.S, *Ind. Conv. of Coal and Carbon to Gas, Liquid, and Solid Products,* London, (1981).

[26] Nazeem F.F., *Process for controlling the cross-sectional structure of mesophase pitch derived fibers*, U.S. Patent 4,376,747 (1983).

[27] Mochida I., Yoon S.H., and Korai Y., *J. Mater. Sci.* **28** 2331 (1993)

[28] Wang L. and Rey A.D., *Modell. Simul. Sci. Eng* **5** 67 (1997)

[29] Hamada T., Nishida T., Furuyama M., Tomoioka T., and Endo M., *J. Mater. Res.* **5**, 1271 (1990)

[30] *Carbon Fibers – 3rd Edition* ed by Donnet J-B., Wang T.K., Peng J.C.M., and Reborillat S., (Marcel Dekker, New York, 1998).

[32] Matsumoto M., *Pure Appl. Chem.* **57**(11) 1553 (1985)

[33] Tsuji T., and Rey A.D., *J. Non Newtonian Fluid Mech.*, **73** 127 (1997)

Chapter 2

Theory and Mathematical Model

This chapter presents basic principles of liquid crystal physics, governing equations to describe structure evolution in liquid crystalline materials, and the formulation and solution methodology of the mathematical model that describes texture formation in mesophase carbon fibers.

2.1 Orientational Ordering

The description of the thermodynamics of phase transitions in uniaxial nematic liquid crystals requires the specification of the average molecular orientation (known as the unit vector or director **n**) and the degree of molecular alignment along the average orientation, known as the uniaxial scalar order parameter [1]. The first idea would have been to use the average, $< \cos\theta >$, of the cosine of the angle between the direction of a particular molecule **a**, and director **n**, for uniaxial nematics (i.e. oriented along a single direction). However, this vanishes identically for nematics given the fact the directions **n** and –**n** are equivalent. Thus a higher moment of the uniaxial molecular orientation distribution needs to be used. The lowest order one giving a non-trivial answer is the order parameter or scalar order parameter S, defined as [2]:

$$S = \left\langle \frac{3}{2} \cos^2\theta - \frac{1}{2} \right\rangle \qquad (2.1)$$

where the angular brackets denote an ensemble average over all possible molecular configurations. For more general (than uniaxial) molecular orientations, the tensorial equivalent of the scalar order parameter S, denoted by $\mathbf{Q}$ and defined in terms of the distribution of the orientation unit vector $\mathbf{a}$, of the molecules as [3]

$$\mathbf{Q} = \left\langle \mathbf{aa} - \frac{1}{3}\boldsymbol{\delta} \right\rangle \tag{2.2}$$

The tensor $\mathbf{Q}$ is a symmetric and traceless second order tensor and is defined using a tensorial physical property such as the magnetic susceptibility, the dielectric polarizability or the dielectric constant and extracting its anisotropic part [2, 4]. $\mathbf{Q}$ vanishes in the isotropic phase. In biaxial nematics there is a second scalar order parameter P, corresponding to the biaxial director $\mathbf{m}$, that specifies the transverse ordering. The tensor order parameter $\mathbf{Q}$ can be represented in terms of the two order parameters namely S and P and the three directors $\mathbf{n}$, $\mathbf{m}$ and $\mathbf{l}$ by the form

$$\mathbf{Q} = S(\mathbf{nn} - \frac{1}{3}\boldsymbol{\delta}) + \frac{P}{3}(\mathbf{mm} - \mathbf{ll}) \tag{2.3}$$

where the following restrictions apply

$$\mathbf{Q} = \mathbf{Q}^{\mathrm{T}}\,;\ \mathrm{tr}(\mathbf{Q}) = 0; \quad -\frac{1}{3} \le S \le 1\,; \quad -\frac{3}{2} \le P \le \frac{3}{2}\,; \tag{2.4 a,b,c,d}$$

$$\mathbf{n}\cdot\mathbf{n} = \mathbf{m}\cdot\mathbf{m} = \mathbf{l}\cdot\mathbf{l} = 1;\ \mathbf{nn} + \mathbf{mm} + \mathbf{ll} = \boldsymbol{\delta} \tag{2.4e,f}$$

The uniaxial director $\mathbf{n}$ corresponds to the maximum eigenvalue $\frac{2}{3}S$, the biaxial director $\mathbf{m}$ corresponds to the second largest eigenvalue $-\frac{1}{3}(S-P)$, and the second biaxial director $\mathbf{l}$ (= $\mathbf{n}\times\mathbf{m}$) corresponds to the smallest eigenvalue $-\frac{1}{3}(S+P)$. This ordering of eigenvalues from smallest to the largest is valid as long $S > \frac{P}{3}$. The orientation is defined by the orthogonal director triad ($\mathbf{n}$, $\mathbf{m}$, $\mathbf{l}$). The magnitude of the uniaxial scalar order parameter, S is a measure of the alignment along the uniaxial director $\mathbf{n}$. and can be expressed as:

$$S = \frac{3}{2}(\mathbf{n}\cdot\mathbf{Q}\cdot\mathbf{n}) \tag{2.5}$$

Similarly the biaxial scalar order parameter P, representing the degree of alignment along the biaxial director $\mathbf{m}$ can be expressed as:

$$P = \frac{3}{2}(\mathbf{m}\cdot\mathbf{Q}\cdot\mathbf{m} - \mathbf{l}\cdot\mathbf{Q}\cdot\mathbf{l}) \tag{2.6}$$

Therefore the tensor order parameter can be represented in its diagonal form by [5]:

$$\begin{bmatrix} -\frac{1}{3}(S-P) & 0 & 0 \\ 0 & -\frac{1}{3}(S+P) & 0 \\ 0 & 0 & \frac{2}{3}S \end{bmatrix} \tag{2.7}$$

If the nematic is uniaxial, $P = 0$, equation (2.3) representing the **Q** in terms of the two scalar order parameters and the three orthogonal vectors **n**, **m**, **l** reduces to

$$\mathbf{Q} = S(\mathbf{nn} - \frac{1}{3}\delta) \tag{2.8}$$

In this uniaxial case, if the coordinate system is so chosen that **n** is along the z-axis then **Q** can be expressed in the diagonal form:

$$\begin{bmatrix} Q_{\perp} & 0 & 0 \\ 0 & Q_{\perp} & 0 \\ 0 & 0 & Q_{\parallel} \end{bmatrix} \tag{2.9}$$

where $Q_{\perp}$ stands for the two equal eigenvalues of **Q** in the plane normal to **n** and $Q_{\parallel}$ refers to the largest one parallel to **n**.

As a symmetric second order tensor, **Q** can be represented geometrically by a quadratic surface in the form [6]:

$$Q_{ij}x_ix_j = 1 \tag{2.10}$$

where the Einstein summation convention is used. The quadratic surface given by equation (2.10), in its principal axes, takes the form:

$$\frac{(x_1)^2}{1/\lambda_1} + \frac{(x_2)^2}{1/\lambda_2} + \frac{(x_3)^2}{1/\lambda_3} = 1 \tag{2.11}$$

where λ_i ($i = 1,2,3$) are the three eigenvalues of **Q**. If they are positive, the surface is an ellipsoid with semiaxes of length:

$$\frac{1}{\sqrt{\lambda_1}}, \frac{1}{\sqrt{\lambda_2}}, \frac{1}{\sqrt{\lambda_3}} \tag{2.12}$$

For negative eigenvalues, their absolute values can be used to construct the ellipsoid. In this thesis we use a similar principle for our visualization technique as explained later.

2.2 Long-Range Elastic Distortions in Liquid Crystals

In an ideal, nematic, single crystal, the molecules are (on average) aligned along one common direction ± **n**. The system is uniaxial, and the tensor order parameter has the form given by equation (2.8). However, in most circumstances this ideal conformation is not compatible with the constraints imposed by the limiting surfaces of the sample (e.g. walls of the container) and by external fields acting on the molecule. There will be some deformation of the alignment, the order parameter will vary from point to point. The characteristic distances involved in these phenomena are large compared to molecular dimensions [4]. Thus these deformations maybe described by a continuum theory disregarding the details of the structure on the molecular scale. Such a description has been put forward by F.C. Frank [7] by describing the distorted state entirely in terms of a vector field (**r**). It is assumed that **n** varies slowly and smoothly with **r** (except possibly on a few singular points or singular lines). The free energy density or Frank distortion energy can be written as:

$$F_{\mathrm{D}} = \frac{1}{2}K_{11}(\nabla \cdot \mathbf{n})^2 + \frac{1}{2}K_{22}(\mathbf{n} \cdot \nabla \times \mathbf{n})^2 + \frac{1}{2}K_{33}(\mathbf{n} \times \nabla \times \mathbf{n})^2 \tag{2.13}$$

Where the constants K_{11}, K_{22}, and K_{33} are, respectively, the splay, twist, and bend elastic constants and are named collectively as the Frank elastic constants. It is possible to generate deformations that are pure splay, pure twist or pure bend. Thus each constant K_{ii} must be positive, if not, the undistorted nematic conformation would not correspond to a minimum of the free energy. The three deformations are shown in Figure 16.

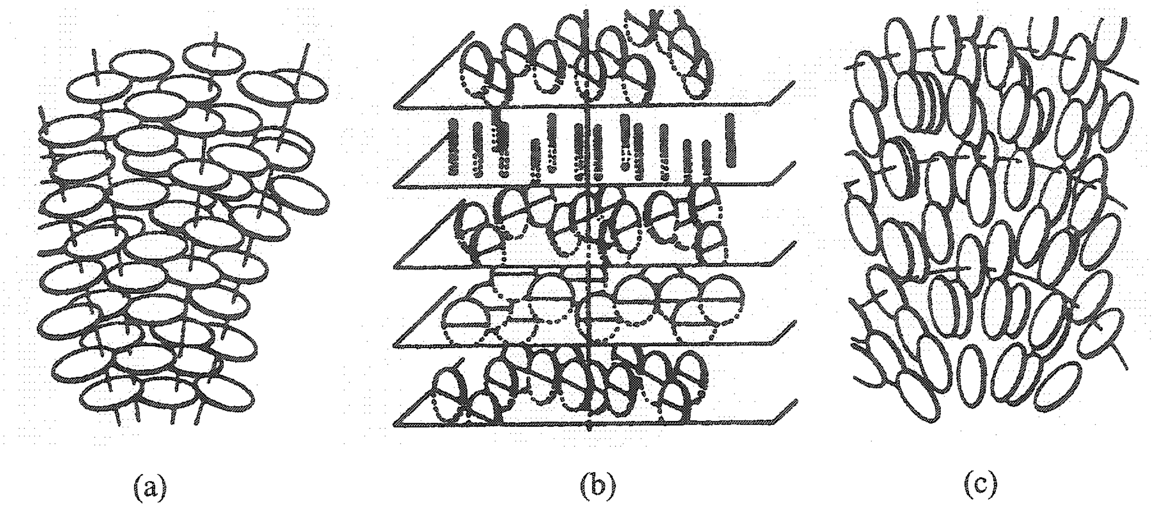

Figure 16: Schematic of the characteristic deformation modes in nematics. (a) Splay deformation (b) Twist deformation (c) Bend Deformation. The lines in the figure represent the director trajectory.

Note that in contrast to rod-like molecules, for disc-like molecules the bending disc's trajectories give rise to a splay deformation, and the splaying of disc's trajectories leads to a bend deformation [8]; disc trajectory means the curve locally orthogonal to the director. The configuration (a) Splay and (c) Bend are planar, whereas (b) Twist is a non-planar configuration. Also for disc-like molecules the twist elastic (K_{22}) constant is greater than the splay (K_{11}) and bend (K_{33}) elasticity, which in other words implies that discotics favor splay and bend configuration more than the twist.

2.3 Disclinations (Defects) in Liquid Crystals

Almost all the observed textures in nematic discotic liquid crystals have the presence of defects called disclination(s). Hence a brief introduction to disclinations is necessary before moving to the details of the problem at hand. A disclination is a discontinuity in orientation i.e. a discontinuity in the director field [2]. Disclinations are associated with a strength (*s*) and dimensionality (*d*) and are characterized by these two properties. Some of the most common disclinations are shown in figure 17 [9]. The continuous black lines show the director trajectory around the disclination. The dimensionality of the defect denotes whether the discontinuity in the director field is located at one point (point defect), on a line

(line defect), or on a surface (wall defect). The strength indicates the degree of rotational discontinuity when encircling the defect. The strength of a disclination

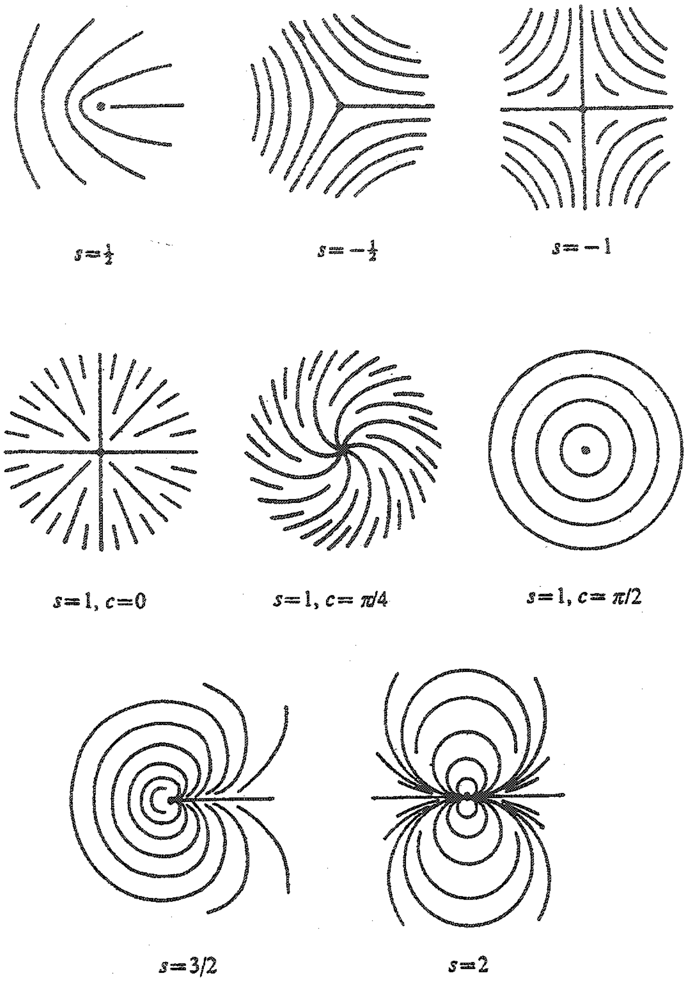

$s=\frac{1}{2}$ $s=-\frac{1}{2}$ $s=-1$

$s=1, c=0$ $s=1, c=\pi/4$ $s=1, c=\pi/2$

$s=3/2$ $s=2$

Figure 17: Classes of various disclinations in a nematic, with the disclination line perpendicular to the plane of the page. The lines around the defect represent the director trajectories around the disclination for the discotic nematics. Adapted from [9].

is determined by the angle $\theta = 2\pi s$ through which the director rotates as one orbits through an angle 2π (a complete rotation) around the defect. When observed under a polarized light microscope, the nematic material with defects displays *schlieren textures* as shown in Figure 18 [9]. The black brushes originating from the dark points are line defects (line singularities), perpendicular to the layer. The brushes are regions where the director (or the local optical axis) is either parallel or perpendicular to the plane of polarization of the incident light. The polarization is unchanged by the material in these regions and is therefore

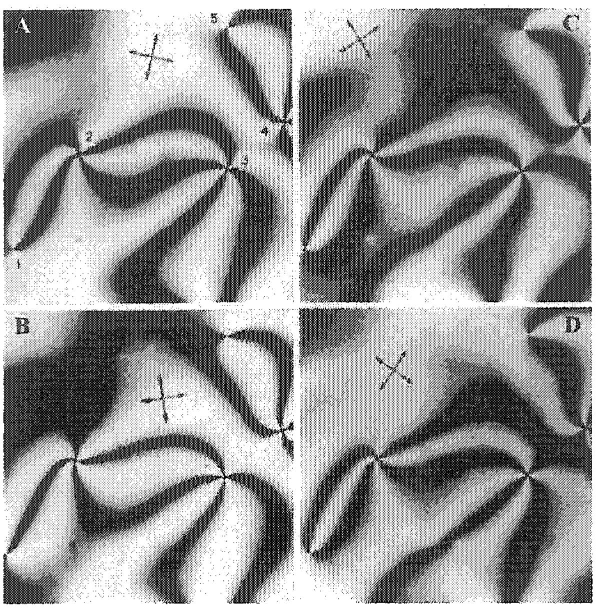

Figure 18: Carbonaceous Mesophases exhibiting schlieren textures as observed by polarized light microscopy. Orientation of the crossed polarizers is indicated by the plotted cross. Strength of the points: No. 1: $s = +1/2$, No. 2: $s = -1$, Nos. 3 and 4: $s = +1$, No. 5: $s = -1/2$. A, B, C, D indicate the rotation sequence of the polarizers (+22.5° counter-clock-wise).

extinguished by the crossed analyzer. Some points have four black brushes while others have only two. The position of the dark points remains unchanged on rotating the crossed polarizers but the brushes themselves rotate continuously showing that the orientation of the director changes continuously about the disclinations. The sense of rotation may be either the same as that of the polarizers (*corotating or positive*) or in the opposite direction to that of the polarizers (*counter rotating or negative*) [10]. The direction of rotation characterizes the positive and negative signs of a defect as shown in figure 17. The rate of rotation is about equal to that of the polarizers when the disclination has four brushes and is twice as fast when it has only two. The strength of a disclination can also be defined as $s = \frac{1}{4} \times (\text{number of brushes})$. The most commonly observed disclinations in carbonaceous mesophases are of strength $s = \pm\frac{1}{2}$ or $s = \pm 1$. The concept of internal distortions in a continuous body was developed at the turn of the century by Volterra [12]. Governed by the curvature elasticities namely splay, twist and bend (figure16), the basic configurations of disclinations that may exist in the carbonaceous mesophases can be developed by certain conceptual operations known as the Volterra process. Referring to figure 19, where the lamellae represent the preferred orientation of mesophase molecules, consider a cut in a body of lamelliform texture along a surface parallel to the lamellae in an unperturbed region (figure 19a). The shape of the surface is arbitrary, and thus the disclination line, the line defining the edge of the surface, can be curved. The direction of the tangent to the disclination line is defined in a right-handed sense in that for a clockwise circuit when looking in the direction of the tangent, face C^+ is encountered first. The two faces of the cut are then rotated with respect to each other about an axis of rotation.

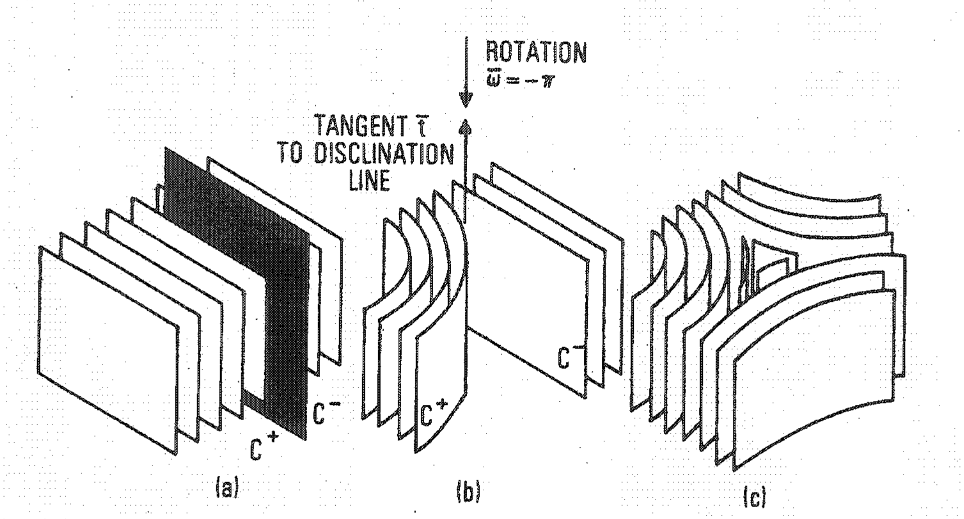

Figure 19: Formation of a negative wedge disclination in a discotic nematic liquid crystal by the Volterra process. (a) A cut is made midway between two adjacent lamellae. (b) Face C^+ is rotated about one edge of the cut relative to face C^-. The axis of rotation is antiparallel to the disclination line. (c) Layers are added to heal the cut, retaining the parallel stacking away from the disclination core. Adapted from [10].

The direction of rotation is right handed about the rotation vector and thus the face C^+ is rotated with respect to the C^- face. The symmetry of the carbonaceous mesophase requires that the rotations be only multiples of π. If the two cut faces are rotated apart as shown in figure 19b, the rotation vector ω is antiparallel to the tangent to the disclination line; this is negative wedge disclination. Additional material must be added to heal the cut. For a positive wedge disclination, the rotation vector is parallel to the tangent to the disclination line, and the material must be removed to heal the cut. Therefore in the cases in which the rotation vector is parallel to the tangent to the disclination line, it gives rise to wedge disclinations. In the other case of the rotation vector being perpendicular to the tangent to the disclination line gives rise to twist disclinations as shown in figure 20. In a path circumnavigating a twist disclination, the molecule normals will vary out of plane of the path. Thus we can also term them as out of plane disclinations or deformations. It has been shown that elastic anisotropy controls the stability of the different classes of disclinations [13], and thus the relative abundance of certain types of defects. The effects of anisotropy on stability of $s = \pm\frac{1}{2}$ lines are: (a) wedge disclinations are favoured when $K_{22} > (K_{11} + K_{33})/2$, and are stable against out-of-plane perturbations; (b) twist disclinations are favoured when $K_{22} < (K_{11} + K_{33})/2$, and are unstable against out-of-plane perturbations. It is known that for discotic nematics [14] that $K_{22} > K_{11}, K_{22} > K_{33}$. This implies that for discotic mesophases wedge disclinations of $s = \pm\frac{1}{2}$ should be more abundant than twist disclinations of the same strength. A stability analysis has also shown [15] that twist disclinations are less favourable than wedge disclinations in elastically anisotropic media. Thus, wedge disclinations are much more common in discotic nematic liquid crystal and we will focus on wedge disclinations of strength $s = \pm\frac{1}{2}$ and $s = \pm 1$ from this point onwards.

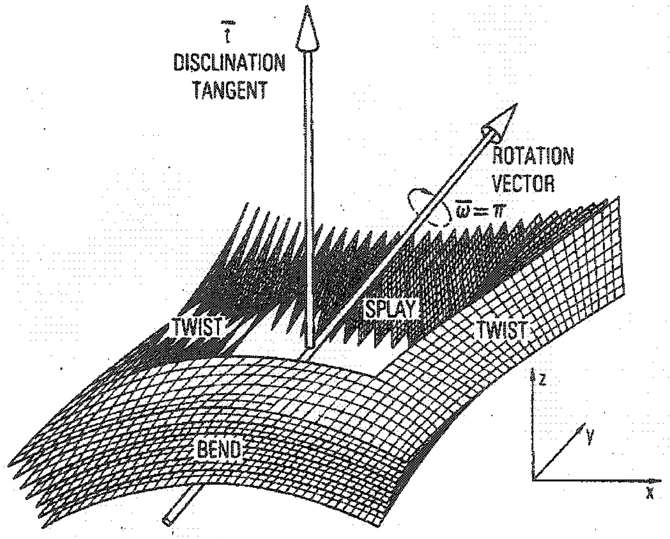

Figure 20: Model of a twist disclination with uniform rotation about the core. Adapted from [10].

2.3.1 Disclination Core Structure in Discotic Nematic Liquid Crystal

The determination of the nature of the core of discotic nematic liquid crystal is an interesting problem with various theories being put forward by various scientists [16-20]. For a single disclination the free energy density can be written as:

$$F_D = \frac{K}{2}\frac{s^2}{r^2} \tag{2.14}$$

Ericksen [16] postulated the concept of an isotropic core based on the fact that since the free energy expression tends to infinity on approaching the center of the defect, below a certain critical radius r_c it should be large enough to transform the material from the nematic to the isotropic phase. Thus, the core should consist of a region of isotropic material separated from the nematic phase. In contrast to the proposed isotropic core, mean-field Landau theory predicts an oblate molecular orientation disribution. Recent studies have shown that the core structure of $s = -\frac{1}{2}$ and $s = +1$ [19, 20] is uniaxial at the center of the defect core surrounded by strongly biaxial nematic material eventually tending to the bulk nematic properties. A disclination line of stength $s = \pm 1$ in a cylindrical geometry can on the other hand become unstable for very large lengths and avoid the planar high-energy state by escaping into the non-planar direction (along the cylinder axis) as shown in figures 21 and 22 and thus giving a disclination with a continuous core with lower energy.

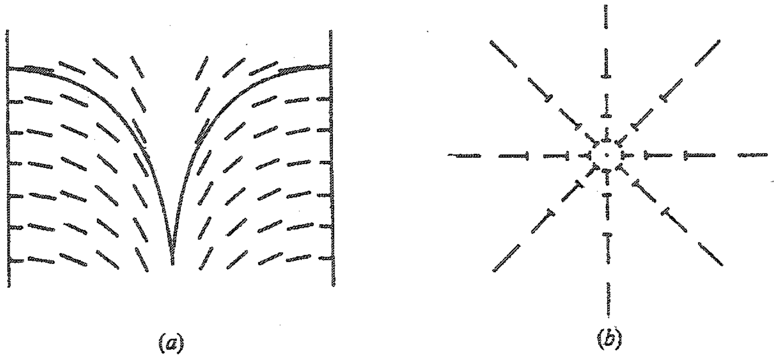

Figure 21: (a) Director escape at the center of a disclination of strength $s = 1$ in a thin capillary: the wall alignment is homeotropic and changes by 90° from wall to the axis (b) Projection of the structure on a plane normal to the capillary axis. Nails signify that the director is tilted with respect to the plane of the paper. Adapted from [9].

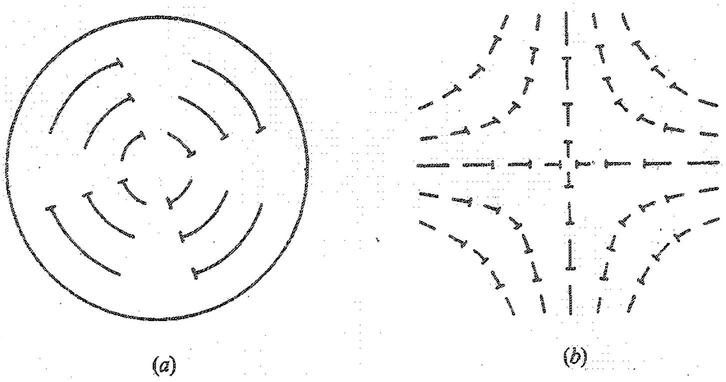

Figure 22: Escaped configurations of (a) onion like $s = 1$ and (b) $s = -1$ disclinations. Nails signify that the director is tilted with respect to the plane of the paper. Adapted from [9].

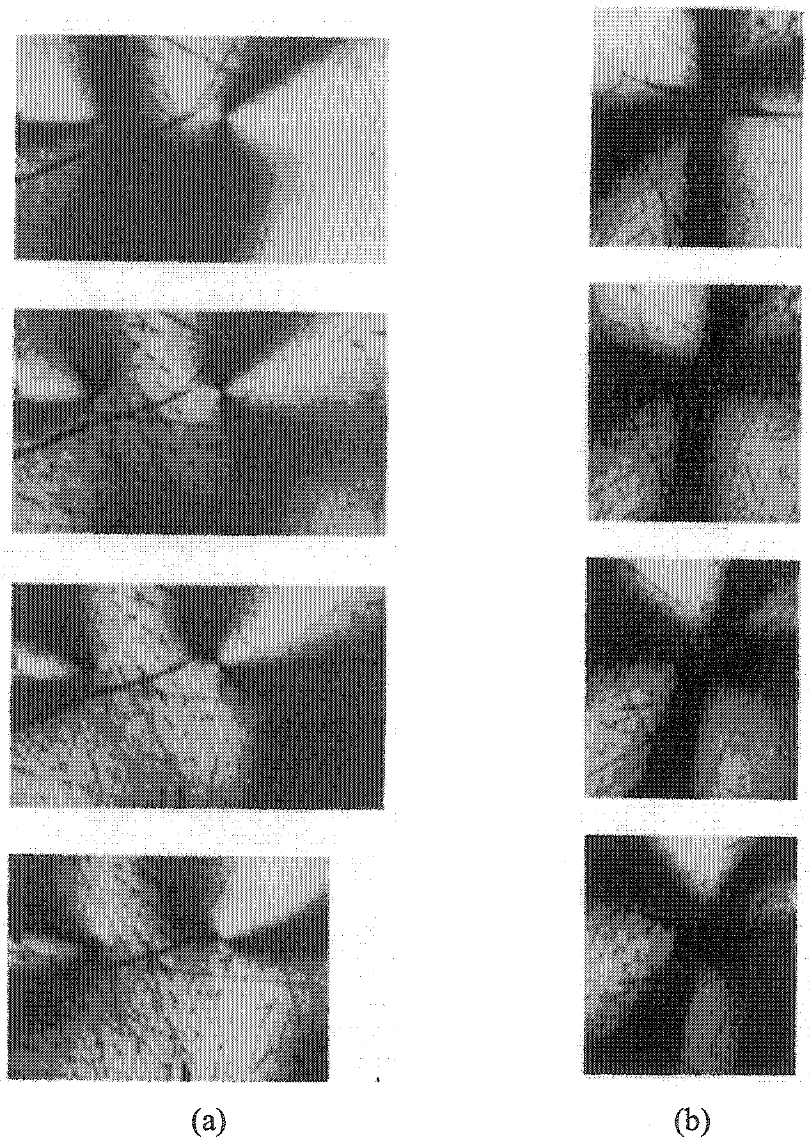

Figure 23: Polarized light micrographs of (a) $s = -1/2$ and (b) $s = +1$ wedge disclinations. It is clearly visible that $s = -1/2$ have thin centers or nodes where as $s = +1$ have thick nodes indicating a escape of the director in the axial direction.

The free energy in this case scales as s instead of s^2 unlike the planar case. This has been experimentally observed in polarized light micrographs where the extinction contour crosses denoting a $s = \pm 1$ wedge disclinations usually have broad centers compared to the sharp, pinched-down centers of the nodes denoting $s = \pm \frac{1}{2}$ wedge disclinations. The broad center as shown in figure 23 is an indication of the continuous core structure [10]. Since the nature of the core will strongly affect the fracture properties of carbon fiber spun from CMs precursors, it is important to study the stability of various textures with different defect structures. On the other hand if the capillary radius is very small or the elastic constant very large (in the one constant approximation i.e. $K_{11} = K_{22} = K_{33}$), the planar solution maybe more favorable energetically.

2.3.2 Formation and Interaction of Disclinations

Initial structural studies of the carbonaceous mesophase were either made on specimens of mesophase glass, solidified from liquid crystalline state by cooling to room temperature or hot stage studies of mesophase specimens between glass slides [22, 23] but direct observation of the dynamic behavior of the mesophase seemed to be inhibited by the reduced mobility of the mesophase. An important step in experimental technique was made by Hoover *et al.* [24] by direct observation on the free surface of the pyrolizing liquid; their films provide dynamic evidence of such microstructural processes as mesophase coalescence and disclination annihilation. This technique has been further extended by designing a quenching capability into the hot stage [25] so that specimens representative of critical points in pyrolysis can be quenched to solidification specimens and studied on polished sections to relate the bulk microstructure to the observations made on the free surface.

During the isotropic-nematic mesophase phase transition, when spherules grow and coalesce to produce large mesophase regions, a large number of disclinations nucleate [10]. The nucleation of disclinations occurs because of a lack of orientation registry between the uncoalesced mesophase regions, such that when they come into contact, orientation incompatibility is resolved by the nucleation of disclinations. For example when three droplets coalesce a disclination of strength $s = \pm\frac{1}{2}$ results, similarly a higher order disclination such as $s = \pm 1$ will require the coalescence of four orientationally incompatible spherules. The material overall has zero topological charge or in other words the sum of strengths of all disclinations in a sample tends to be zero [9].

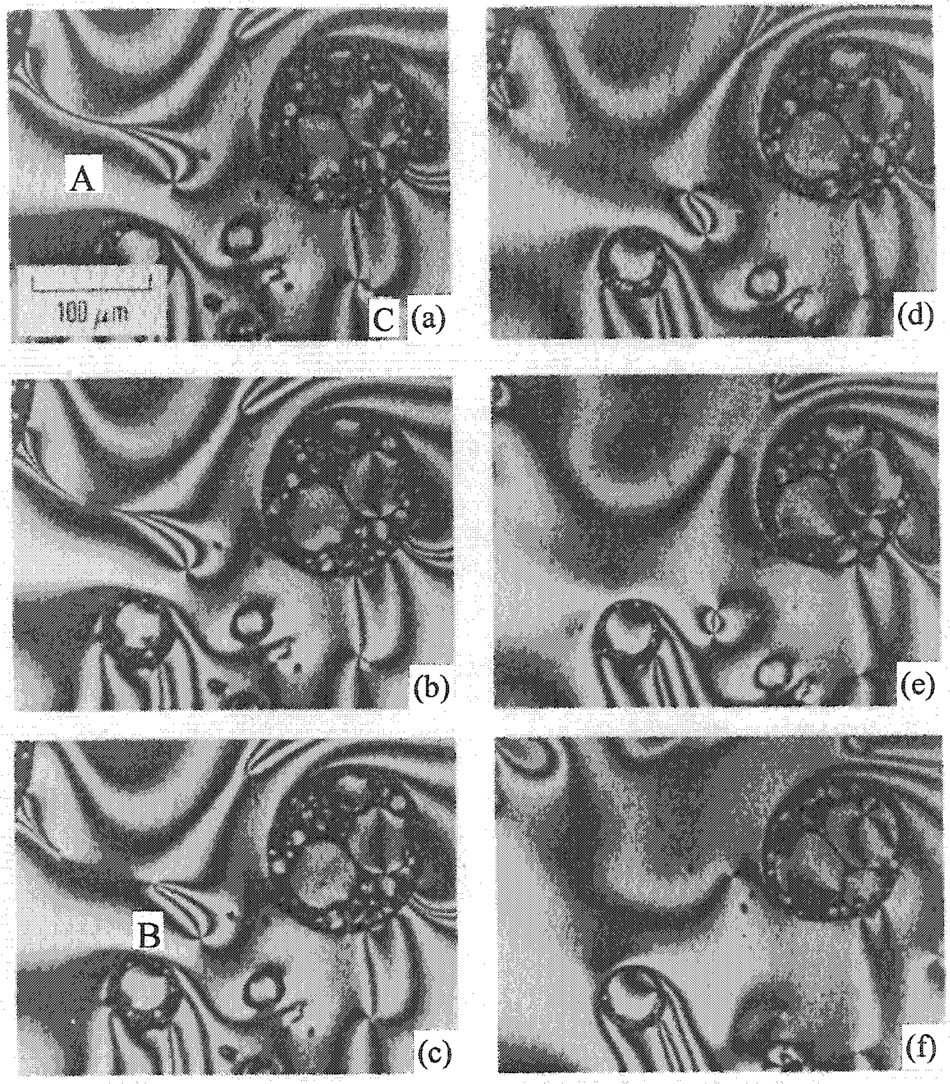

Figure 24: Observation of disclination reactions by hot-stage microscopy (crossed polarizers): (A) generation of $s = +1$ and $s = -1$ disclinations; (B) annihilation of $s = +1$ and $s = -1$ disclinations; (C) disclination reaction $(s = +1/2) + (s = -1) \rightarrow (s = -1/2)$. Adapted from [10].

As explained above, after a symmetry breaking phase transition the mesophase exhibits a distribution of defects of various strengths. Textures undergo a coarsening processes involving defect-defect reactions and annihilations. This phenomenon is shown in figure 24. It shows the nucleation of $s=+1$ and $s=-1$ disclinations which annihilate each other. Further it shows the reaction of $s=+\frac{1}{2}$ and $s=-1$ into a disclination of strength $s=-\frac{1}{2}$ as shown in the spatial sketch in figure 25.

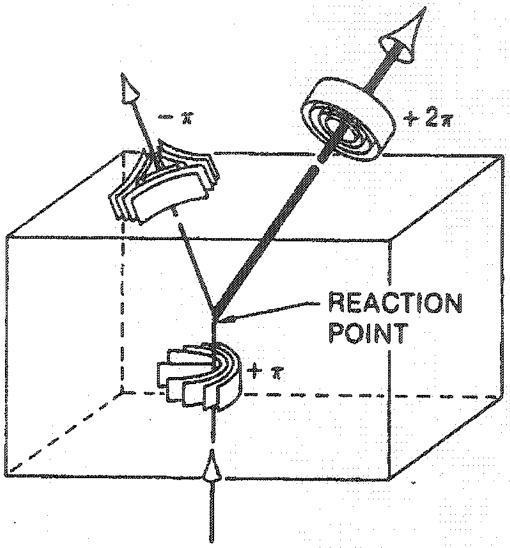

Figure 25: Spatial sketch of a disclination reaction in bulk mesophase showing the reaction. Adapted from [10].

Thus texture coarsening is driven by a defect density reduction. Also as the disclination energy is proportional to s^2 (square of the strength) and since the most commonly observed defects in CMs are $s=\pm\frac{1}{2}$ and $s=\pm 1$ [10]. This should dictate an abundance of $s=\pm\frac{1}{2}$ defects as compared to defects of $s=\pm 1$. The defect-defect reactions and annihilations that drive texture coarsening have been documented by Zimmer and White [10]. They report the observation of the following wedge disclination interactions:

$$\begin{aligned}
s=+1 \;+\; s=-\tfrac{1}{2} &\rightleftharpoons s=+\tfrac{1}{2}\\
s=-1 \;+\; s=+\tfrac{1}{2} &\rightleftharpoons s=-\tfrac{1}{2}\\
s=+\tfrac{1}{2} + s=-\tfrac{1}{2} &\rightleftharpoons 0\\
s=+1 \;+\; s=-1 &\rightleftharpoons 0\\
s=+\tfrac{1}{2} + s=+\tfrac{1}{2} &\rightleftharpoons s=+1\\
s=-\tfrac{1}{2} \;+\; s=-\tfrac{1}{2} &\rightleftharpoons s=-1
\end{aligned}\qquad (2.15a,b,c,d,e,f)$$

These disclinations reactions were observed on the free surface of a CM and provide an important insight into bulk reactions. Moreover the recovery by defect annihilation was rapid when the mesophase was quite fluid. As the viscosity increased by continued pyrolysis, the extent of recovery decreased, leaving increasingly fine deformed microstructures in the hardening mesophase. They made the critical observation that deformation processes can be imposed on the mesophase well beyond the point at which disclinations interact appreciably. This explains the relatively high densities of disclinations in carbon products. The focus in this thesis will be on the commonly observed disclinations ($s = \pm\frac{1}{2}$ and $s = \pm 1$) in mesophases and their interactions.

2.4 Governing Equations and Mathematical Model

The use of vector theory which uses a unit vector **u** to describe the orientation excludes from the problem formulation interesting physics and experimentally observed behaviors which occur in LCs. This is because there are inherent drawbacks in the vector theory. First it carries no information on the deviations from a perfect uniaxial state. Also any realistic model of LCs has to account for changes in the degree of orientation communicated through the scalar order parameter S or tensor order parameter **Q** (defined earlier in section 2.1) in order to be able to predict phase transition. Moreover, one cannot describe a biaxial LC (i.e. a LC with two characteristic directions of orientation). This is especially true in regions around the defects, which are predominantly biaxial. Thus, a tensor theory model including homogeneous (space-independent) and the non-homogeneous (Frank gradient elasticity) is needed for a systematic study of liquid crystals. In order to unify the representation of elastic and thermal free energy, de Gennes [26] wrote a second order tensor representation of free energy density in terms of **Q** and gradients of **Q** given by

$$\begin{aligned} f &= \frac{1}{2}\mathrm{A}\,\mathrm{tr}\left(\mathbf{Q}^2\right) + \frac{1}{3}\mathrm{B}\,\mathrm{tr}\left(\mathbf{Q}^3\right) + \frac{1}{4}\mathrm{C}\,\mathrm{tr}\left(\mathbf{Q}^2\right)^2 + \ldots. \\ &\quad + \frac{1}{2}L_1 \mathbf{Q}_{\alpha\beta,\gamma}\mathbf{Q}_{\alpha\beta,\gamma} + \frac{1}{2}L_2 \mathbf{Q}_{\alpha\beta,\beta}\mathbf{Q}_{\alpha\gamma,\gamma} + \frac{1}{2}L_3 \mathbf{Q}_{\alpha\beta}\mathbf{Q}_{\gamma\delta,\alpha}\mathbf{Q}_{\gamma\delta,\beta} = \mathrm{F}^{\mathrm{h}} + \mathrm{F}^{\mathrm{e}} \end{aligned} \qquad (2.16)$$

The homogeneous F^{h} (short-range) and elastic F^{e} (long-range) free energy contributions are given by:

$$\mathrm{F}^{\mathrm{h}} = \frac{1}{2}\mathrm{A}(\mathbf{Q}{:}\mathbf{Q}) + \frac{1}{3}\mathrm{B}\left(\mathbf{Q}{:}(\mathbf{Q}\cdot\mathbf{Q})\right) + \frac{1}{4}\mathrm{C}\operatorname{tr}\left(\mathbf{Q}{:}\mathbf{Q}\right)^{2} \qquad (2.17)$$

A, B and C are phenomenological coefficients and C must be positive in order for the homogeneous energy to have a minimum.

$$\mathrm{F}^{\mathrm{e}} = \frac{1}{2}L_1\left(\nabla\mathbf{Q}\right)\vdots\left(\nabla\mathbf{Q}\right)^{\mathrm{T}} + \frac{1}{2}L_2\left(\nabla\cdot\mathbf{Q}\right)\cdot\left(\nabla\cdot\mathbf{Q}\right) + \frac{1}{2}L_3\mathbf{Q}{:}\left(\nabla\mathbf{Q}{:}\nabla\mathbf{Q}\right) \qquad (2.18)$$

Where L_1, L_2 and L_3 are elastic constants similar to Frank's elastic constants presented earlier (see section 2.2). The elastic free energy density includes all three invariants. When we include terms of order higher than two in $\mathbf{Q}$ then the expression written in equation (2.18) is no longer unique. There are six independent L_3 terms to be found in the literature [28]. One of these six terms is: $\mathbf{Q}_{\alpha\beta}\mathbf{Q}_{\gamma\delta,\alpha}\mathbf{Q}_{\gamma\delta,\beta}$ (shown in equation 2.18) which is able to reproduce experimental data. In the above written expression for the elastic free energy density we have a one-to-one correspondence between tensor theory elastic constants and the Frank elastic constants from the vector theory in the uniaxial limit (P=0). The relations can be written as follows [1]:

$$L_1 = \frac{3K_{22} - K_{11} + K_{33}}{6S^2};\ L_2 = \frac{K_{11} - K_{22}}{S^2};\ \text{and } L_3 = \frac{K_{33} - K_{11}}{2S^3} \qquad (2.19\text{a, b, c})$$

In addition the third order L_3 term in elastic free energy contribution eqn.(2.18) can be omitted under the assumption that splay elastic constant (K_{11}) is equal to the bend elastic constant (K_{33}). In case of Dirichlet boundary condition used in our work, this assumption simplifies the problem without loss of generality [29]. After omitting L_3 terms and retaining terms up to second order in $\mathbf{Q}$, the relationship between our reduced elastic constants L_1 and L_2 to Frank's elastic constants simplifies to [1]:

$$L_1 = \frac{K_{22}}{2S^2} \text{ and } L_1 = \frac{K - K_{22}}{S^2};\ K = K_{11} \text{or } K_{33} \qquad (2.20\text{ a, b})$$

But the simplified equations impose an additional constraint of equal splay and bend elastic constants ($K_{11} = K_{33}$) on the system. In addition thermodynamic stability considerations impose the following inequality:

$$L_1 > 0, \quad 3L_1 + 5L_2 > 0 \tag{2.21}$$

Another restriction imposed on the elastic constant is $L_2 < 0$ due to the molecular geometry involved (because of disc-like molecules).

In order to obtain the equilibrium configuration of discotic nematic liquid crystals (DNLCs), we should minimize the free energy for all the variations of **Q**. For this purpose, we must derive its variational derivative. This can be mathematically expressed in terms of time evolution of **Q** as [30]:

$$-\gamma(\mathbf{Q})\frac{\mathrm{d}\mathbf{Q}}{\mathrm{dt}} = \frac{\delta \mathrm{F}}{\delta \mathbf{Q}} = \left[\frac{\partial f}{\partial \mathbf{Q}} - \nabla \cdot \frac{\partial f}{\partial \nabla \mathbf{Q}}\right]^{[\mathrm{S}]} \tag{2.22}$$

Where $[\mathrm{S}]$ indicates symmetric and traceless properties, $\gamma(\mathbf{Q})$ is the rotational viscosity coefficient, and $\frac{\delta \mathrm{F}}{\delta \mathbf{Q}}$ is the functional derivative of the total free energy density (both homogeneous and elastic energy). For the phenomenological coefficients A, B, and C in the short-range energy, Doi [30] proposed the following expressions:

$$\mathrm{A} = \frac{ckT}{2}\left(1 - \frac{\mathrm{U}}{3}\right); \ \mathrm{B} = -ckT\frac{\mathrm{U}}{3}; \ \mathrm{C} = ckT\frac{\mathrm{U}}{4} \tag{2.23a, b, c}$$

In the above expressions c is the number density of the discs, k is the Boltzman's constant, and U is the nematic potential, an indication of the stability of the nematic phase. In other words as U increases the temperature decreases. It is given by $\mathrm{U} = \frac{3T^*}{T}$, where T^* is a reference temperature just below the isotropic-nematic phase transition. Substituting the expressions for the homogeneous and elastic energy (namely equations 2.17 and 2.18) into equation (2.22) yields the following expression for **Q** as a function of time and space:

$$\frac{d\mathbf{Q}}{dt} = -6\overline{\mathrm{D}_r}\left\{\left(1-\frac{\mathrm{U}}{3}\right)\mathbf{Q} - \mathrm{U}\left(\mathbf{Q}\cdot\mathbf{Q}-\tfrac{1}{3}(\mathbf{Q}:\mathbf{Q})\delta\right)+\mathrm{U}(\mathbf{Q}:\mathbf{Q})\mathbf{Q}\right\} \tag{2.24a}$$
$$+6\overline{\mathrm{D}_r}\left\{\frac{L_1}{ckT}\nabla^2\mathbf{Q}+\frac{L_2}{2ckT}\left(\nabla(\nabla\cdot\mathbf{Q})+\left[\nabla(\nabla\cdot\mathbf{Q})\right]^{\mathrm{T}}-\frac{2}{3}\mathrm{tr}\left[\nabla(\nabla\cdot\mathbf{Q})\right]\delta\right)\right\}$$

$$\overline{\mathrm{D}_r} \approx \mathrm{D}_r\frac{1}{\left(1-(3/2)\mathbf{Q}:\mathbf{Q}\right)^2};\quad \overline{\mathrm{D}_r}=\frac{ckT}{6\eta} \tag{2.24b}$$

Where $\overline{\mathrm{D}_r}$ is the rotational diffusivity coefficient and is a function of the microstructure; D_r is the pre-averaged rotational diffusivity or isotropic diffusivity independent of the microstructure and η is the viscosity of the material. By comparing equations (2.22) and (2.24b) the relation between $\gamma(\mathbf{Q})$ and $\overline{\mathrm{D}_r}$ can be deduced and $\overline{\mathrm{D}_r}$ is a driving force coefficient similar to the ones found in other diffusion phenomena since our governing equation is a gradient system where evolution is dictated by energy minimization.

Generally, it is useful to introduce a scaling or non-dimensionalization into the Landau de Gennes minimization problem to bring out the characteristic length and time scales. Thus, from here on we will non-dimensionlize our governing equation and solve the derived scaled equation. The scaling of the governing equation (2.24a) is worked out below:

$$\frac{d\mathbf{Q}}{dt} = -\frac{6\mathrm{D}_r}{\left(1-\frac{3}{2}\mathbf{Q}:\mathbf{Q}\right)^2}\left\{\left(1-\frac{\mathrm{U}}{3}\right)\mathbf{Q} - \mathrm{U}\left(\mathbf{Q}\cdot\mathbf{Q}-\tfrac{1}{3}(\mathbf{Q}:\mathbf{Q})\delta\right)+\mathrm{U}(\mathbf{Q}:\mathbf{Q})\mathbf{Q}\right\} \tag{2.25}$$
$$+\frac{6\mathrm{D}_r}{\left(1-\frac{3}{2}\mathbf{Q}:\mathbf{Q}\right)^2}\left\{\frac{L_1}{ckT}\nabla^2\mathbf{Q}+\frac{L_2}{2ckT}\left(\nabla(\nabla\cdot\mathbf{Q})+\left[\nabla(\nabla\cdot\mathbf{Q})\right]^{\mathrm{T}}-\frac{2}{3}\mathrm{tr}\left[\nabla(\nabla\cdot\mathbf{Q})\right]\delta\right)\right\}$$

$$\left(1-\tfrac{3}{2}\mathbf{Q}:\mathbf{Q}\right)^2\frac{d\mathbf{Q}}{d\tilde{t}} = -6\left\{\left(1-\frac{\mathrm{U}}{3}\right)\mathbf{Q} - \mathrm{U}\left(\mathbf{Q}\cdot\mathbf{Q}-\tfrac{1}{3}(\mathbf{Q}:\mathbf{Q})\delta\right)+\mathrm{U}(\mathbf{Q}:\mathbf{Q})\mathbf{Q}\right\} \tag{2.26}$$
$$+\frac{2L_1\times\mathrm{U}}{H^2ckT^*}\left\{\tilde{\nabla}^2\mathbf{Q}+\frac{L_2}{2L_1}\left(\tilde{\nabla}(\tilde{\nabla}\cdot\mathbf{Q})+\left[\tilde{\nabla}(\tilde{\nabla}\cdot\mathbf{Q})\right]^{\mathrm{T}}-\frac{2}{3}\mathrm{tr}\left[\tilde{\nabla}(\tilde{\nabla}\cdot\mathbf{Q})\right]\delta\right)\right\}$$

$$\left(1-\tfrac{3}{2}\mathbf{Q}:\mathbf{Q}\right)^2\frac{\mathrm{d}\mathbf{Q}}{\mathrm{d}\tilde{\mathrm{t}}}=-6\left\{\left(1-\frac{\mathrm{U}}{3}\right)\mathbf{Q}-\mathrm{U}\left(\mathbf{Q}\cdot\mathbf{Q}-\tfrac{1}{3}(\mathbf{Q}:\mathbf{Q})\delta\right)+\mathrm{U}(\mathbf{Q}:\mathbf{Q})\mathbf{Q}\right\} \tag{2.27}$$

$$+\frac{\mathrm{U}}{R}\left\{\tilde{\nabla}^2\mathbf{Q}+\widetilde{L_2}\left(\tilde{\nabla}\left(\tilde{\nabla}\cdot\mathbf{Q}\right)+\left[\tilde{\nabla}\left(\tilde{\nabla}\cdot\mathbf{Q}\right)\right]^{\mathrm{T}}-\frac{2}{3}\mathrm{tr}\left[\tilde{\nabla}\left(\tilde{\nabla}\cdot\mathbf{Q}\right)\right]\delta\right)\right\}$$

where the quantities with $\left(\;\tilde{}\;\right)$ represent their dimensionless form. The different dimensionless parameters that emerge out of the above equation are $R=\dfrac{H^2ckT^*}{2L_1}$, $\mathrm{U}=\dfrac{3T^*}{T}$ and $\widetilde{L_2}=\dfrac{L_2}{L_1}$. The dimensionless parameter R represents the ratio of short-range order elasticity and long-range order elasticity [31], and also the short-range (internal) time scale and long-range (external) time scale. Moreover R $\left(R\approx\dfrac{H^2}{\xi^2}\right)$ scales as the square of the ratio of the fiber radius (macroscopic length scale H) to the molecular length scale (microscopic length scale ξ). The molecular length scale is given as $\xi=\sqrt{\dfrac{L_1}{ckT^*}}$ and H representing the fiber radius is the macroscopic length scale. The quantity $\dfrac{3T^*}{T}$ is the dimensionless temperature denoted by U and also known as the nematic potential describing the extent of the stability of the nematic phase. A high value of U indicates a low temperature. For U<8/3, the stable phase is isotropic, for $8/3 \leq \mathrm{U} \leq 3$ there is biphasic equilibrium, and for nematic potential greater than three (U>3) the stable phase is uniaxial nematic. It also governs the equilibrium value of the scalar order parameter S that the system will tend to achieve. An expression relating the nematic potential U to the scalar order parameter put forward by Doi [30] is given below:

$$S_{eq}=\frac{1}{4}+\frac{3}{4}\sqrt{\left(1-\frac{8}{3\mathrm{U}}\right)} \tag{2.28}$$

The third dimensionless parameter is $\widetilde{L_2}=\dfrac{L_2}{L_1}$, the ratio of the two elastic constants and is a measure of the elastic anisotropy of the material. As mentioned before, the exclusion of L_3 terms in our governing equation restricts the Frank elastic constants to $K_{11} = K_{33}$ [1] (splay is equal to the bend) but if in addition we put $L_2 = 0$ in our equation then we end up with the relation $K_{11} = K_{22} = K_{33}$ (i.e. splay elastic constant is equal to the twist and bend elastic constants). In other words a case of isotropic elasticity meaning the system does not gain any special advantage by opting for a specific mode of deformation. The dimensionless parameter R is ratio of the two length scales (internal and external) or can also be expressed as the ratio of two time scales, because R controls the relative magnitudes of the short-range and long-range order elasticity. A change in R causes a change in their relative magnitude and consequently in their ability to impose uniaxiality (short-range) and minimize gradients (long-range) thus leading to a change in the time scales of these two phenomena. The two length scales can be written as:

$$\mathrm{L_e} = H; \text{ and } \mathrm{L_i} = \xi = \sqrt{\frac{L_1}{ckT^*}} \qquad (2.29)$$

The external length scale is usually the fiber radius and the internal length scale represents the characteristic length over which the scalar order parameter varies and is usually much smaller than the fiber radius ($\mathrm{L_i} \ll \mathrm{L_e}$). The internal length scale is related to the evolution of scalar order parameters S and P and the external length is related to the gradients of the tensor order parameter $\mathbf{Q}$. On the other hand the time scales can be represented as:

$$\tau_\mathrm{i} = \frac{\eta}{ckT^*}; \text{ and } \tau_\mathrm{e} = \frac{\eta H^2}{L_1} \qquad (2.30)$$

Similar to the length scales, the internal time scale is much smaller than the external time scale ($\tau_\mathrm{i} \ll \tau_\mathrm{e}$). The internal time scale τ_i governs the scalar order parameters and external time scale τ_e governs the evolution of the orientation of the molecules (represented by the director $\mathbf{n}$).

The governing equation for our mathematical model is equation (2.27) along with its dimensionless parameters namely R ratio of the short-range order elasticity to the long-range order elasticity, U the nematic potential, and $\widetilde{L_2}$ the elastic anisotropy. The governing equation is a set of non-linear coupled diffusion reaction partial differential equations describing the evolution of the microstructure. For simplicity, from here on we will omit $\left(\tilde{\ }\right)$ denoting dimensionless quantities in our governing equation. This set of partial differential equations will be solved numerically to study the stability of different carbon fiber microstructures under different parametric (U, R, L_2) conditions. A short description of the solution methodology along with the numerical methods used is given below.

2.5 Numerical Methodology of Solution

The types of mathematical models encountered by scientists and engineers may be as simple as solving a system of linear algebraic equations or as difficult as solving a set of partial differential equations in three spatial coordinates, in addition to the time coordinate. While the derivation of the governing equations is not unduly difficult, their solution by exact methods of analysis is a formidable task in itself. In such cases alternative methods of analysis provide the means of finding approximate solutions. These methods are commonly known as numerical methods or computational methods since the majority of them make use of computers for doing the computation work involved in these methods. One of these, the Galerkin Finite Element Method (GFEM) has been widely used for solving problems governed by ordinary differential equations, partial differential equations and integral equations in many applications [32]. When we suppose that the given differential equation with appropriate initial condition and boundary conditions in two dimensions can be expressed as:

$$L(u) = 0 \tag{2.31}$$

in a domain ***D*** (*x,y*). The Galerkin method assumes that u can be accurately represented by an approximate solution as:

$$u_a(x,y,t) = \sum_{j=1}^{N} u_j(t)\varphi_j(x,y) \tag{2.32}$$

where φ_js are known analytical functions, called global trial and test functions and u_js are time dependent unknown coefficients. Replacing u in eqn. (2.32) with u_a in eqn. (2.31), we obtain the following expression:

$$L(u_a) = \mathrm{R} \neq 0 \tag{2.33}$$

where R is the residual. An approximate solution u_a is assumed to be composed of piecewise approximate functions, so that if the piecewise approximation is correctly constructed, then it will approach the corresponding exact solution u. In other words, the aim of the method of residual is to force R to zero and consequently make an approximate solution u_a approach the exact solution. To do this, we need to set the inner product of the residual R and an independent weight function w_i equal to zero:

$$F_i = \iint_D \mathrm{R}\varphi_i(x,y)\mathrm{dA} = \iint_D L(u_a)w_i(x,y)\mathrm{dA} = 0 \tag{2.34}$$

In the Galerkin method, the weight function w_i is chosen from the same family of functions as the global test and trial functions in eqn. (2.32), hence eqn. (2.34) can be rewritten as:

$$F_i = \iint_D \mathrm{R}w_i(x,y)\mathrm{dA} = \iint_D L(u_a)\varphi_i(x,y)\mathrm{dA} = 0 \tag{2.35}$$

where $i, j = 1,2,\ldots N$. Note that the equation (2.33) can be expressed as a set of N differential equations to be solved for the unknown coefficients u_a when we apply Gaussian integration. Consequently, equation (2.31) has been reduced to a set of ordinary differential equations (2.35).

In this thesis, the given differential equation $L(\mathbf{Q})$ is represented by the governing equation (2.27) and can be rewritten as:

$$\begin{aligned}&\left(1-\tfrac{3}{2}\mathbf{Q}:\mathbf{Q}\right)^2\frac{\mathrm{d}\mathbf{Q}}{\mathrm{dt}}+6\left\{\left(1-\frac{\mathrm{U}}{3}\right)\mathbf{Q}-\mathrm{U}\left(\mathbf{Q}\cdot\mathbf{Q}-\tfrac{1}{3}(\mathbf{Q}:\mathbf{Q})\delta\right)+\mathrm{U}(\mathbf{Q}:\mathbf{Q})\mathbf{Q}\right\} \\ &\quad -\frac{\mathrm{U}}{R}\left\{\nabla^2\mathbf{Q}+L_2\left(\nabla(\nabla\cdot\mathbf{Q})+\left[\nabla(\nabla\cdot\mathbf{Q})\right]^{\mathrm{T}}-\frac{2}{3}\mathrm{tr}\left[\nabla(\nabla\cdot\mathbf{Q})\right]\delta\right)\right\}=0\end{aligned} \tag{2.35}$$

After obtaining the residual and taking its inner product with weight functions similar to that represented in eqn. (2.35) leads to the following equation:

$$
\begin{aligned}
F_i = & \iint\limits_D \left[\left(1-\tfrac{3}{2}\mathbf{Q}:\mathbf{Q}\right)^2 \frac{\mathrm{d}\mathbf{Q}}{\mathrm{dt}} \right] \varphi_i \mathrm{dxdy} \\
& + \iint\limits_D 6 \left\{ \left(1-\frac{\mathrm{U}}{3}\right)\mathbf{Q} - \mathrm{U}\left(\mathbf{Q}\cdot\mathbf{Q}-\tfrac{1}{3}(\mathbf{Q}:\mathbf{Q})\delta\right) + \mathrm{U}(\mathbf{Q}:\mathbf{Q})\mathbf{Q} \right\} \varphi_i \mathrm{dxdy} \\
& - \iint\limits_D \left[\frac{\mathrm{U}}{R} \left\{ \nabla^2\mathbf{Q} + L_2\left(\nabla(\nabla\cdot\mathbf{Q}) + \left[\nabla(\nabla\cdot\mathbf{Q})\right]^{\mathrm{T}} - \frac{2}{3}\mathrm{tr}\left[\nabla(\nabla\cdot\mathbf{Q})\right]\delta \right) \right\} \right] \varphi_i \mathrm{dxdy} = 0
\end{aligned}
\tag{2.37}
$$

Applying the following tensor identities and the divergence theorem to equation (2.37) to simplify the equation as well as lower the order of the derivatives involved.

$$\nabla^2\mathbf{Q}\varphi = \nabla\cdot(\nabla\mathbf{Q}\varphi) - \nabla\varphi\cdot\nabla\mathbf{Q} \tag{2.38a}$$

$$\left[\nabla(\nabla\cdot\mathbf{Q})\right]\varphi = \nabla\left[(\nabla\cdot\mathbf{Q})\varphi\right] - (\nabla\varphi)(\nabla\cdot\mathbf{Q}) \tag{2.38b}$$

$$\left[\nabla(\nabla\cdot\mathbf{Q})\right]^{\mathrm{T}}\varphi = \left[\nabla(\nabla\cdot\mathbf{Q})\varphi\right]^{\mathrm{T}} \tag{2.38c}$$

$$\left[\nabla(\nabla\cdot\mathbf{Q})\varphi\right]^{\mathrm{T}} = \left[\nabla\{(\nabla\cdot\mathbf{Q})\varphi\}\right]^{\mathrm{T}} - \left[(\nabla\varphi)(\nabla\cdot\mathbf{Q})\right]^{\mathrm{T}} \tag{2.38d}$$

$$(vw)^{\mathrm{T}} = (wv) \tag{2.38e}$$

$$\iint\limits_D \alpha\nabla\cdot v\mathrm{dA} = \oint\limits_S \alpha\mathbf{n}\cdot v\mathrm{dS} - \iint\limits_D \nabla\alpha\cdot v\mathrm{dA} \tag{2.38f}$$

where v,w represent vector quantities and equation (2.38f) represents the divergence theorem which relates the total flux of a vector field out of a surface S surrounding a finite volume V to the properties of the field inside the volume. Therefore, the equation that we obtain can be expressed as:

$$
\begin{aligned}
F_i = & \iint\limits_D \left[\left(1-\tfrac{3}{2}\mathbf{Q}:\mathbf{Q}\right)^2 \frac{\mathrm{d}\mathbf{Q}}{\mathrm{dt}} \right] \varphi_i \mathrm{dxdy} \\
& + \iint\limits_D \left[6 \left\{ \left(1-\frac{\mathrm{U}}{3}\right)\mathbf{Q} - \mathrm{U}\left(\mathbf{Q}\cdot\mathbf{Q}-\tfrac{1}{3}(\mathbf{Q}:\mathbf{Q})\delta\right) + \mathrm{U}(\mathbf{Q}:\mathbf{Q})\mathbf{Q} \right\} \varphi_i + \frac{\mathrm{U}}{R}\left\{(\nabla\varphi_i)\cdot(\nabla\mathbf{Q})\right\} \right] \mathrm{dxdy} \\
& + \iint\limits_D \left[\frac{\mathrm{U}L_2}{R} \left((\nabla\varphi_i)(\nabla\cdot\mathbf{Q}) + (\nabla\cdot\mathbf{Q})(\nabla\varphi_i) - \frac{2}{3}\mathrm{tr}\left[(\nabla\varphi_i)(\nabla\cdot\mathbf{Q})\right]\delta \right) \right] \mathrm{dxdy} = 0 \\
& - \oint\limits_S \left[\frac{\mathrm{U}}{R} \left\{ \mathbf{n}\cdot(\nabla\mathbf{Q}\varphi_i) + L_2\left(\mathbf{n}\left[(\nabla\cdot\mathbf{Q})\varphi_i\right] + \left[(\nabla\cdot\mathbf{Q})\varphi_i\right]\mathbf{n} - \frac{2}{3}\mathrm{tr}\left[\mathbf{n}\{(\nabla\cdot\mathbf{Q})\varphi_i\}\right]\delta \right) \right\} \right] \mathrm{dxdy}
\end{aligned}
\tag{2.39}
$$

where **Q** is expressed as:

$$\mathbf{Q}(x,y,t)=\sum_{j=1}^{N}\mathbf{Q}_j(t)\varphi_j(x,y); \qquad j=1,2,....N \tag{2.40}$$

Once the governing equation has been set up in the Galerkin form, the next step is domain discretization, that is, the domain must be divided into a number of smaller sub-domains, called finite elements as show in figure 26. The dark dots represent the vertices of each element and are also known as nodes.

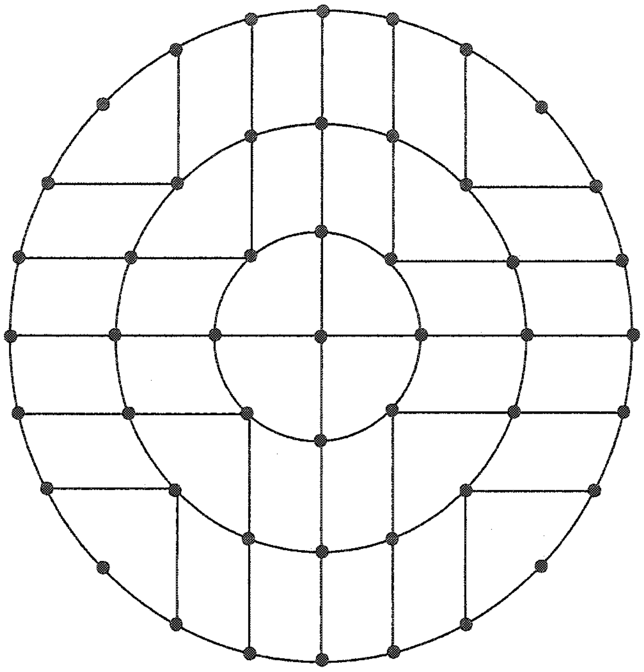

Figure 26: A schematic diagram showing the spatial discretization of our domain into smaller sub-domains called the finite elements. Each dark dot represents a Node. Note that this figure does not depict the actual discretization but is shown as an example.

For two-dimensional problems, either triangles or quadrilaterals can be used as finite elements, depending on the boundary geometry. The number of nodes has to be properly chosen to represent the solution more effectively where rapid changes in the solution are expected. A balance between the number of elements and computational time and memory requirements should also be taken into account.

As shown in equation (2.32), an approximate solution has been expressed as the summation of the product of unknown coefficients u_j(t), also known as the nodal unknowns and the global trial and test functions $\varphi_j(x,y)$. However, in computations, by using the local test and trial functions instead of the global one, the given problems can be solved very economically. This is plausible because the test and trial functions span a very small section of the spatial domain. A schematic representation of two-dimensional global and local domains is shown in figure 27. Where ζ and υ represent the local orthogonal coordinate system.

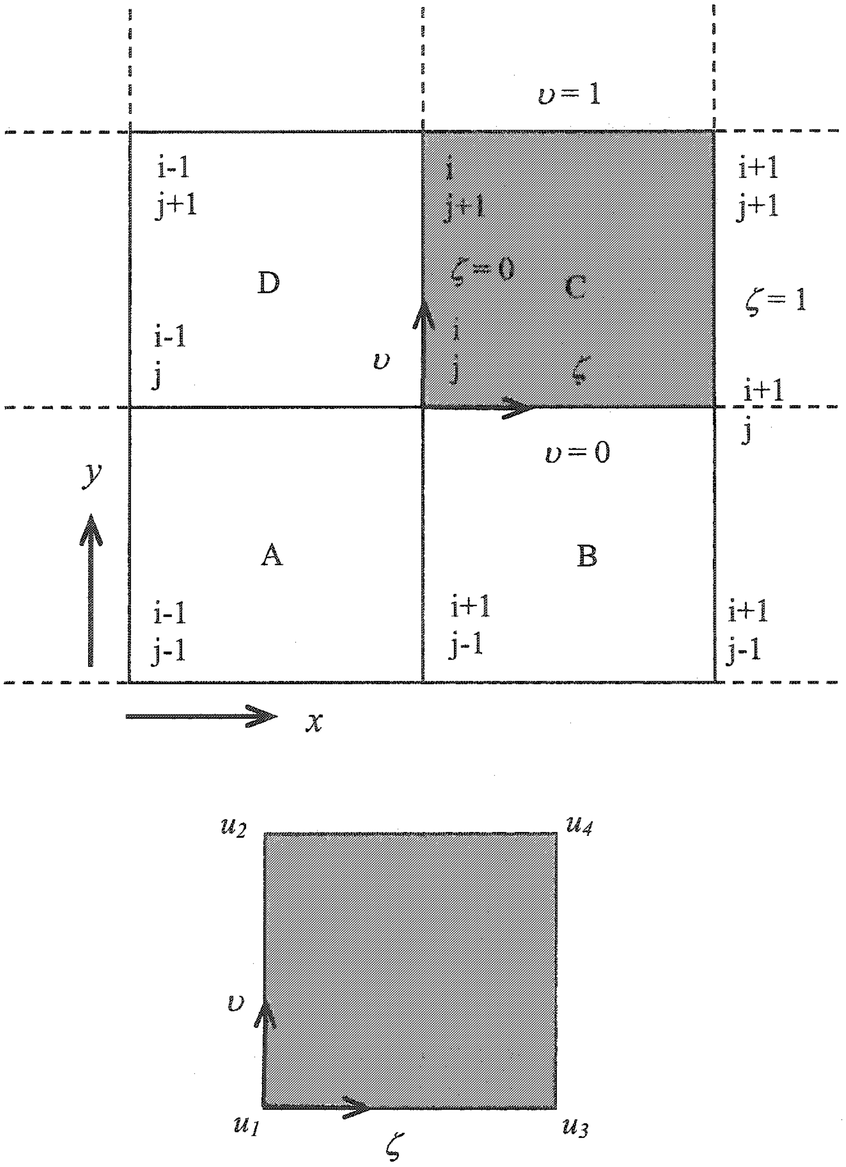

Figure 27: Element configurations in a two-dimensional global domain and corresponding local domain. x and y represent the global two-dimensional coordinate axes while ζ and υ represent the local coordinate axes.

The test and trial functions are non-zero in the vicinity of the node (i, j)th node and zero outside of this range. If local, low order polynomial interpolating functions are used as trial functions then it leads to low-order integrands in evaluating the inner product of the residual with the weight functions. A lower order integrand permits a lower order quadrature formula to be used. Consequently an important computational economy is achieved when N is large [32].

The elements represented in the representative domain of our problem in figure 26 are not rectangular but quadrilaterals of arbitrary shapes. We need a method to map these arbitrary quadrilaterals into our local orthogonal coordinate system in ξ and η. One such method that we use is called isoparametric mapping. A transformation between physical space (x,y) and the element space (ζ,υ) for a given element (as shown in figure 28) is expressed as:

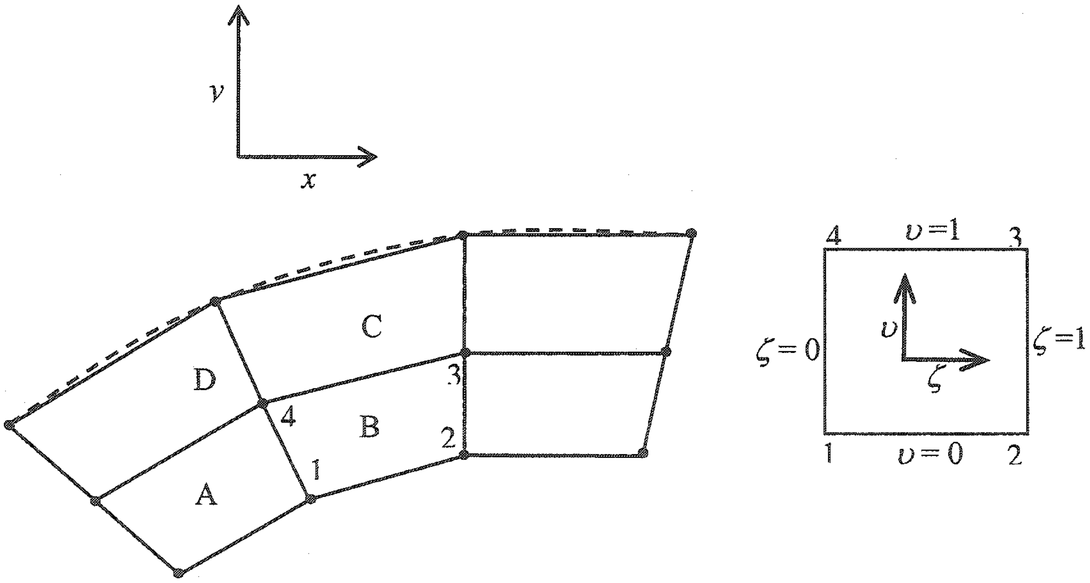

Figure 28: Isoparametric mapping of arbitrary quadrilaterals in the global space to local orthogonal coordinate system ξ and η.

$$x = \sum_{l=1}^{4} \varphi_l(\zeta,\upsilon)\bar{x}_l$$
$$y = \sum_{l=1}^{4} \varphi_l(\zeta,\upsilon)\bar{y}_l \qquad (2.41\text{ a, b})$$

where $\bar{x}_l$ and $\bar{y}_l$ are the coordinates of the lth corner of an element in physical space and $\varphi_l(\zeta,\upsilon)$ are the same interpolating functions as used in the trial functions. Equation (2.41) is called isoparametric transformation. Since it is also easier to evaluate the residual integral in the local (ζ,υ) space, $\partial\varphi_j/\partial x$, $\partial\varphi_j/\partial y$ are related to $\partial\varphi_j/\partial\zeta$, $\partial\varphi_j/\partial\upsilon$ by the following equations:

$$\begin{bmatrix} \dfrac{\partial\varphi_j}{\partial\zeta} \\ \dfrac{\partial\varphi_j}{\partial\upsilon} \end{bmatrix} = [J] \begin{bmatrix} \dfrac{\partial\varphi_j}{\partial x} \\ \dfrac{\partial\varphi_j}{\partial y} \end{bmatrix} \tag{2.42}$$

where the Jacobian J is the matrix of transformation from the global to the local coordinates and J is given by

$$[J] \equiv \begin{bmatrix} \dfrac{\partial x}{\partial\zeta} & \dfrac{\partial y}{\partial\zeta} \\ \dfrac{\partial x}{\partial\upsilon} & \dfrac{\partial y}{\partial\upsilon} \end{bmatrix} \tag{2.43}$$

This completes our mapping to the orthogonal local coordinate system (ζ,υ) and now a short discussion of the test functions is presented below.

The local, low order polynomial interpolating functions that are used as trial functions are also called basis functions. We employ bilinear basis functions for solving our governing equation. The bilinear basis functions are constructed from linear basis functions used for one-dimensional problems. A visual representation of bilinear basis functions is represented in figure 29. Note that the localized basis functions are non-zero only on the concerned node in the local coordinate system as shown in the figure. The four localized basis functions can be expressed as:

$$\begin{aligned} \varphi_1(\zeta,\upsilon) &= (1-\upsilon)(1-\zeta) \\ \varphi_2(\zeta,\upsilon) &= (\upsilon)(1-\zeta) \\ \varphi_3(\zeta,\upsilon) &= (1-\upsilon)(\zeta) \\ \varphi_4(\zeta,\upsilon) &= (\upsilon)(\zeta) \end{aligned} \tag{2.43 a,b,c,d}$$

There are four local basis functions corresponding to the four nodes of the rectangular element and are constructed in such a way so as to fulfill the requirement of being non-zero at the corresponding node and zero at all the other nodes.

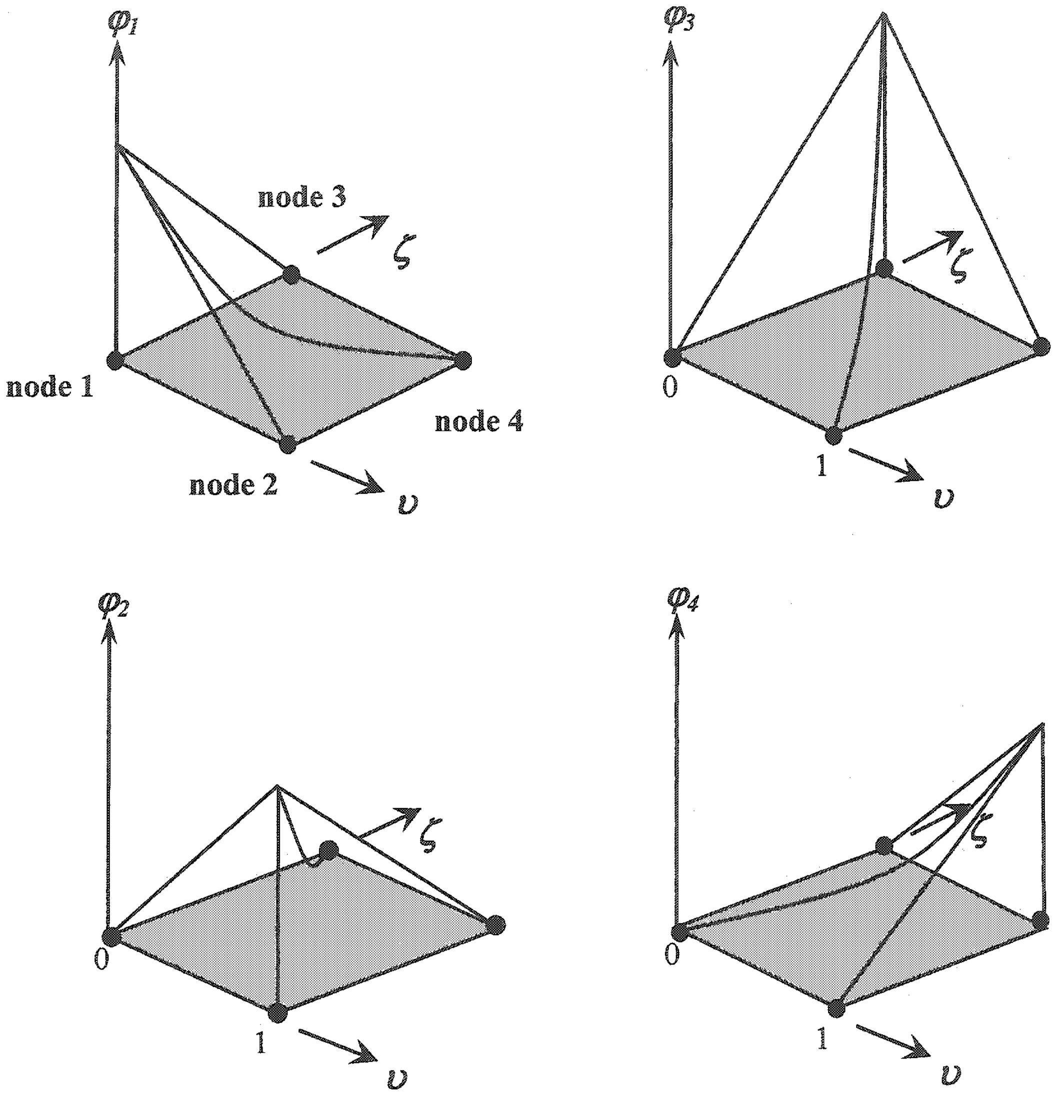

Figure 29: Two dimensional local bilinear basis functions for rectangular elements. Note that there are four basis functions corresponding to each node in the rectangular element. Adapted from [33].

In a two dimensional rectangular mesh (figure 27) the (*i,j*)th node is surrounded by four elements. Approximate solutions can be defined independently in each element using the local coordinate system (ζ,υ). Thus in an element we obtain

$$u=\sum_{j=1}^{4}\varphi_j(\zeta,\upsilon)\,\overline{u}_j \tag{2.44}$$

where $\overline{u}_j$ are the nodal values of u, and φ_j is the interpolating function associated with the jth node. Note that $\overline{u}_j$(j going from 1to 4) defined at the local level becomes $\overline{u}_{i,j}$ at the global level. The above expression can be written for the complete spatial domain as:

$$u=\sum_{i=1}^{N}\sum_{j=1}^{4}\varphi_j(\zeta,\upsilon)\,\overline{u}_{i,j} \tag{2.45}$$

In the above equation the subscript i (1…N) goes over each global element traversing the whole spatial domain whereas the subscript j goes from 1 to 4 representing the mapping of each global element into local element with local bilinear basis functions. Here $\overline{u}_{i,j}$ represents the global nodal unknowns. We can represent eqn. (2.45) in a simpler form by lumping together the coefficients in the above equation as U_i and the basis functions as ψ_i, which gives:

$$u=\sum_{i=1}^{N}U_i\psi_i \tag{2.46}$$

We can obtain a similar equation for **Q** as:

$$\mathbf{Q}=\sum_{i=1}^{N}\mathbf{Q}_i\psi_i \tag{2.47}$$

Inserting equation (2.47) into equation (2.39) and after applying the boundary conditions, we obtain a set of equations in a matrix form given by:

$$\underline{\underline{J}}\cdot\underline{\mathbf{Q}}=-\underline{F} \tag{2.48}$$

where $\underline{\underline{J}}$ is the Jacobian matrix and can be obtained by $J_{i,j}=\partial F_i/\partial \mathbf{Q}_j$ and F_i is given by equation (2.39). Finally the above equation (2.48) is solved for the unknown coefficients $\mathbf{Q}_i$ using the Newton-Raphson iteration scheme. Convergence is assumed when the difference between two consecutive solution vectors is less than 10^{-6}. Moreover a set of non-linear time dependent equations has been reduced to a set of ordinary time dependent differential equation. A first-order implicit Euler predictor-corrector method is used for time descritization [34]. In addition, an adaptive time step control method [33] is used to capture the essential physics of the problem and minimize computing time while maintaining accuracy. Prior to presenting typical examples of stable two-dimensional liquid crystal configurations, some explanation of our visualization technique is presented below.

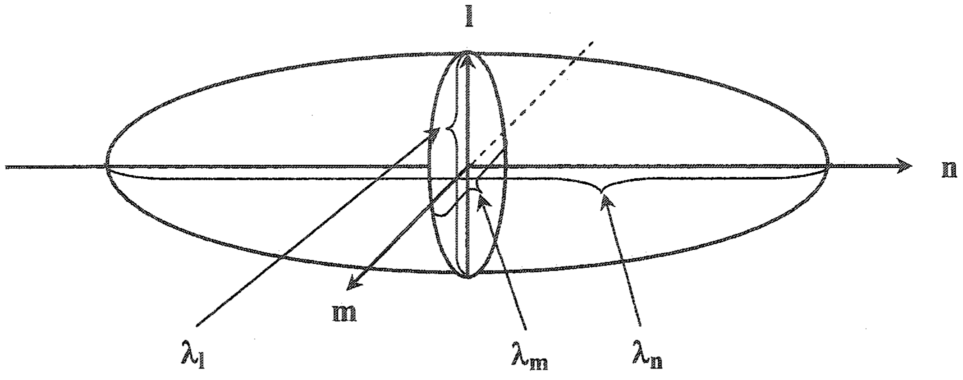

Figure 30: Ellipsoid of visualization, which represents the eigen vectors and eigen values of our tensor order parameter **Q**, which in return help us to depict the orientation of the molecules and degree of orientation in one single picture.

2.6 Visualization Technique

We have seen that a stationary point of the Landau-de Gennes free energy functional is a field, which describes at each point in the domain a symmetric, traceless matrix **Q**. We also recall that **Q** contains all information (at a point) about the preferred direction of orientation of the molecules of the material in question, the nature of fluctuations about this preferred orientation, and the degree of the order of the phase. In other words the three eigen vectors **n**, **m**, **l** of the tensor **Q** provide information on the orientation of the molecules at each of the nodes in our domain. The degree of order in each of these principal directions is given by the three eigen values corresponding to three eigen vectors **n**, **m**, **l**. Since in our case the limiting values of the eigen values can be represented as $-\frac{1}{3} < \lambda_1, \lambda_2, \lambda_3 < \frac{2}{3}$. We scale our eigen values so that limiting values span from zero to one ($0 < \lambda_1, \lambda_2, \lambda_3 < 1$). To represent a solution field, we determine the principal directions of **Q** (the eigen vectors **n**, **m**, **l**) at the nodes of our mesh. As mentioned before a symmetric second order tensor, **Q** can be represented geometrically by a quadratic surface. We then construct an ellipsoid whose principal axes are determined by the three eigen vectors and whose axes lengths are determined by the corresponding eigen values. These ellipsoids then depict not only a preferred direction of orientation (if such a direction exists) of the molecules but also the magnitude of fluctuations about this direction. An example of such a representation is shown in figure 30 and figure 31. We now have all the necessary ingredients to compute the solution field and present the equilibrium configurations of the discotic nematic liquid crystal (DNLC) materials, which we will commence in the next chapter.

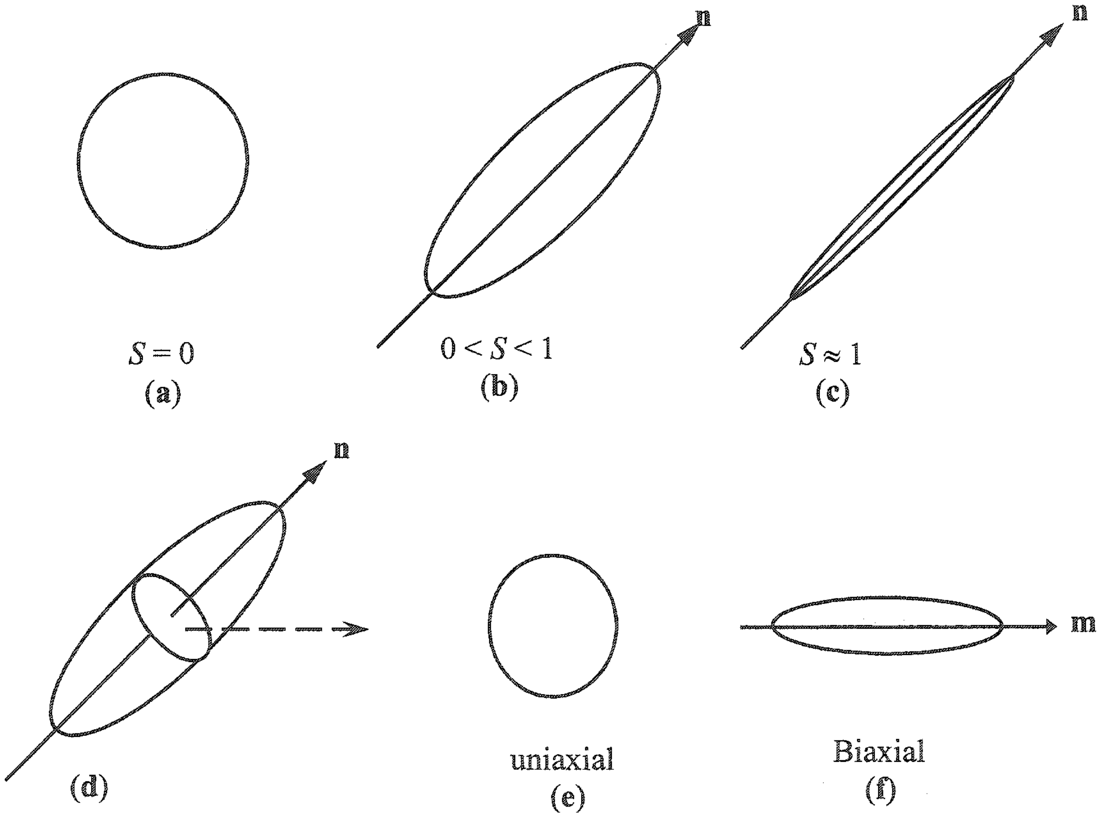

Figure 31: Visualization techniques used for a tensor order parameter. The slenderness of the ellipsoid depicts the degree of order. Thus a circle in (a) represents an ispotropic state and a very slender ellipsoid in (c) represents a high scalar order parameter S. The second row of figures depicts the biaxial order parameter i.e if the cross-section at centre of the ellipsoid is (e) a circle it is uniaxial, otherwise it is biaxial. The principal axes capture the alignment of the molecules.

2.7 Conclusions

A theoretical framework was developed with a brief overview of the basic concepts of the theory of liquid crystals like orientational order, tensor order parameter **Q**, and elastic distortions. An understanding of the concept and theory of disclinations in liquid was developed as disclinations (defects) form the characterizing feature for various microstructures observed in carbon fibers. All these concepts then led to the formulation of a tensor order theory involving **Q** and gradients of **Q** describing the free energy of a liquid crystal system. A governing equation describing the equilibrium configuration of a discotic nematic liquid crystal (DNLC) was obtained from the tensor order theory by minimizing the free energy equation. A set of parameters namely R ratio of the short-range order elasticity to the long-range order elasticity, U the nematic potential, and $\widetilde{L_2}$ the elastic anisotropy were clearly outlined and their physical interpretation explained. This was followed by an explanation of the numerical methods that are used to solve the governing equation especially Galerkin Finite Element Method. The Galerkin Finite Element method was chosen for spatial discretization of the governing equations. In addition, a first-order implicit Euler predictor-corrector method and an adaptive time scheme were chosen for temporal discretization. In summary, a mathematical model describing the microstructure evolution along with the solution methodology based on numerical methods was developed.

Bibliography

[1] Beris A.N., Edwards B.J., *Thermodynamics of flowing systems: with internal microstructure* (Oxford University Press, New York, 1994)

[2] de Gennes P-G., Prost J., *The Physics of Liquid Crystals,* 2nd edition (Clarendon Press, Oxford, 1995)

[3] Stephen M.J., Straley J.P., *Rev. Mod. Phys.* **46,** 617 (1974)

[4] Priestley E.B., Wojtowicz P.J., Sheng P., *Introduction to Liquid Crystals,* (Plenum Press, New York, 1975).

[5] Lubensky T.C., *Phys. Rev. A.,* **2**, 2497 (1970)

[6] Borisenko A.I., and Tarapov I.E., *Vector and Tensor Analysis with Application,* (Prentice-Hall, NJ, 1968)

[7] Frank F.C., *Discuss. Faraday Soc.*, **25**, 19 (1958)

[8] Wang L., and Rey A.D., *Modell. Simul. Mater. Sci. Eng.*, **5**, 67 (1997)

[9] Chandrasekhar S., *Liquid Crystals*, 2nd Edition (Cambridge University Press, Cambridge, 1992)

[10] Zimmer J.E., White J.L., in "*Advances in Liquid Crystals*" **5**, 157 (Academic Press, 1982).

[11] Rey A.D., Tsuji T., *Macromol. Theory Simul.*, **7**, 623 (1998)

[12] Volterra V., *Ann. Sci. Ecole Norm. Sup.*, **24**(3), 401 (1907)

[13] Anisimov S.I., Dzyaloshinskii I.E., *Sov. Phys.-JETP*, **36**, 774 (1972)

[14] Rey A.D., *Phys. Rev. E.*, **51**, 6278 (1995)

[15] Ranganath G.S., *Mol. Cryst. Liquid Cryst.*, **87**, 187(1982)

[16] Ericksen J.L., *Liquid Crystals and Ordered Fluids; proceedings of an American Chemical Society Symposium On Ordered Fluids and Liquid Crystals,* ed. by Johnson J.F., and Porter R. S. (Plenum Press, New York, 1970)

[17] Schopohl N., Sluckin T.J., *J. Phys. France*, **49**, 1097 (1988)

[18] Penzenstadler E., Trebin H.R., *J. Phys. France*, **50**, 1027 (1989)

[19] Hudson S.D., Larson R.G., *Phys. Rev. Lett.*, **70**(9), 2916 (1993)

[20] Sigillo I., Greco F., Marucci G., *Liq. Cryst.*, **24**(3), 419 (1998)

[21] Cladis P., Kleman M., *J. Phys. France*, **33**, 591 (1972)

[22] Rester D.O., Rowe R., *Carbon*, **12**, 218 (1974)

[23] Ihnatowicz M., Chiche P., Deduit J., Pregermain S., and Tournant R., *Carbon*, **4**, 41 (1966)

[24] Hoover D.S., Davis A., Perrotta A.J., and Spackman W., *Extended abstract published in the Proceedings of the 20th Biennial Conference on Carbon*, 393, Pennsylvania, USA (1979)

[25] White J.L., Buechler M., *"Microstructure formation in mesophase carbon fibers and other graphitic materials"*, *Petroleum-Derived Carbons,* ed. by Bacha J.S., Newman J.W., White J.L., ACS Symp. Ser., **303**, 62 (1986)

[26] de Gennes P-G., *Mol. Cryst. Liq. Cryst.*, **12**, 193 (1971)

[27] Longa L., Monselesan D., Trebin H.R., *Liq. Cryst.*, **2** (6), 769 (1987)

[28] Schiele K., Trimper S., *Phys. Status Solidi B*, **118**, 267 (1983)

[29] Gartland (Jr.) E.C., Palffy-Muhoray P., and Varga R.S., *Mol. Cryst. Liq. Cryst.*, **199**, 429 (1991)

[30] Doi M., Edwards S.F., *The Theory Of Polymer Dynamics* (Clarendon Press, Oxford 1987)

[31] Tsuji T., Rey A.D., *J. Non Newtonian Fluid Mech.*, **73**, 127 (1997)

[32] Fletcher C.A.J., *Computational Galerkin Methods* (Springer-Verlag, New York 1983)

[33] Hunter P., FEM/BEM Notes, The University Of Auckland (URL: http://www.esc.auckland.ac.nz/Academic/Texts/fembemnotes.pdf)

[34] Finalayson B.A., *Nonlinear Analysis in Chemical Engineering* (McGraw-Hill, London 1980)

Chapter 3

Computer Simulation of Texture Formation in Carbon Fibers

3.1 Introduction

A mathematical model has been developed for the time evolution of carbon fiber microstructure based on the classical Landau-de Gennes theory. The mathematical model is based on the tensorial description of the microstructure and always yields a smooth solution even if the director field is discontinuous. This model is also able to capture biaxiality observed around the disclination regions [1]. Moreover, the more common director description is more suitable for problems with a constant order parameter. This chapter is devoted to the numerical study of the Landau-de Gennes free energy equation that includes the bulk terms as well as the spatial variations of the tensor order parameter **Q**, for a circular geometry. The study of liquid crystals in cylindrical confinement is of interest because the carbon fibers have cylindrical geometry and numerical computation offers a better alternative to superior product design based on understanding of the carbon fiber microstructure.

3.2 Governing Equations and Auxiliary Conditions

The results presented in this chapter are based on the numerical solution to the following equation:

$$\left(1-\tfrac{3}{2}\mathbf{Q}:\mathbf{Q}\right)^2\frac{d\mathbf{Q}}{dt}+6\left\{\left(1-\frac{U}{3}\right)\mathbf{Q}-U\left(\mathbf{Q}\cdot\mathbf{Q}-\tfrac{1}{3}(\mathbf{Q}:\mathbf{Q})\delta\right)+U(\mathbf{Q}:\mathbf{Q})\mathbf{Q}\right\} \tag{3.1}$$
$$-\frac{U}{R}\left\{\nabla^2\mathbf{Q}+L_2\left(\nabla(\nabla\cdot\mathbf{Q})+[\nabla(\nabla\cdot\mathbf{Q})]^T-\frac{2}{3}\mathrm{tr}[\nabla(\nabla\cdot\mathbf{Q})]\delta\right)\right\}=0$$

Note that the equation is in dimensionless form and $\left(\tilde{\ }\right)$ has been removed for the sake of clarity. Equation (3.1) can be further written as:

$$\left(1-\tfrac{3}{2}\mathbf{Q}:\mathbf{Q}\right)^2\frac{\mathrm{d}\mathbf{Q}}{\mathrm{dt}}+\mathrm{F}^{\mathrm{h}}+\mathrm{F}^{\mathrm{e}}=0 \tag{3.2}$$

The above equation describes the dynamical evolution of the carbon fiber microstructure and F^{h}, F^{e} represent the homogeneous and elastic contributions to the free energy. As previously mentioned the short-range elasticity governs the isotropic-nematic transition and tends to keep the molecular order (S and P) equal to that of the equilibrium state in a local domain. The long-range order elasticity, on the other hand, tends to minimize the spatial gradients in the system. The dimensionless parameters of our model are $\mathrm{U}=\frac{3T^*}{T}$, known as the nematic potential, $R=\frac{H^2ckT^*}{2L_1}=\frac{H^2}{2\xi^2}$ (ratio of short-range order elasticity to long-range order elasticity), and $\widetilde{L_2}=\frac{L_2}{L_1}$ (measure of elastic anisotropy). Where T^* denotes the isotropic-nematic phase transition temperature, T is the temperature, H represents the fiber radii, L_1 and L_2 are the Landau coefficients, and $\xi=\sqrt{\frac{L_1}{ckT^*}}$ is the characteristic defect core length. The nematic potential U is the reciprocal of the dimensionless temperature and controls that equilibrium order parameter S_{eq} at the phase transition. The expression relating the equilibrium scalar order parameter to the nematic potential is given as [2]:

$$S_{eq}=\frac{1}{4}+\frac{3}{4}\sqrt{\left(1-\frac{8}{3\mathrm{U}}\right)} \tag{3.3}$$

Accordingly for our model the isotropic-nematic phase transition occurs at a value of U = 8/3 and the isotropic phase is stable below this value. For the range of $8/3\leq \mathrm{U}\leq 3$, there is biphasic equilibrium. The nematic phase is the only stable phase for values of $\mathrm{U} > 3$. For the computations in this work we use $2.7\leq \mathrm{U}\leq 6$. The parameter R is the ratio of the fiber radius to the internal length scale (ξ).It signifies the relative effects of the short-range order elasticity and the long-range elasticity. When $R \ll 1$, long-range energy dominates and tends to avoid spatial gradients thus leading to the selection of homogenous states. On the other hand, when $R \gg 1$, long-range energy is insignificant as compared to the short-range energy and defects proliferate, since spatial gradients are not as costly as the non-homogenous states. In the results presented here the values of R used are $0<R\leq 300$. The third dimensionless parameter is L_2, a measure of the elastic anisotropy. When $L_2 = 0$, all the elastic modulii are equal ($K_{11}=K_{22}= K_{33}$) and the system is elastically isotropic in the sense neither of the elastic modes of deformation (splay, twist, bend) is energetically favourable over the other modes. A non-zero value of L_2 in our model denotes that the splay elastic modulus of deformation is equal to the bend modulus of elastic deformation ($K_{11}= K_{33}$). Moreover, the thermodynamic restrictions [3] imply that the elastic constants satisfy the following condition:

$$L_2 > -\frac{3}{5} \tag{3.4}$$

In addition, since for discotic nematic liquid crystals it is well known that $K_{22}>K_{11}$, and $K_{33}>K_{11}$. We get the following limits for L_2:

$$-\frac{3}{5} < L_2 \leq 0 \tag{3.5}$$

We have used $L_2=-0.5$ for the computations in this chapter. The governing equation (3.1) is solved numerically in a circle of unit radius. For the numerical computation the quenching phenomenon is used i.e. when time $t = 0$, the system is in isotropic state with $\mathbf{Q}\approx 0$ and $U=U_{iso}$. This implies that the system is above the isotropic-nematic transition temperature and isotropic phase is the only stable phase. The initial condition can be written as:

$$t=0,\ \mathbf{Q}_{\text{ini}} = S_{ini}\left(\mathbf{n}_{\text{ini}}\mathbf{n}_{\text{ini}} - \frac{1}{3}\delta\right) + \frac{1}{3}P_{ini}\left(\mathbf{m}_{\text{ini}}\mathbf{m}_{\text{ini}} - \mathbf{l}_{\text{ini}}\mathbf{l}_{\text{ini}}\right)$$

$$\mathbf{n}_{\text{ini}} = \begin{pmatrix}\cos(\zeta)\\ \sin(\zeta)\\ 0\end{pmatrix} \quad \mathbf{m}_{\text{ini}} = \begin{pmatrix}\cos\left(\frac{\pi}{2}+\zeta\right)\\ \sin\left(\frac{\pi}{2}+\zeta\right)\\ 0\end{pmatrix} \quad \mathbf{l}_{\text{ini}} = \begin{pmatrix}0\\ 0\\ 1\end{pmatrix} \tag{3.6 a, b}$$

where S_{ini} and P_{ini} are the initial uniaxial and biaxial order parameters generated randomly and $S_{ini} \approx 0$, $P_{ini} \approx 0$. The initial local orientation of the system is given by generating a set of orthogonal unit vectors $\mathbf{n}_{\mathrm{ini}}$, $\mathbf{m}_{\mathrm{ini}}$, $\mathbf{l}_{\mathrm{ini}}$ at each point on the mesh. A visualization of the initial condition used for the solution is given in figure 32.

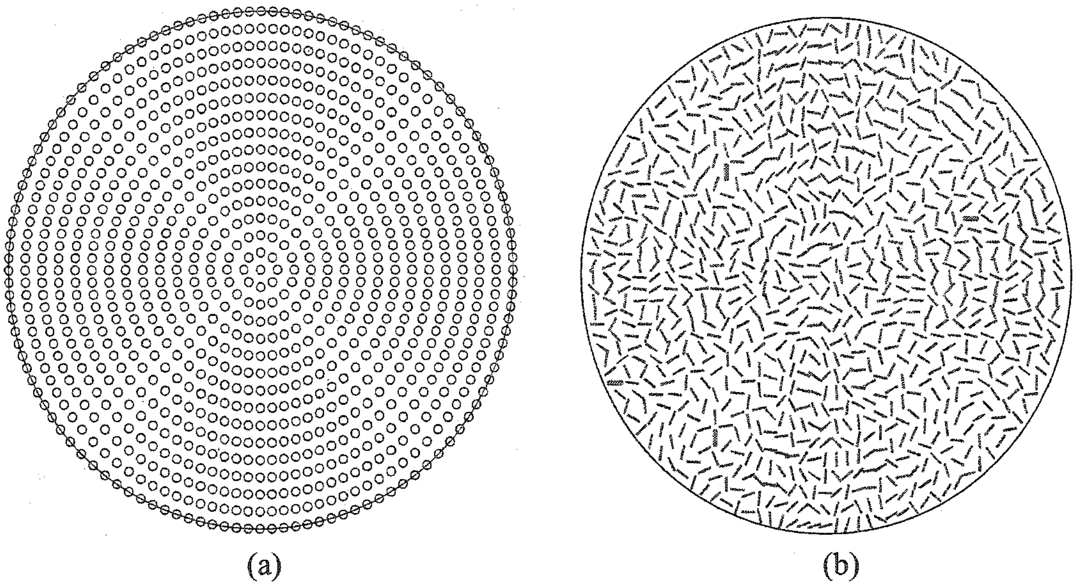

(a) (b)

Figure 32: Visualization of the initial condition used for the numerical computations. In (a) the initial condition is visualized according to the technique given in Chapter 2. For a very low order parameter the ellipsoids become circles. (b) represents the same initial condition in terms of molecular orientation (orientation of the disc-like molecules). Note that since we are solving for only the planar components of $\mathbf{Q}$, the orientation of the molecules is in plane only.

For t > 0 (t = ε i.e. time just after 0) we decrease the temperature (increase the nematic potential) of our system to a value U > 8/3 in which the nematic phase is stable. In other words we freeze the initial orientation of our system and let it evolve as per the parametric conditions specified. We also apply the Dirichlet boundary condition on the boundary of the circle. We specify the equilibrium scalar order parameter at the boundary given by the equation (3.3) as well as the molecular orientation at the boundary. For this work a strong homeotropic anchoring boundary condition has been used for all the cases. Moreover, this leads to the simplifying assumption, that due to the strong anchoring boundary condition, the director orientation is always planar. This assumption reduces our tensor parameter to the following form:

$$\mathbf{Q} = \begin{pmatrix} \mathbf{Q}_{xx} & \mathbf{Q}_{xy} & 0 \\ \mathbf{Q}_{xy} & \mathbf{Q}_{yy} & 0 \\ 0 & 0 & \mathbf{Q}_{zz}\left(=-\mathbf{Q}_{xx}-\mathbf{Q}_{yy}\right) \end{pmatrix} \tag{3.7}$$

The boundary condition used for numerical computation of the governing equation can be written as follows:

$$t=\varepsilon,\ \mathbf{Q}_{\text{ini}} = S_{eq}\left(\mathbf{n}_{\text{bc}}\mathbf{n}_{\text{bc}} - \frac{1}{3}\delta\right)$$

$$\mathbf{n}_{\text{bc}} = \begin{pmatrix} \cos(\theta) \\ \sin(\theta) \\ 0 \end{pmatrix} \qquad \mathbf{m}_{\text{bc}} = \begin{pmatrix} \cos\left(\frac{\pi}{2}+\theta\right) \\ \sin\left(\frac{\pi}{2}+\theta\right) \\ 0 \end{pmatrix} \qquad \mathbf{l}_{\text{bc}} = \begin{pmatrix} 0 \\ 0 \\ 1 \end{pmatrix} \tag{3.8 a, b}$$

where θ is always homeotropic to the boundary at all the points on the grid.

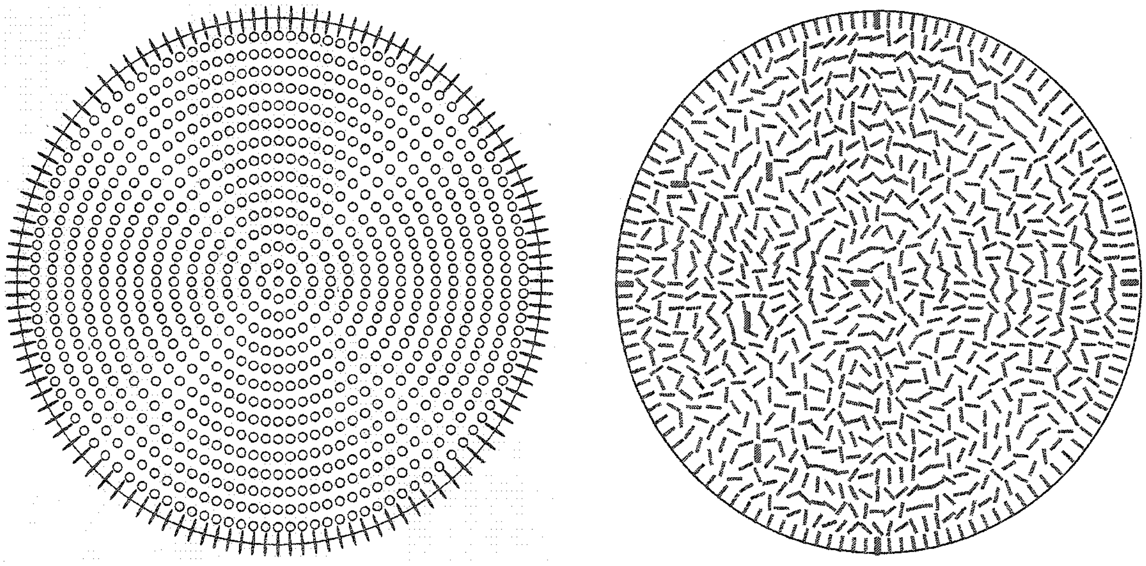
(a) (b)

Figure 33: Visualization of the boundary condition used for the numerical computations. In (a) the initial condition is visualized according to the technique given in Chapter 2. The narrow sharp ellipsoids on the boundary indicate a high scalar order parameter as well as the homeotropic boundary orientation is clearly visible. (b) represents the same boundary condition in terms of molecular orientation (orientation of the disc-like molecules).

The molecular orientation is perpendicular to the surface whereas the director orientation is tangential at the surface (because in DNLCs a bend director trajectory gives rise to splay configuration and splay director trajectory gives rise to a bend configuration). The visualization for the boundary condition in terms of ellipsoids and molecular orientation is presented in figure 33.

3.3 Results and Discussion

3.3.1 Typical Two-Dimensional Textures

The two characteristic textures obtained by numerical solution to the governing equation together with its auxiliary conditions are Planar Radial (PR) and Planar Polar (PP) textures. A molecular profile of the typical PR and PP textures obtained is shown in figure 34.

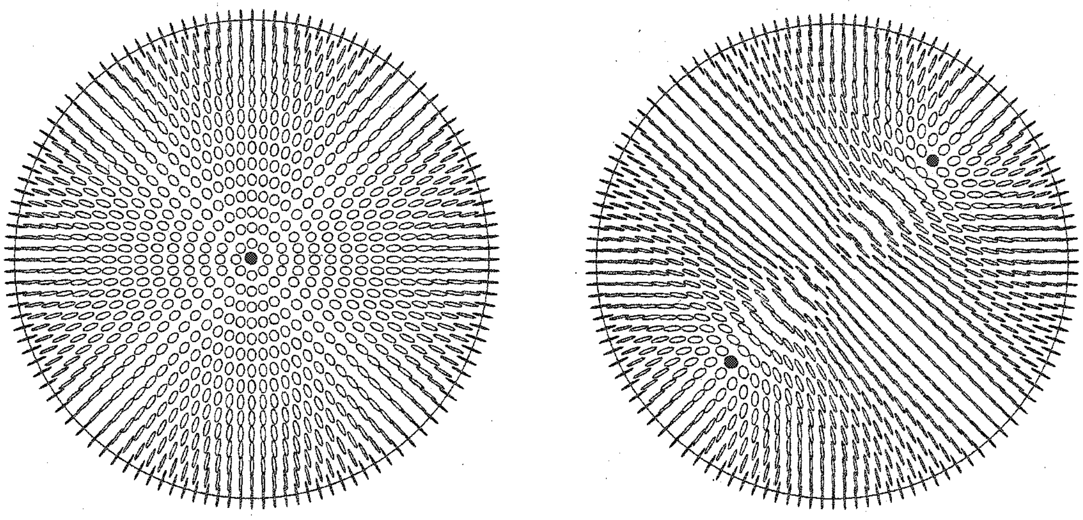

(PR) (PP)

Figure 34: The two characteristic textures obtained as solutions to the governing equation. The planar radial (PR) with is characteristic disclination of strength +1 is shown on the left and planar polar (PP) texture with two disclinations of strength +1/2 is shown on the right. The parametric conditions used are (i) for PR, U = 6.0, L_2 = -0.5, and $\frac{H}{\xi} = 2.25$ (ii) for PP, U = 6.0, L_2 = -0.5, $\frac{H}{\xi} = 5.0$

The molecules are aligned in the radial direction (perpendicular) at the boundary and continue to be radially aligned as we move towards the center of the fiber. A disclination of strength s = +1 forms at the center of the fiber cross-section. The planar radial (PR) configuration is rotationally symmetric. The only deformation mode that exists in the PR texture is bend (K_{33}), although the molecular trajectories in the visualization scheme display splay. This is due to the fact that for discotic nematics the major dimension of the molecules is perpendicular to the director n. In contrast the planar polar (PP) texture is the symmetry-breaking configuration solution [4] to the governing equation (3.1). In addition the PP texture configuration contains two defects of strength $s = +1/2$ collinear with the fiber axis as shown in figure 34. A texture obtained by the rotation of the PP texture through an angle φ about the axis of the cylinder has the same free energy and is also a solution to our governing equation. Therefore all textures obtained by rotation are equivalent. The PP texture has bend (K_{33}) as well as splay (K_{11}) modes of elastic deformation. In addition, the PP texture has a perfectly-aligned region in between the two defects close to the center of the fiber.

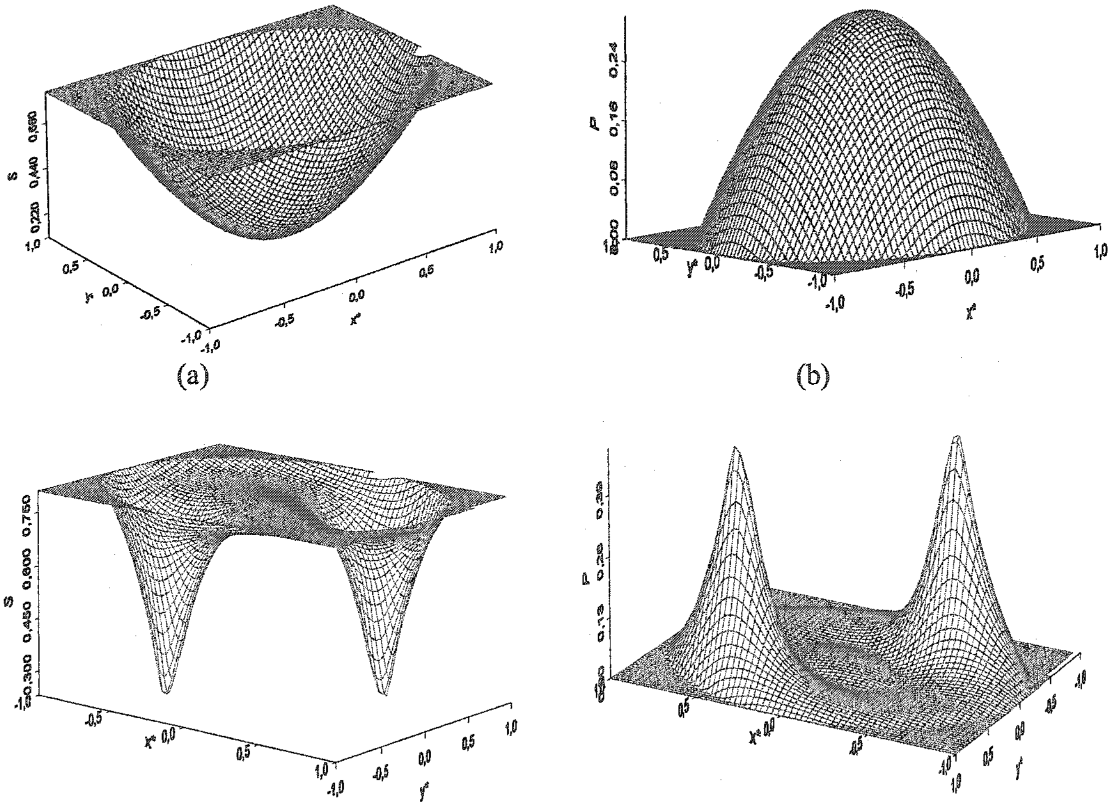

(a) (b)

(c) (d)

Figure 35: Surface plots showing the uniaxial scalar order parameter S and biaxial order parameter P. (a) & (b) represent S and P for a Planar Radial (PR) texture. (c) & (d) represent S and P for a Planar Polar texture (PP). The parametric conditions are the same as used in figure 34.

The scalar order parameter deviates considerably from its bulk value near the defects in both the characteristic textures namely, PR and PP [5]. In figure 35 we present a surface plot of the variation of the uniaxial scalar order and biaxial scalar parameters across the fiber cross-section. It is clearly visible from the surface plots of the PP and PR textures that the troughs in the surface plots (a) & (c) represent the center of the defect and the value of the uniaxial scalar order parameter S is the lowest at this point. On the contrary the peaks in plots (b) & (d) also represents the center of a defect and the value of the biaxial order parameter P is the highest at the core of the defect. We have also calculated a phase diagram for the two stable characteristic textures (PR and PP) that predicts which of the solutions is stable for a given temperature and given capillary size. The phase diagram is shown in figure 36.

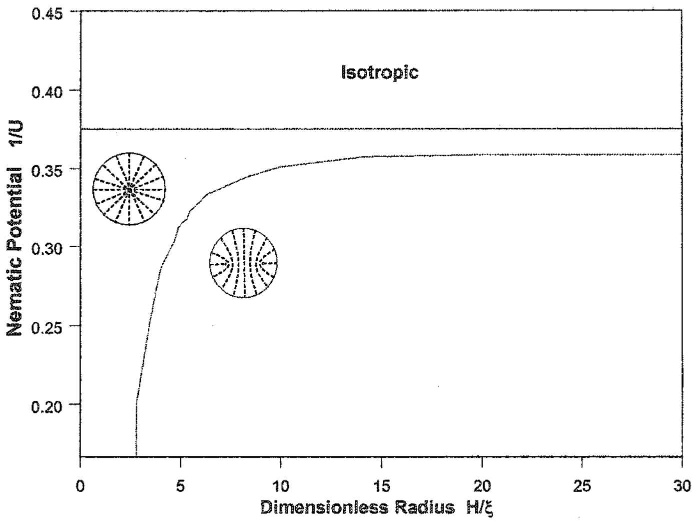

Figure 36: Phase diagram which predicts the type of solution for a given dimensionless temperature and dimensionless radius. The two stable characteristic textures observed are the planar radial (PR) and the planar polar (PP).

The solid line identifies the texture transition line. The phase diagram predicts that carbon fibers of smaller cross-section favor the PR texture whereas fibers of larger cross-section prefer the PP texture. It also predicts that the region of stability for the PR texture increases with increase in temperature (decrease in the nematic potential) until U=3.0, after which the PR texture is stable for all fiber radii. Therefore if the carbon fibers are spun at higher temperature then they should exhibit a planar radial (PR) texture irrespective of the fiber radius. In contrast if they are spun at a lower temperature they should exhibit planar polar (PP) texture as well as planar radial (PR) texture depending upon the radius of the fiber. This is confirmed by experimentalists [6].The phase transition from planar radial (PR) to planar polar at large U is controlled by the long-range elastic effects, i.e. the fiber size is the controlling parameter whereas for large fiber size, the short-range elastic effects are responsible for the phase transition. Thus for higher fiber radii, the temperature is the controlling factor for phase transition. A comprehensive analysis of our problem should also involve the study of the dynamical phenomena in the evolution of the two characteristic textures, namely PR and PP. This analysis is done in the following section.

3.3.2 Dynamical Structure Evolution of Planar Radial (PR) and Planar Polar (PP)

In this section we present the transient evolution of the two characteristic textures, namely planar radial (PR) and planar polar (PP). We also present the time evolution of the different energies of the system (short-range order elasticity, and long-range order elasticity) for the two textures. The time evolution of the PR texture is shown in figure 37. It is clearly apparent the order diffuses from the boundary towards the center of the fiber similar to that seen in various diffusion processes. Another characteristic of the transient process is the different time scales that are clearly visible in figure 37. The external time scale in this study is given by $\tau_e = \frac{\eta H^2}{L_1}$ and as such will increase with increase in the value of R. For the parametric conditions used in figure 37, the external time scale τ_e is approximately of the same order of magnitude as the internal time scale τ_i. Although the system reaches the steady molecular orientation of a PR texture before the scalar order parameter S reaches its steady state value, the time scales are of the same order of magnitude as shown in the time evolution of the long-range energy and short-range energy in figure 38. Moreover for the value of the parameter $\frac{H}{\xi} = 2.45$, U=6.0, the long-range energy and the short-range energy are equally costly and the rotationally symmetric PR texture optimizes both the free energies to give the minimum total energy.

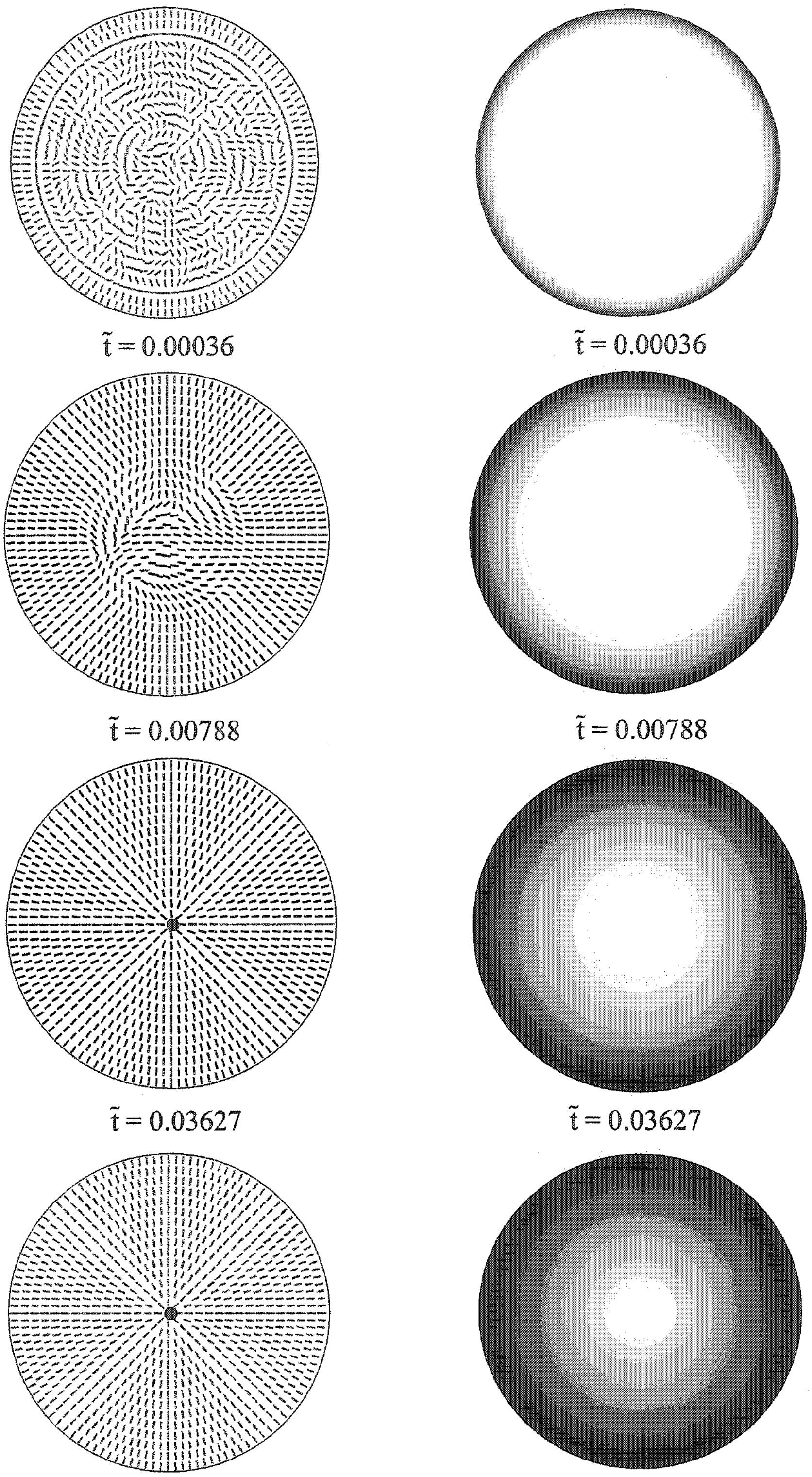

$\tilde{t} = 0.00036$ $\tilde{t} = 0.00036$

$\tilde{t} = 0.00788$ $\tilde{t} = 0.00788$

$\tilde{t} = 0.03627$ $\tilde{t} = 0.03627$

$\tilde{t} = 0.24412$ $\tilde{t} = 0.24412$

Figure 37: Transient evolution of the PR texture. The parametric conditions used here are U=6.0, $\frac{H}{\xi} = 2.45$, L_2 = -0.5. Left column: Orientation profile. Right column: Scalar order parameter (*S*).

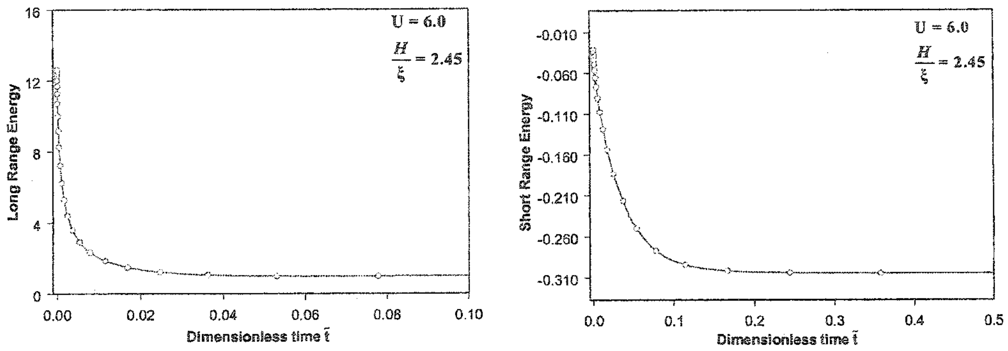

Figure 38: Time evolution of the long-range energy and short-range energy for U=6.0, $\frac{H}{\xi} = 2.45$, L_2 = -0.5. The difference in two time scales is clearly visible. The long-range energy reaches a steady state at $\tilde{t} \approx 0.036$ whereas the short-range energy reaches steady state at $\tilde{t} \approx 0.24$.

Now we move to the transient evolution of planar polar texture. We present a slightly different phase diagram than that given by Davis [7] in figure 39 to clearly explain the transient evolution of the planar polar texture.

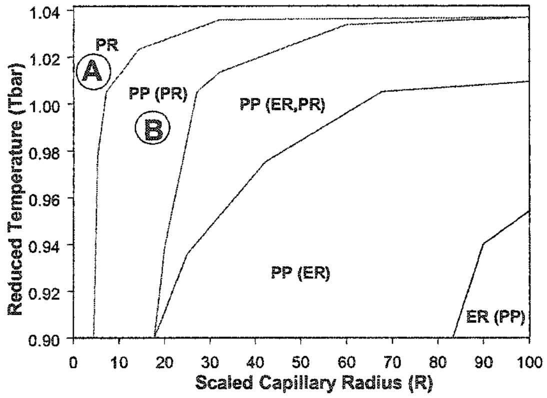

Figure 39: Phase diagram showing various textures that are stable for various parametric conditions of temperature and capillary radius. The textures are PR (Planar Radial), PP (Planar Polar), and ER (Escape Radial). The textures given in the parentheses are textures that are stable but with higher energy. Adapted from [7].

Before we actually look at the transient evolution of the PP texture a brief description of the phase diagram is necessary. The various acronyms are the same as those used before except ER, which represents the Escaped Radial (ER) texture. In the ER texture the director escapes in the fibre axis direction (z direction in a cylindrical coordinate system) as we move from the boundary to the center of the fibre axis as explained in Chapter 2. The contrasting features of this diagram (figure 39) is that in addition to the most stable textures it also lists other stable textures of higher energy that are shown in the parenthesis. Since dynamical simulations are performed in this study we always obtain textures with the lowest energy. Thus, we obtain only planar radial for region A and planar polar for region B in our simulations. Moreover, we never obtain the escape radial texture because the form of the tensor order parameter that we employ restricts the director in the fibre cross-section plane (r-θ plane in the cylindrical coordinate system).The transient evolution of the planar polar texture has three pathways depending on the parametric values used. The first path involves the formation of the intermediate PR texture and then the classical defect split of a defect of strength +1 into two defects of strength $+\frac{1}{2}$.

$$s=+1 \rightleftharpoons s=+\tfrac{1}{2}+s=+\tfrac{1}{2} \tag{3.9}$$

The system takes this path when the parametric values used lie in the region of the phase diagram where the PR texture is metastable. The first path that leads to the PR texture is shown in figure 40. It is clearly visible in the figure that the system attains a planar radial texture with a defect of strength of +1 at the center and then it transforms into two defects of strength $+\frac{1}{2}$. This path for the evolution of the PP texture is essentially a three-stage process. The early stage involves the formation of the intermediate PR texture followed by the intermediate stage consisting of a topological transformation of the +1 defect into two defects of strength $+\frac{1}{2}$. The final step is the relocation of the two defects to their final equilibrium position. This process can be clearly explained by looking at the transient evolution of the short-range order elasticity and long-range order elasticity of a given PR texture for specified parametric conditions. In figure 41 we show the long-range order elasticity and short-range order elasticity for different values of $\frac{H}{\xi}$ that follow the defect splitting path for planar polar texture formation. We observe that there are three stages in the evolution of the long-range elasticity and short-range elasticity. The long-range elasticity in the first stage of evolution reaches a minimum value. This is followed by increase in the long-range elasticity until it reaches an intermediate plateau value.

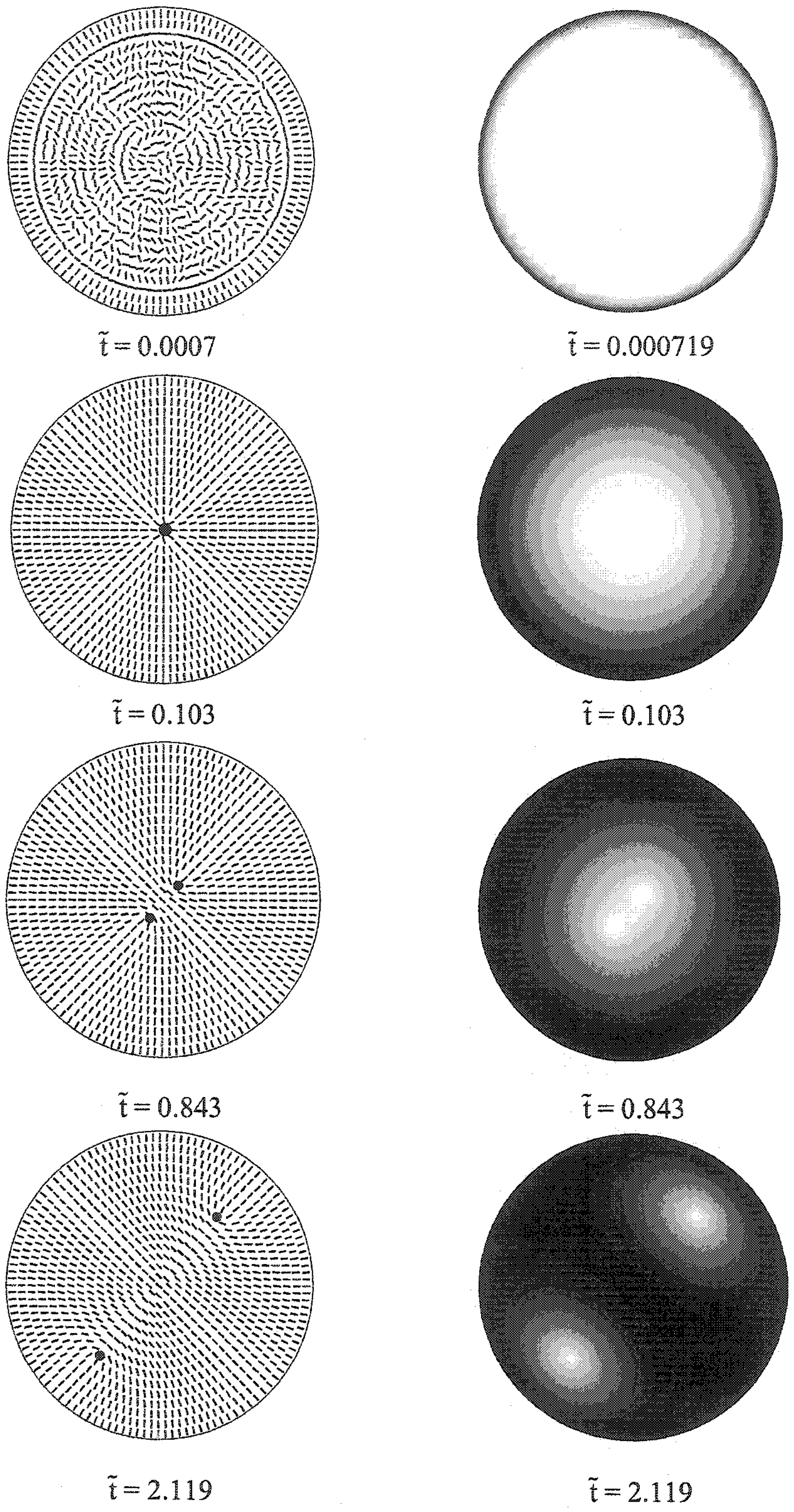

$\tilde{t}=0.0007$ $\tilde{t}=0.000719$

$\tilde{t}=0.103$ $\tilde{t}=0.103$

$\tilde{t}=0.843$ $\tilde{t}=0.843$

$\tilde{t}=2.119$ $\tilde{t}=2.119$

Figure 40: Transient evolution of the PP texture. The intermediate PR texture is clearly visible before the texture transforms into PP through defect splitting. The parametric conditions used here are U=6.0, $\frac{H}{\xi}=31.6$, L2 = -0.5. Left column: Orientation profile (**n**). Right column: Scalar order parameter (*S*).

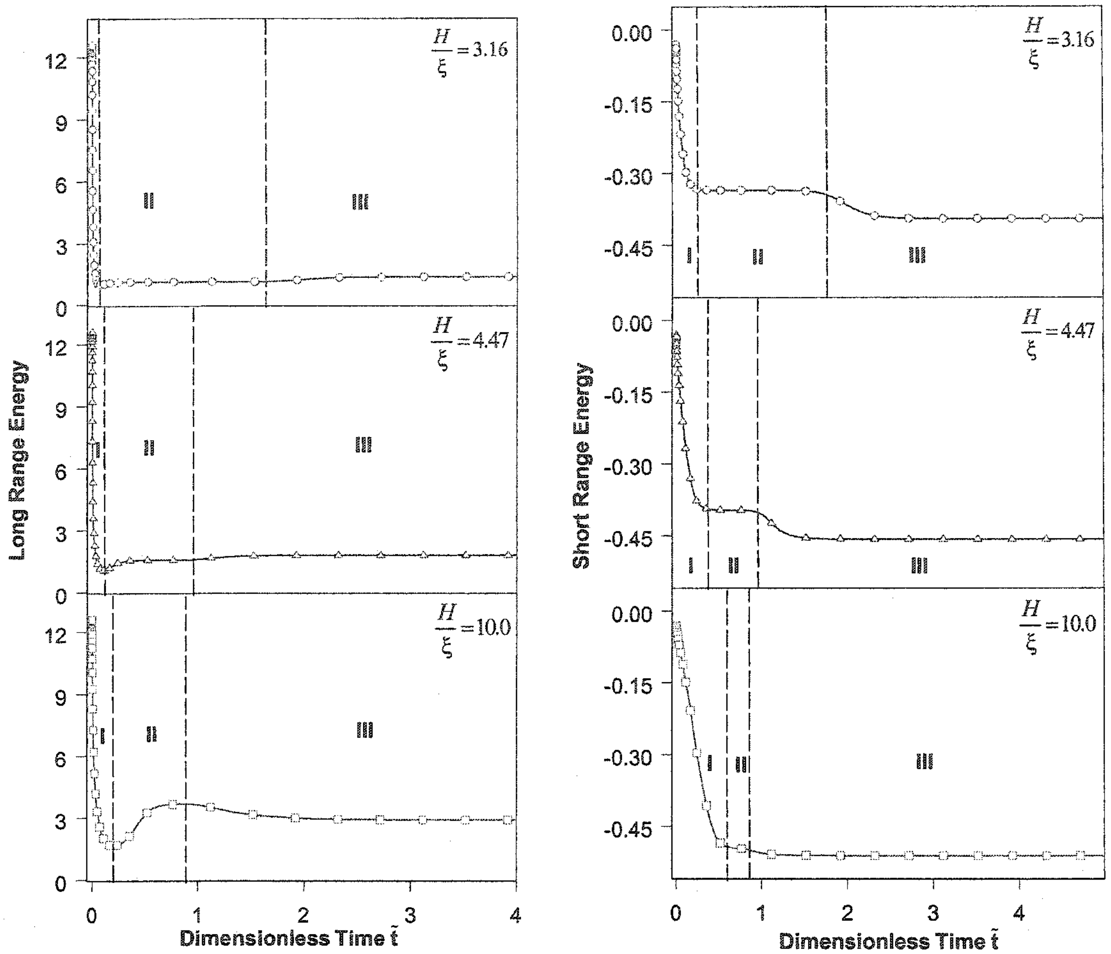

Figure 41: Long-range and short-range energy plots for different values of dimensionless fibre radii. The evolution of long-range energy and short-range energy follows three different stages. The dashed lines indicate various stages since they are not clearly visible in some cases.

Finally there is further increase/decrease in the long-range elasticity signifying the beginning of the late stage. In the early stage (i.e. at the bottom of the trough-like structure in the plot of long-range elasticity) the microstructure is planar radial (PR). In the intermediate stage the microstructure is still planar radial up until the later stages of the intermediate steady state in stage two when the +1 defect splits into two $+\frac{1}{2}$ defects. In the late stage the main phenomenon involved is the relocation of two defects at their final equilibrium position. The dashed vertical line separates the early, intermediate, and later stages since in some cases it is not clearly apparent by looking at the plot. In the time evolution of short-range energy an early stage with an exponential decrease is followed by an intermediate state with a plateau followed by a step like decrease before reaching the final steady state. The step like decrease following the intermediate stage signals the beginning of the late stage. It is interesting to note that the onset of the late stage for both short-range energy and long-range energy evolution begins at almost the same time. The splitting of the +1 defect in a PR texture does not cause a change in the short-range energy, and therefore at the end of intermediate stage in the short-range the texture is planar polar but the two $+\frac{1}{2}$ defects are very close to each other. In other words the width of existence of the first (intermediate) steady state (stage two) in the short-range energy plot is proportional to the extent that the PR texture is metastable before it transforms to the PP texture. Thus from the plots we observe that for the given value of U=6.0, the PR texture ceases to be metastable for $\frac{H}{\xi} > 10.0$. For fibres of larger thickness the evolution of PP texture is not through the defect splitting process. With these results we can present a coherent picture for the whole PP texture evolution process. First the system minimizes the elastic energy by forming a planar radial texture but the relative magnitude of the short-range elasticity is higher as compared to parametric values for which the PR texture is completely stable which for the current case of U=6.0 is $\frac{H}{\xi} \leq 2.82$. This implies a stronger force promoting uniaxiality and therefore decreases the defect core radius and results in a higher energy of deformation as given by the energy equation (3.10) for a defect of strength +1 [8].

$$W = W_c + \pi K \ln\left(\frac{H}{r_c}\right) \tag{3.10}$$

where W_c is the core energy and r_c is the core radius. This is the reason for the increase in long-range energy after reaching a minimum value because the short-range energy is still decreasing when the long-range starts to increase after reaching its minima. Therefore the system can reduce the free energy by shrinking the defect core radius only up to a limit and beyond that the only way is by splitting the +1 defect into two $+\frac{1}{2}$ defects because the energy scales as square of the defect strength. After the defect split there is a sudden drop in short-range free energy due to relocation of the two $+\frac{1}{2}$ defects after the split. Next we will look at the second method of the formation of the planar polar texture.

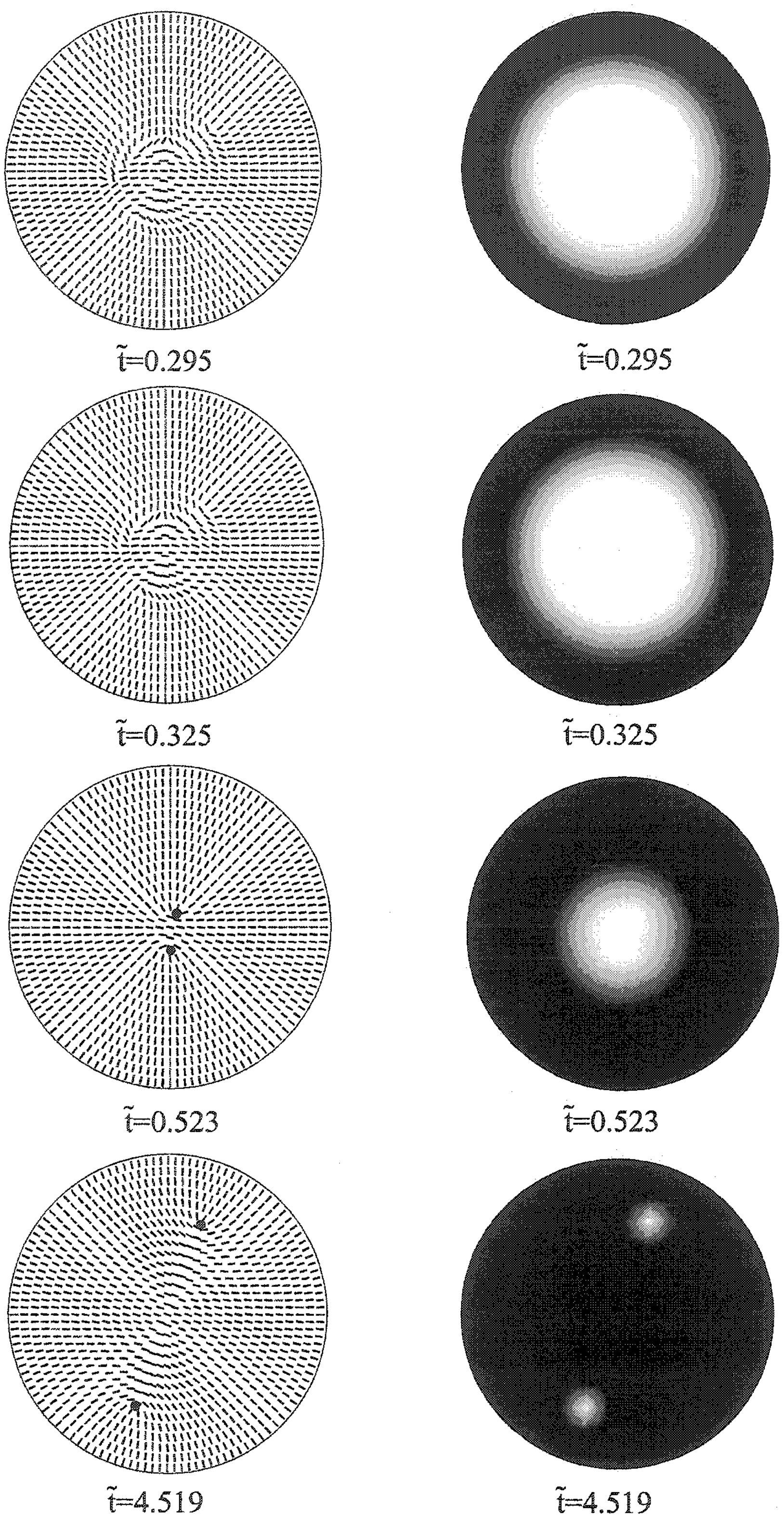

$\tilde{t}=0.295$ $\tilde{t}=0.295$

$\tilde{t}=0.325$ $\tilde{t}=0.325$

$\tilde{t}=0.523$ $\tilde{t}=0.523$

$\tilde{t}=4.519$ $\tilde{t}=4.519$

Figure 42: Second pathway for planar polar texture evolution without the formation and splitting of defect of strength +1. The parametric conditions used are U=6.0, $\frac{H}{\xi}=14.15$, L_2 = -0.5. Left column: Orientation profile (**n**). Right column: Scalar order parameter (S).

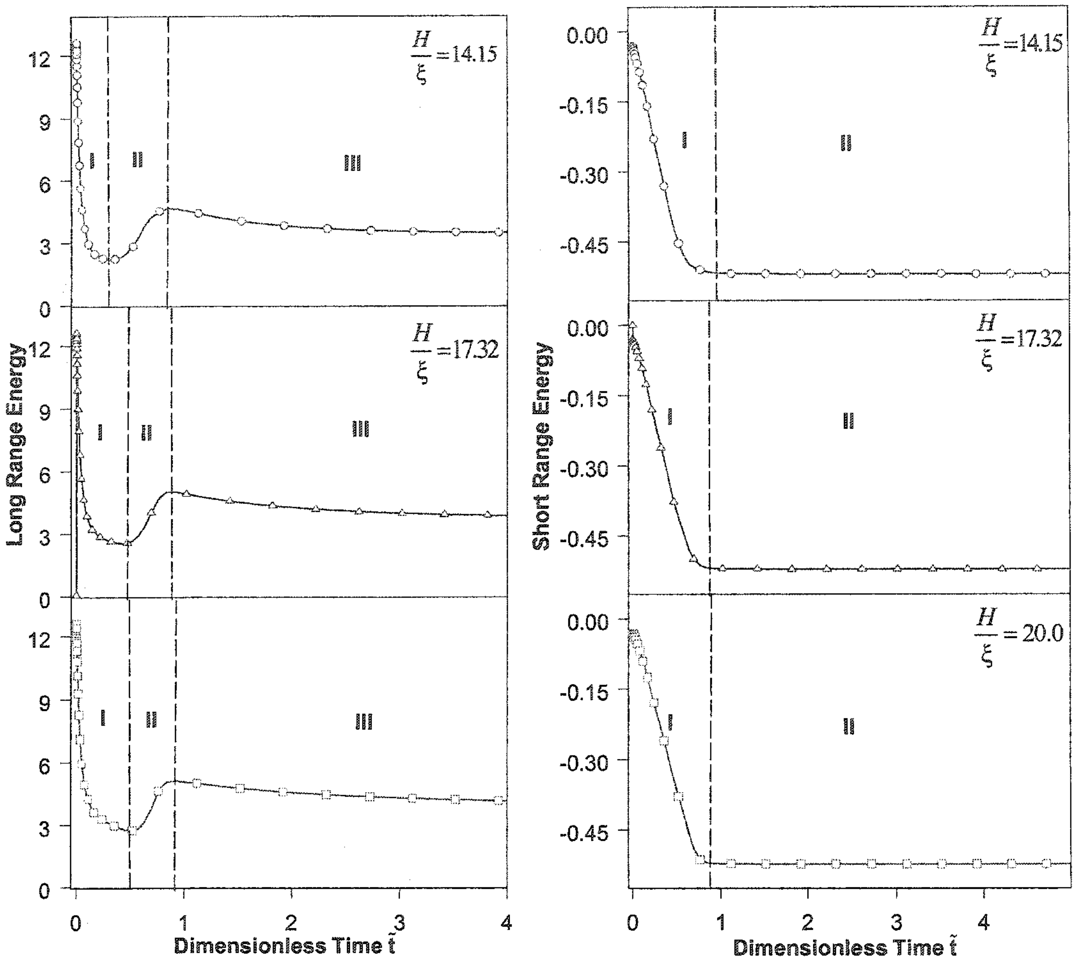

Figure 43: Long-range energy and short-range energy plots for different dimensionless fibre radii. The long-range energy profile shows behaviour similar as before but short-range energy does not show a step function like drop but reaches steady state without any intermediate steady states in between.

The second pathway for the evolution of the planar texture is shown in figure 42. For this pathway the long-range energy shows behaviour similar to the first case. The minimum of the long-range energy (i.e. the lowest point of the trough like shape in the plot) no longer corresponds to a planar radial (PR) orientation configuration but has a texture that we will refer to as isotropic core (IC), as shown in the top most texture in figure 42 at $\tilde{t}$=0.2953. The characteristic of the isotropic core texture is that there is a radial rim surrounding an isotropic core. The scalar order parameter S in the core region is non zero but is very small for the parameters used in figure 42. Once the long-range energy has reached its minimum value the scalar order parameter is still diffusing inwards reducing the region of nucleation of the two $+\frac{1}{2}$ defects and thereby leading to an increase in the long-range elasticity. In the beginning the diffusion of scalar order parameter is radially symmetric until the long-range reaches its minimum value at the bottom of the trough.

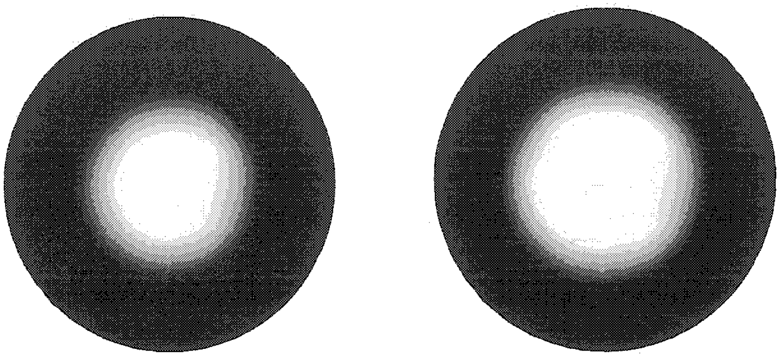

(a) (b)

Figure 44: Selective scalar order diffusion during the formation of planar polar texture for two different values of $\frac{H}{\xi}$. For (a) $\frac{H}{\xi}=14.15$ and (b) $\frac{H}{\xi}=17.32$. The value of U=6.0 and L_2 = -0.5 for both the cases.

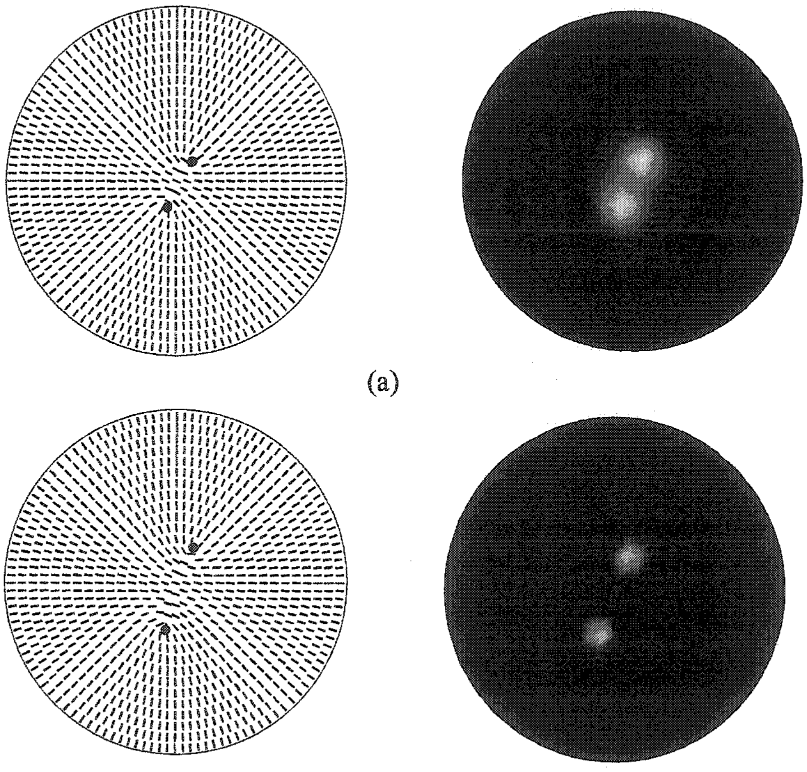

(a)

(b)

Figure 45: The above figure shows that the distance of the nucleation of the two $+\frac{1}{2}$ defects increases with increasing fibre radius before they relocate to their equilibrium postion. The value of $\frac{H}{\xi}$ is 14.15 for (a) and 20.0 for (b). The value of U is 6.0 and L_2 = -0.5 for both the cases.

After that this symmetry is broken and there is selective diffusion of the short-range elasticity. This process of selective diffusion is shown clearly in figure 44. Another interesting phenomenon to note is that the time at which the long-range energy reaches its local maxima for the transition into the late stage coincides with the short-range energy reaching its steady state value. Finally the two $+\frac{1}{2}$ defects repel each other to an equilibrium position with a small decrease in the long-range energy. The distance between the nucleation of the two $+\frac{1}{2}$ defects in the polar planar texture before they move apart increases with increasing fibre radius as shown in figure 45. Furthermore as we move towards higher fiber radii $(\frac{H}{\xi} \approx 30)$ for the same value of U=6.0 the number of defects that form before the steady state polar texture is observed increases. This is clearly depicted in figure 46 showing the transient evolution of the planar polar texture at U=6.0 and $\frac{H}{\xi} = 31.6$. Initially there are four defects that are formed, followed by defect-defect interaction leading to the annihilation of two defects and eventually leaving us with two $+\frac{1}{2}$ defects. The defect annihilation reaction can be given as:

$$s = +\frac{1}{2} \; + s = -\frac{1}{2} \rightleftharpoons 0 \tag{3.11}$$

This defect-defect interaction is due to the fact that defects of opposite signs attract each other and the attractive force per unit length between two wedge disclinations of $\frac{1}{2}$ strength is given by [9]:

$$\mathscr{F}_{12} = \frac{\pi K}{2\mathrm{d}} \tag{3.12}$$

Where K represents the elastic constant in the case of one constant approximation and d represents the distance between the two disclinations. In addition, the fiber size is not too large to render long-range elastic effects (like the defect interaction) negligible as the attractive force reduces with the increase in distance between the defects.

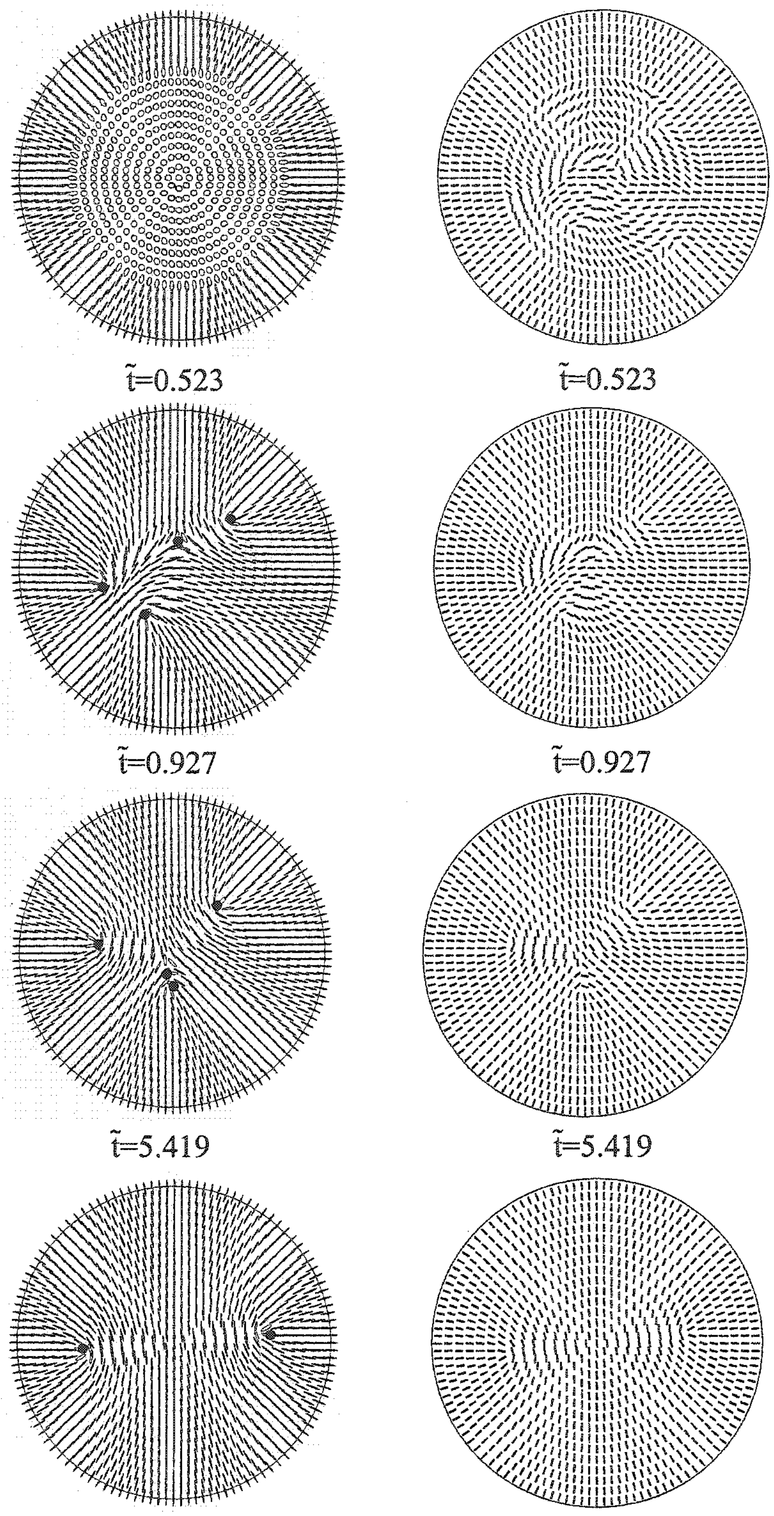

$\tilde{t}$=0.523 $\tilde{t}$=0.523

$\tilde{t}$=0.927 $\tilde{t}$=0.927

$\tilde{t}$=5.419 $\tilde{t}$=5.419

$\tilde{t}$=50.019 $\tilde{t}$=50.019

Figure 46: The formation of the PP texture through initial coarsening of multiple defects and consequent annihilation of two defects. The parametric values used in the above case are U=6.0, $\frac{H}{\xi} = 31.6$ and L_2 = -0.5. The annihilation of two $\frac{1}{2}$ defects is clearly visible at t=5.419. The figures on the left show ellipsoid representation and on the right show director representation.

Figure 47 shows the long-range and short-range energy evolution for the above methodology of the formation of planar polar (PP) texture through the texture coarsening process. The minimum of the long-range energy corresponds to the topmost set of figures in figure 47 and can be characterized by an ordered boundary layer and isotropic central region. In addition, the director profile at this stage shows apparent coarsening of multiple defects at a future time. As the scalar order parameter diffuses in, some of the apparent defects in director orientation never coarsen into defects but the molecules become oriented with the diffusion of the scalar order parameter. Eventually only four defects coarsen as the scalar order parameter diffuses inwards leading to an increase in the long-range energy. The local maximum following the minimum in the long-range energy is characterized by four $\frac{1}{2}$ defects (3 defects of $+\frac{1}{2}$ and one defect of $-\frac{1}{2}$). This point corresponds to the second set of figures in figure 46 at t=0.93. As pointed out previously, the time at which the long-range energy reaches it local maximum is the same time at which the short-range energy reaches its minimum steady state value.

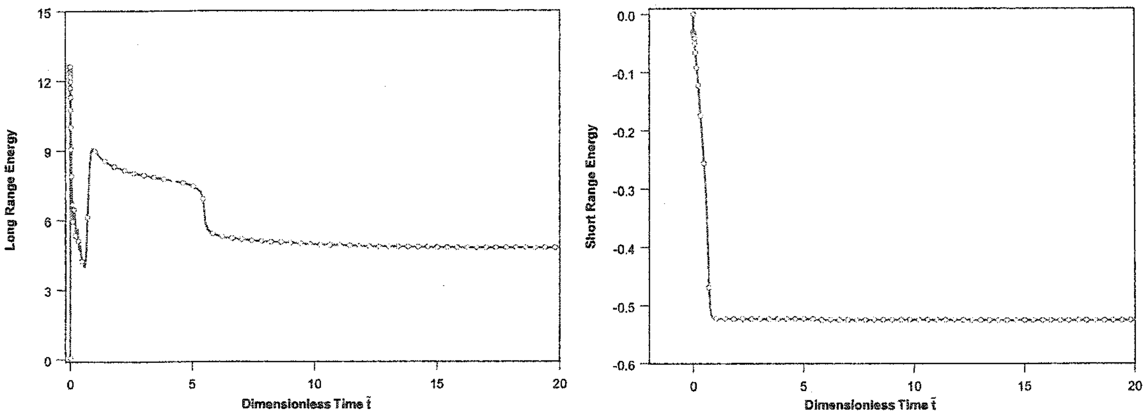

Figure 47: Time evolution of long and short-range energy for the formation of planar polar texture by defect annihilation process. The parametric values used in the above case are U=6.0, $\frac{H}{\xi} = 31.6$ and L_2 = -0.5. A sudden reduction is visible in the long-range energy at $\tilde{t}$=5.61 where the two $\frac{1}{2}$ defects combine to annihilate each other and leave only two $+\frac{1}{2}$ defects.

After this point the reduction in energy of the system is solely due to reduction in the long-range energy. The local maximum in the long-range energy is followed by a steady decay in the long-range energy indicating the movement of the two $\frac{1}{2}$ defects of opposite signs towards each other. Finally there is a sudden reduction in the long-range energy, which is an indication of the annihilation of two half defects followed by a small steady decrease in the long-range energy denoting the reorientation and relocation of the two remaining $+\frac{1}{2}$ defects. Moreover the long-range energy reaches the steady state later than the short-range energy because the long-range order time scale is much larger than the short-range order time scale for the fibre radius involved. In summary the formation of the planar polar texture in the present case is by both by defect splitting and defect annihilation by combination of two defects of $\frac{1}{2}$ strength but of opposite sign. In the next section we will take a detailed look at the defect core structure for the defect of strength +1.

3.3.3 Defect Core Structure of the +1 Defect In Planar Radial Texture

In this section we will begin with the defect core structure of the PR and PP texture and move on to focusing in detail on the +1 defect of the planar radial texture. Figure 48 depicts the core of PR and PP texture in terms of eigenvalue plots across the fibre diameter of a planar radial texture and across the line joining the two defects of a planar polar texture.

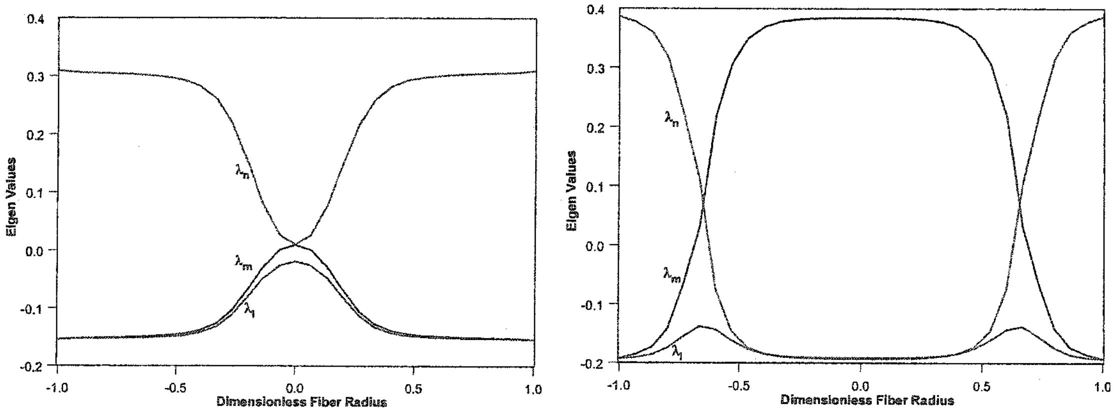

Figure 48: The variation of three eigen values of the tensor **Q** across the fibre diameter. The figure on the left is for PR texture (+1 defect) with U=2.90, $\frac{H}{\xi} = 24.5$. The figure on the right is for PP texture exhibiting the eigen value variation across the line joining the two $(+\frac{1}{2})$ defects. The value for U= 3.30 and $\frac{H}{\xi} = 17.3$ for PP texture.

The eigenvalues are defined as follows:

$$\begin{aligned} \lambda_n &= 2/3S \\ \lambda_m &= (P-S)/3 \\ \lambda_l &= -(P+S)/3 \end{aligned} \qquad (3.13a, b, c)$$

Note that $\lambda_n+\lambda_m+\lambda_l = 0$ and hence only two eigenvalues are independent. We observe that the tensor order parameter **Q** is uniaxial far from the defect and as we move closer to the defect it becomes increasingly biaxial and finally becomes uniaxial again at the centre of the defect [10, 11]. We also observe that the value of the biaxial scalar order parameter $P = 3S$ at the centre of the defect. This is true for both defects of strength +1 and $+\frac{1}{2}$. It is apparent from the eigenvalue plots shown in figure 48 that at the center of the defects the two largest eigenvalues (λ_n and λ_m) become equal and the only distinct eigenvalue is λ_l, thus making tensor order parameter uniaxial. From here on we will focus on the defect core of +1 defect. We will start with an explanation of the scalar order parameter *S-P* triangle [12] that we will use to elucidate the defect core texture. The *S-P* triangle can represent various order parameter fields since the eigenvalues are directly related to the two scalar order parameter *S* and *P*. The *S-P* is shown in fig.49.

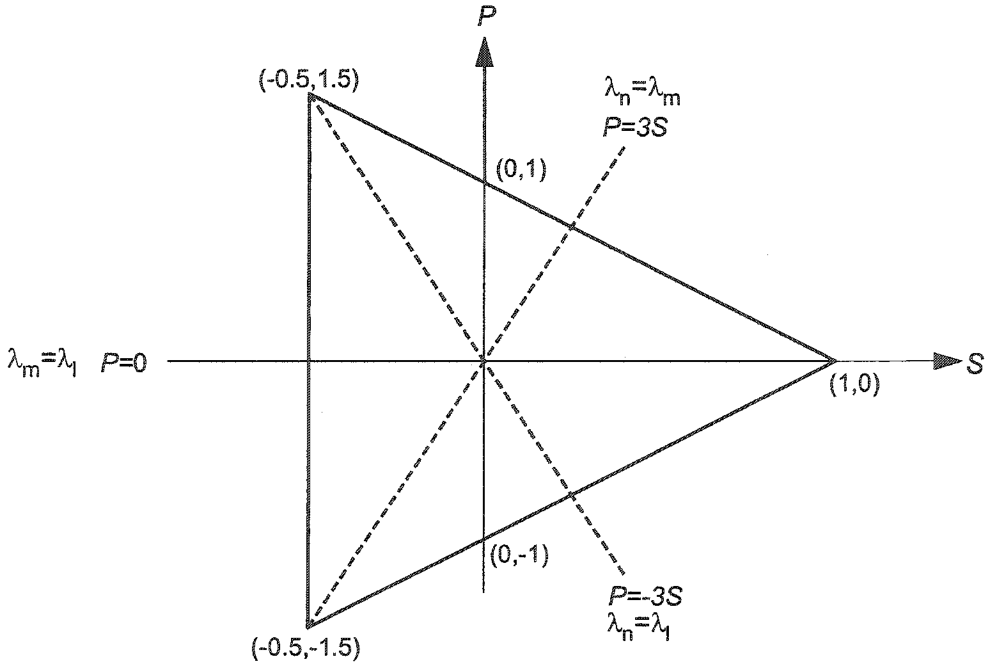

Figure 49: Orientation *S-P* triangle in terms of scalar order parameters *S* and *P*. Inside the triangle the orientation is biaxial (distinct eigen values), except on the uniaxial (two equal eigen values) lines $P= 0$, $P= +3S$, $P= -3S$.

The order parameter triangle *S-P* exhibits the following orientation fields:

(a) Isotropic orientation (three equal eigenvalues): $S = 0$ and $P = 0$.

(b) Uniaxial orientation (two equal eigenvalues): (i) $P = 0$ (horizontal full line through origin), (ii) $P= +3S$ (dashed line through the origin), and (iii) $P= -3S$ (dashed line through the origin)

A plot of the trajectory of *S* and *P* on the orientation triangle corresponding to planar radial (PR) texture with a +1 defect at the center is shown in figure 50 below.

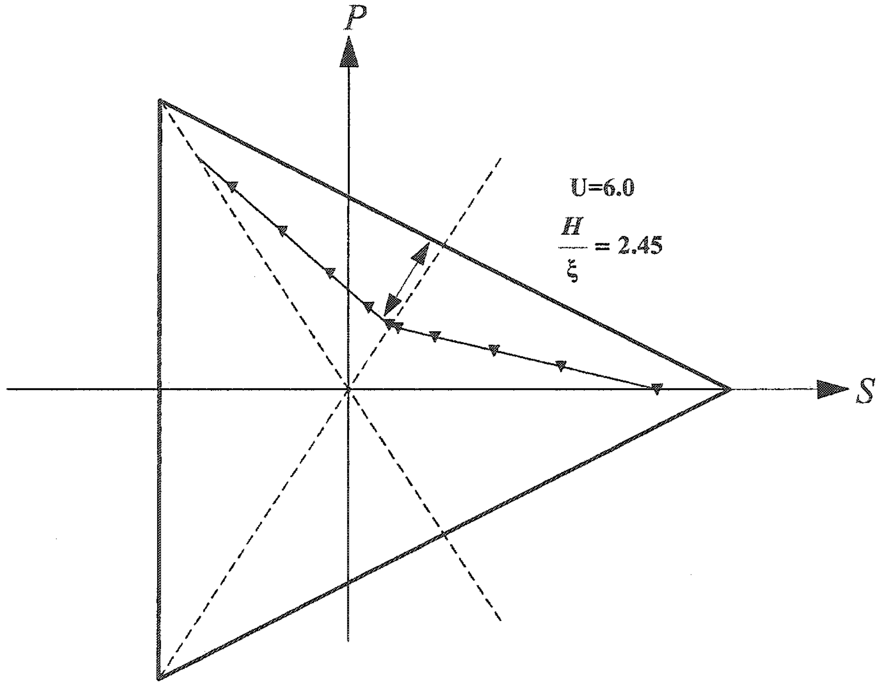

Figure 50: Plot of the trajectory of the scalar order parameter *S* across the fiber diameter of planar radial texture (for a +1 defect) plotted on the *S-P* triangle. The center of the defect (defect core center) always lies on the uniaxial line $P= 3S$.

It can be observed that the order parameter **Q** is uniaxial with a positive order parameter on one end of the fibre diameter and it goes to the other equivalent uniaxial state at the other end with negative order parameter through the mechanism of eigenvalue exchange [13]. It is apparent that the system takes the straight line path through the biaxial region with the defect center lying on the uniaxial line ($P= 3S$) through which the eigen value exchange occurs because on this line the two biggest eigen values are equal ($\lambda_n = \lambda_m$) and the distinguishing eigen value is λ_l. For a given U the point characterizing the scalar order parameters S and P moves along the uniaxial line $P = 3S$ and moving towards the isotropic point ($S = 0$, $P = 0$) as the value of nematic potential decreases. Next, using Doi's mesoscopic nematodynamic theory the dynamic equation for the tensor order parameter **Q** can be written as:

$$\frac{d\mathbf{Q}}{dt} = -6D\left\{\left(1-\frac{U}{3}\right)\mathbf{Q} - U\left(\mathbf{Q}\cdot\mathbf{Q} - \tfrac{1}{3}(\mathbf{Q}:\mathbf{Q})\boldsymbol{\delta}\right) + U(\mathbf{Q}:\mathbf{Q})\mathbf{Q}\right\} \tag{3.14}$$

After rewriting the eqn. (3.13) in the principal axes of **Q**, we obtain the following equations for the evolution of scalar order parameters S and P:

$$\frac{dS}{dt} = -\frac{2}{27}\left\{9S + U\left(P^2 - 3S + 2SP^2 - 3S^2 + 6S^3\right)\right\} \tag{3.15a, b}$$

$$\frac{dP}{dt} = -\frac{2}{27}\left\{9P - 9S + U\left(-3P - P^2 + 2P^3 + 3S + 6SP - 2SP^2 + 3S^2 + 6S^2P - 6S^3\right)\right\}$$

Phase plane analyses of the above equations were performed using standard procedure under the assumption that the unstable root would give the value of the scalar order parameter at the defect centre. The results of the phase plane analysis have been summarized in figure 51.

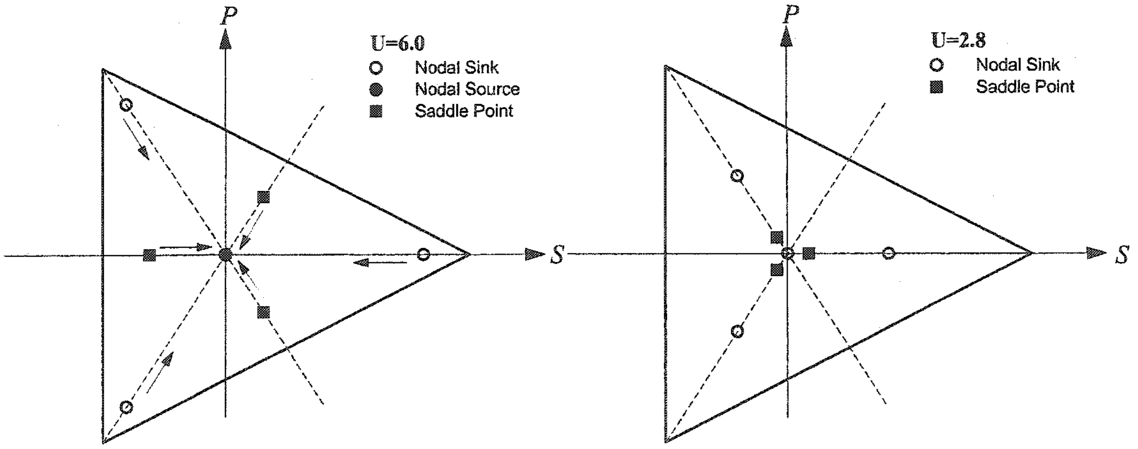

Figure 51: Phase plane analyses of eqn. (3.14a, b) are summarized in the two S-P triangle figures above. The direction of the arrows in the left figure indicates the direction in which the different solution points move as the value of U decreases. Another important change is that for U<3.0, the isotropic state ($S = 0$, $P = 0$) becomes a nodal sink as opposed to a nodal source for the value of U>3.0.

We obtain seven solution points from the phase plane analysis of the Eq. 3.14a, b. For U>3.0 there are three nodal sinks indicated by empty circles, three saddle points indicated by black squares and one source located at $S = 0$, $P = 0$. As indicated in figure 51 above the six solutions (nodal sinks and saddle points) converge towards the isotropic state ($S = 0$, $P = 0$) as we reduce the value of U=6.0.

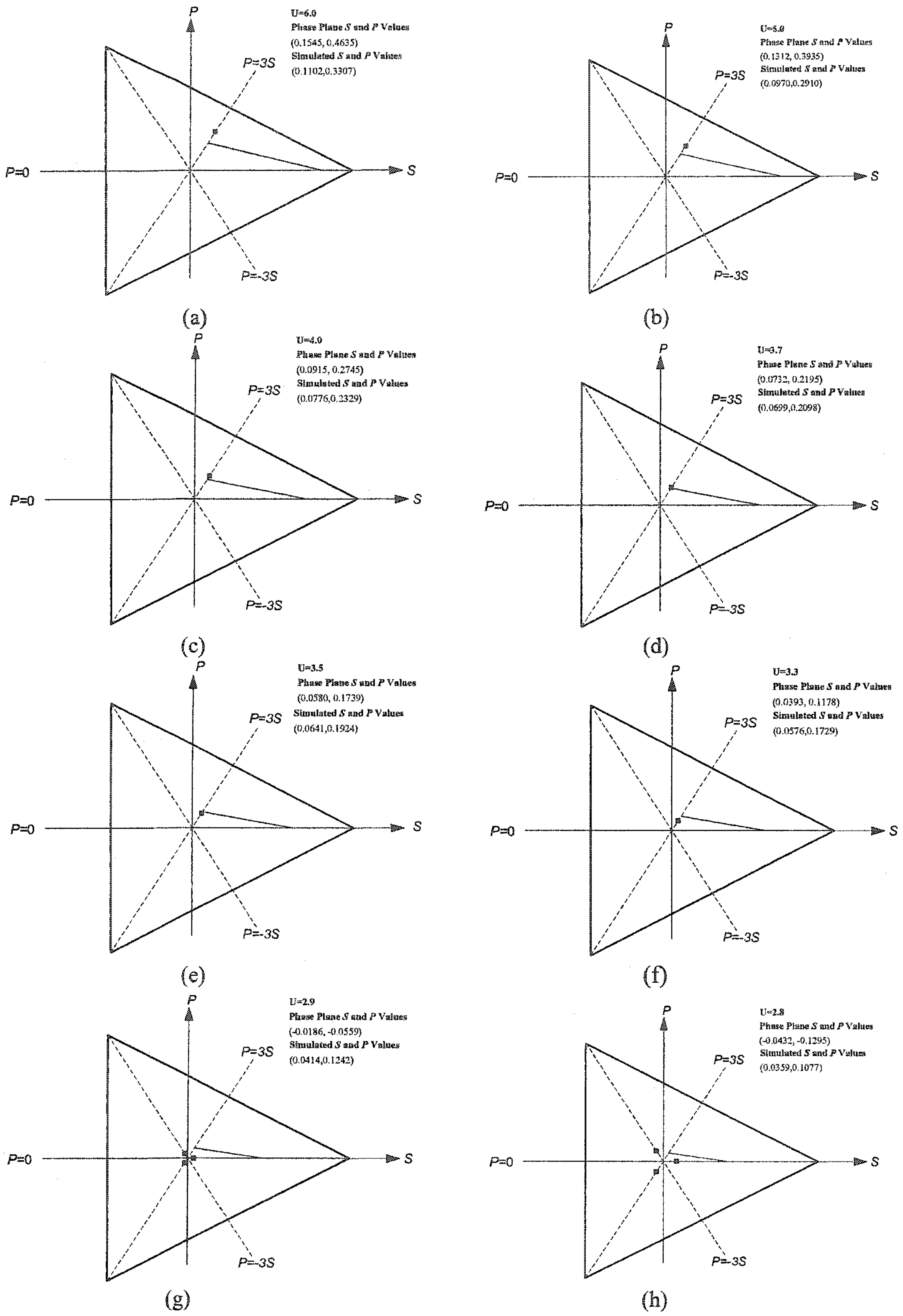

(a) (b)

(c) (d)

(e) (f)

(g) (h)

Figure 52: Comparison of the scalar order parameter values (*S* and *P*) at the defect core obtained from the simulation with the solutions obtained from the phase plane analysis. The best match occurs for 3.5<U<4. For U<3.0 we show all the three saddle points obtained from the phase plane analysis since the saddle point on the $P = 3S$ line attains negative values for *S* and *P*.

The value of U=3.0 is critical because as we decrease the value of U further, the isotropic solution changes from a nodal source to a nodal sink and furthermore the three saddle points go through the isotropic state and emerge on the other side of the origin of the *S-P* triangle. Next we compare the scalar order parameter values at the center of the defect obtained from the simulations with those obtained from the phase plane analysis.

The scalar order parameter values (*S* and *P*) at the defect center, obtained from the simulations are higher than those obtained from phase plane analysis for high values of U (i.e. for low temperature) as shown in figure 52. The predicted phase plane values for the order parameters match nicely with the simulated values for high temperature range (3.5 < U < 4). We also observe that phase plane analysis predicts the isotropic state as one of the possible stable solutions to our system for U<3.0 but simulation results indicate clearly that the defect core is never isotropic in nature. It has been mentioned that close to the defects our tensor order parameter deviates from uniaxiality and is increasingly biaxial in the region surrounding the defects. To quantify and visualize these highly strained localized biaxial regions, we utilize the parameter:

$$\beta^2 = 1\text{-}6\frac{\mathrm{tr}(\mathbf{Q}^3)^2}{\mathrm{tr}(\mathbf{Q}^2)^3} \tag{3.16}$$

The parameter β^2 has been used in [14, 15] for similar purposes. This parameter ranges in the interval [0, 1]. In all uniaxial states β^2=0 and a state with maximal biaxiality would correspond to β^2=1.In figure 53 we show a surface plot of the biaxiality parameter β^2 for a defect of strength +1. We show a cross-section across the fiber diameter for a more clear representation. In the figure as we move across the fiber diameter beginning from one end, the biaxiality parameter is zero (as the tensor order parmeter **Q** is uniaxial) and it increases as we move towards the center of the defect reaching a maximum value of 0.98 before eventually reducing to zero at the center of the carbon fiber (tensor order parameter **Q** again becomes uniaxial). The biaxiality parameter forms a kind of ring of maximal biaxiality around the defect and is termed as biaxial torus around nematic point defects in [14].

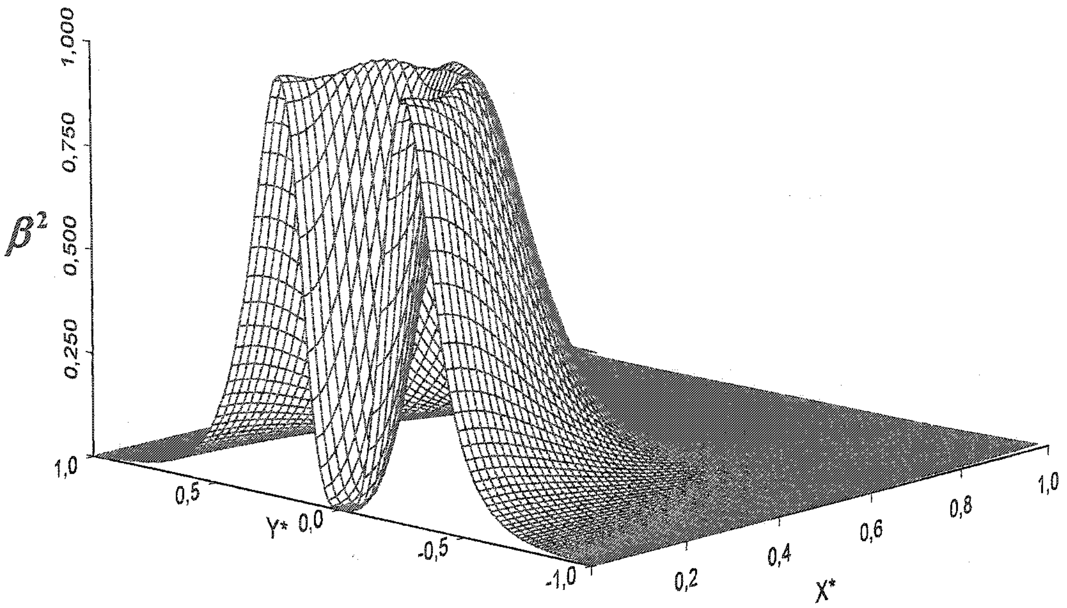

Figure 53: Surface plot of the biaxiality parameter β^2 across the fibre diameter with a +1 defect at the center of the fibre. The biaxiality parameter reaches a maximal value of 0.98 at approx. 1.2ξ and forms a kind of ring of maximal biaxiality around the defect. The Parametric values are U=2.80, $\frac{H}{\xi} = 10.0$, and L_2 = -0.5.

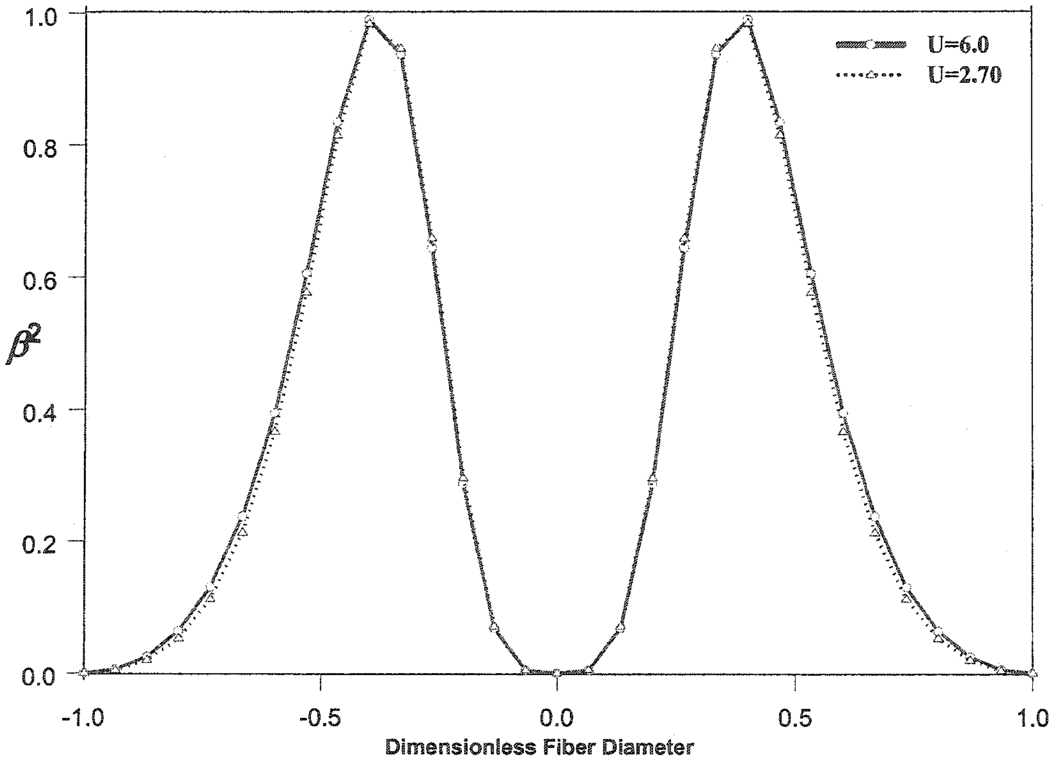

Figure 54: Plot showing β^2 across the fiber diameter for two different values of U. For small fiber radii there is no appreciable effect of temperature on the defect core size. The value of $\frac{H}{\xi} = 2.45$ for the above plot.

Next we look at the effect of temperature (nematic potential U) on the defect core structure. For this we have plotted the parameter β^2 across the fibre diameter for two different values of U. It is clearly apparent that for smaller fiber radius there is no significant effect of temperature on the defect core texture. The graphs for two different values almost overlap each other as shown in figure 54. On the other hand there is an increase in the defect core size with increase in temperature for high fiber radii[11] as shown in figure 55.

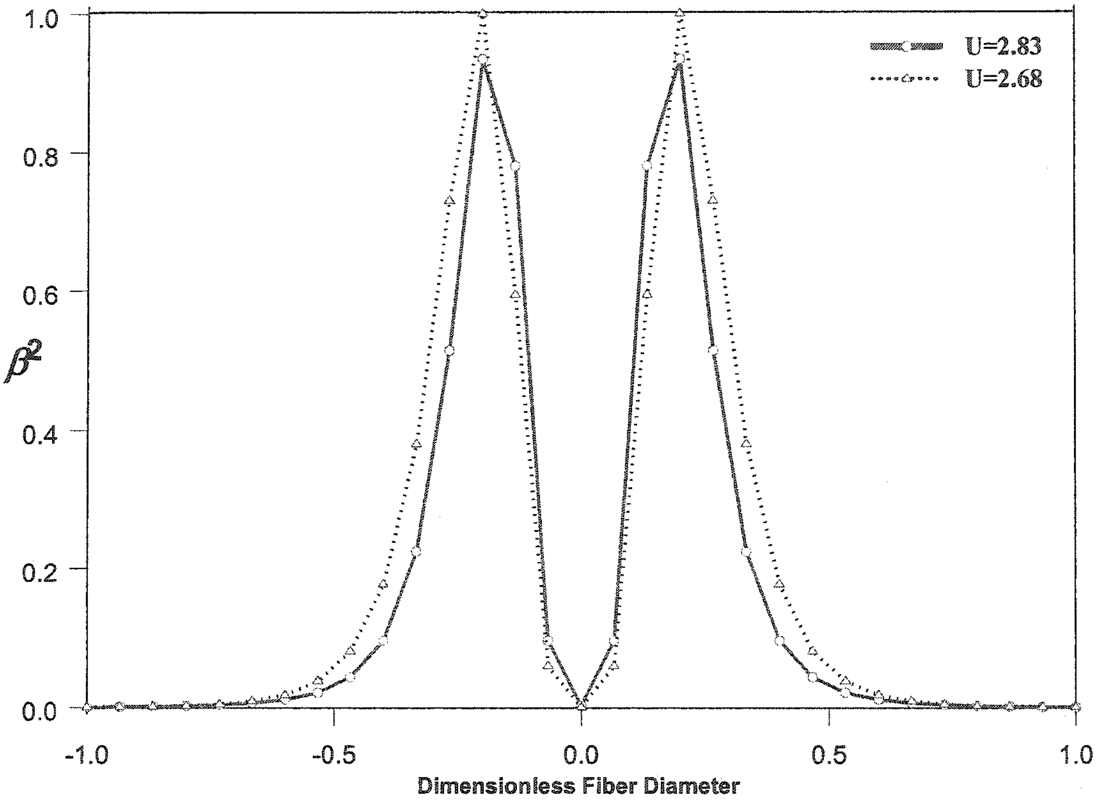

Figure 55: Plot showing β^2 across the fiber diameter for two different values of U at higher fiber radii than figure 54. There is a significant increase in defect core size with an increase in the temperature. $\frac{H}{\xi} = 10.0$.

Another interesting point to note is that the increase in the defect core is on the outside of the biaxial torus (there is an increase in the strained or the biaxial region) whereas the biaxial torus radii (the distance between the center and the maximal biaxiality ring) remains the same. We denote the distance between the center of the defect and the point of maximum biaxiality (i.e. biaxial radii torus) for a PR texture as r_b and look at the variation of this radius with the fiber size. The variation of the biaxial torus radii with fibre size is shown in figure 56.

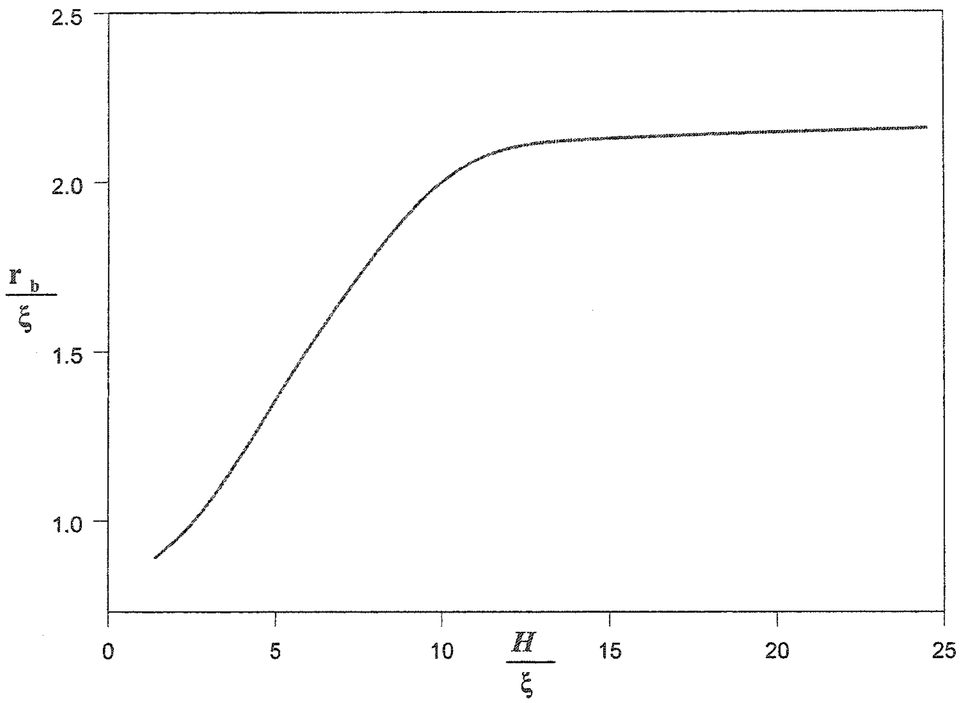

Figure 56: The influence of confinement on the characteristic biaxial torus radii r_b. This characteristic radius shows an asymptotic behavior.

The characteristic radius r_b increases linearly until $\frac{H}{\xi} \approx 10.0$ and after that it asymptotically reaches a value close to 2ξ. The results presented above qualitatively match the analytical results obtained in [14]. The results also indicate that the fiber radii has a strong effect on the core texture for smaller fiber radii. For fibers larger than $\frac{H}{\xi} \approx 10.0$, there is no effect of the fiber size on the defect core texture.

3.4 Conclusions

The results obtained from the numerical simulation of the governing Landau de Gennes mesoscopic theory have been presented in this chapter. The two characteristic textures, namely Planar Radial (PR) and Planar Polar (PP) were obtained from the simulations. A phase diagram showing the regions of favored textures was constructed. We do not observe regions of common textures (i.e. regions where both the textures PR and PP are stable) as obtained in [4] because we perform dynamical simulations. Instead, we get the texture with the lowest energy only. We also do not observe the so called Escaped Radial (ER) texture due to the simplifying assumptions of our model. The model can easily be used to simulate onion texture by changing the boundary condition from tangential molecular orientation to homeotropic molecular orientation although we only simulate PR and PP texture in this study. Next we analyzed the transient evolution of the PR and PP textures, in particular the various pathways that lead to the formation of the PP texture. This analysis was followed by the examination of the defect cores of defects of strength +1 and $+\frac{1}{2}$ with special emphasis on the defect of strength +1. In short, a detailed analysis of the PR and PP textures has been performed. This should provide us with a framework for practical application of this analysis to the real world fabrication of carbon fibers, where texture control and optimization of thermo-mechanical properties is required.

Bibliography

[1] Sonnet A., Kilian A., Hess S., *Phys. Rev. E*, **52** (1), 718 (1995).

[2] Doi M., Edwards S.F., *The Theory Of Polymer Dynamics* (Clarendon Press, Oxford 1987)

[3] Longa L., Monselesan D., Trebin H.R., *Liq. Cryst.*, **2** (6), 769 (1987)

[4] Davis T.A., Gartland (Jr.) E.C., *SIAM J. Numer. Anal.*, **35** (336) 1998

[5] Kralj S., Zumer S., *Phys. Rev. E*, **51**(1), 366 (1995)

[6] Edie D.D., *Private Communication*

[7] Davis T.A., *Finite Element Analysis of the Landau-de Gennes Minimization Problem for Liquid Crystals in Confinement,* Ph.D. Thesis, Kent State University, USA (1994)

[8] Chandrasekhar S., *Liquid Crystals*, 2nd Edition (Cambridge University Press, Cambridge, 1992)

[9] de Gennes P.G., Prost J., *The Physics of Liquid Crystals,* 2nd edition (Clarendon Press, Oxford, 1995)

[10] Schopohl N., Sluckin T.J., *Phys. Rev. Lett.*, **59** (22), 2582 (1987).

[11] Sigillo I., Greco F., and Marucci G., *Liq. Cryst.*, **24**(3), 419 (1998)

[12] Rey A.D., *Macromol. Theory Simul.*, **4**, 857(1995)

[13] Palffy-Muhoray P., Gartland E.C., Kelly J.R., *Liq. Cryst.*, **16** (4), 713 (1994)

[14] Kralj S., Virga E., Zumer S., *Phys. Rev. E*, **60** (2), 1858 (1999)

[15] Mkaddem S., Gartland (Jr) E.C., *Phys. Rev. E*, **62** (5) 6694 (2000)

Chapter 4

Effect of Elastic Anisotropy on the Defect Core

This chapter presents a rigorous analysis of the effect of elastic anisotropy on the defect core structure. A complete characterization of carbon fibers should include structure formation at the nano scale. Defect core sizes are in the nano-range and hence embodied structural features are found at these small scales. One of the most important features of the nano scale structure of defect cores is their sensitivity to elastic anisotropy. What follows provides a summary of the main order and orientation phenomena induced by elastic anisotropy at the nano scale.

4.1 Effect of Elastic Anisotropy (L_2) on the Defect Core Structure of +1 Defect

We will explore the effect of elastic anisotropy (L_2) on the core structure of both the defect types that we encounter in our texture formation process namely defect of strength +1 and defect of strength $+\frac{1}{2}$. We begin with the +1 defect before eventually moving onto the $+\frac{1}{2}$ defect. Figure 57 exhibits the three eigenvalues of the tensor order parameter profiles for three different values of L_2. The two main characteristics that are clearly apparent are the different pathways that the three eigenvalues take in traversing from the boundary to the center of the defect, and the higher values of the two scalar order parameters at the center of the defect as the value of (L_2) increases from -0.5 to 5.0. Although the values of the scalar order parameter (S and P) are higher, the tensor order parameter $\mathbf{Q}$ is still uniaxial at the defect core.

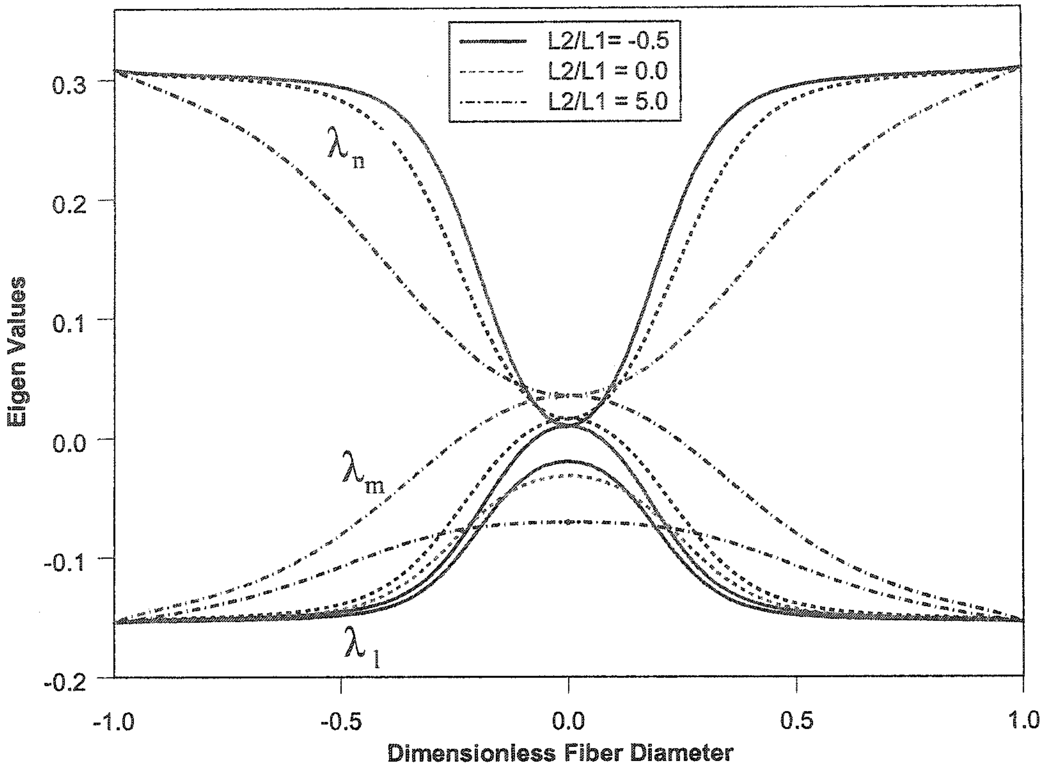

Figure 57: Plot showing the variation of the three eigenvalues across the fiber diameter. The three different sets of eigenvalue plots are for three distinct values of L_2. The values of the scalar order parameters S and P at the center of the defect increase as the value of L_2 is increased from -0.5 to 5.0. The tensor order parameter remains uniaxial at the center of the defect.

It is clearly apparent from the figure above that the slope of the principal eigen value connected to the director orientation decreases in the radial direction as we increase the value of L_2. This can be explained by looking at the long-range energy term associated with the elastic anisotropy parameter L_2 [see equation (2.18) of chapter 2]. Using equation (2.18) of Chapter 2 this term can be expressed in cylindrical coordinates as:

$$\left[\frac{2}{3}\frac{\partial S}{\partial r}+\frac{1}{r}\left(S-\frac{P}{3}\right)\right]^2 \qquad (4.1)$$

We see that this term contains two contributions. The first part contains the gradient of S in the radial direction and the second term controls the uniaxiality of the tensor order parameter at the center of the defect. As we increase the elastic anisotropy parameter, the cost of elastic deformation increases and the system tries to minimize the long-range energy for the same amount of deformation present (since the fiber texture still remains planar radial with a +1 defect at the center) by decreasing the gradient of the scalar order parameter S in the radial direction, or in other words increasing the biaxial region (decreasing the uniaxial region) around the defect center. In addition the second term diverges to infinity as $r \to 0$ leading to infinite long-range energy. Therefore $P = 3S$ at the center in order to keep the long-range energy finite and in turn maintaining the uniaxiality of the tensor order parameter at the center of the defect. As mentioned before, the system increases the region of biaxiality around the defect center as the value of the elastic anisotropy parameter increases. This implies that the defect core size of a defect of strength +1 increases with increase in the value of L_2.

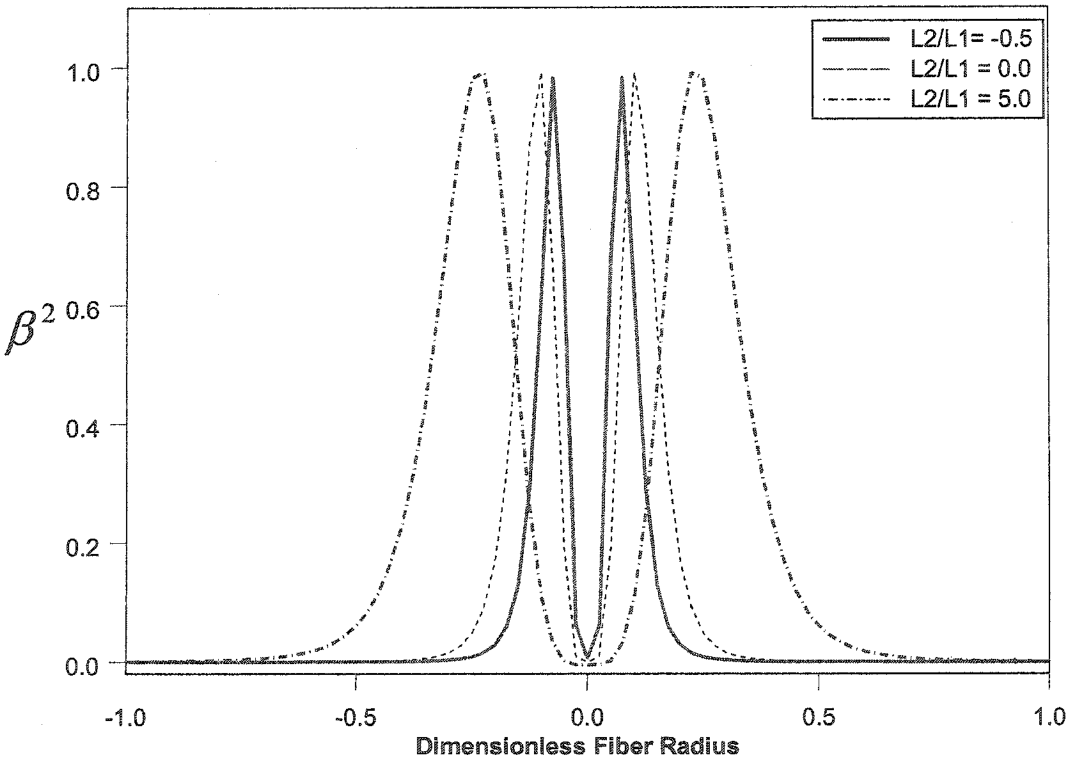

Figure 58: Plot showing the effect of elastic anisotropy parameter L_2 on biaxial region around a defect of strength +1.The two main effects of increase in the value of L_2 are increase in the defect core radius as well as an increase in the biaxial region around the defect with an increase in the value of L_2.

This is also clearly visible if we plot β^2 [biaxiality parameter, introduced and used in the previous chapter, see equation (3.14) in Chapter 3] across the fiber diameter of a planar radial texture for increasing L_2. Figure 58 shows the plot of β^2 across the fiber diameter for three different values of L_2. The peaks indicating a ring of maximal biaxiality (biaxial torus) around the +1 defect are observed to move further apart with an increase in the elastic anisotropy parameter L_2 indicating an increase in the defect core. Furthermore the maximal biaxiality peaks tend to lose their sharpness and become broader with increasing L_2. This clearly indicates an increase in the overall biaxial region for the planar radial (PR) texture. This increase in the biaxial region is an effort by system to minimize the long-range energy for the same deformation but with an increased penalty for the deformation with L_2 going from -0.5 to 5.0. Next we study the effects of elastic anisotropy on the planar polar (PP) texture and on the defect of strength $+\frac{1}{2}$.

4.2 Effect of Elastic Anisotropy (L_2) on the Defect Core Structure of $+\frac{1}{2}$ Defect

As mentioned in the previous chapters, the planar polar (PP) texture with it characteristic two $+\frac{1}{2}$ defects is the symmetry-breaking solution to our governing equation for certain parametric values (see, for example, figure 36 in Chapter 3). When we plot the contour plot of the variation of the scalar order parameter for a planar polar texture, the contour lines around the two $+\frac{1}{2}$ defects are elliptical in shape far away from the defect center as shown in figure 59. As we move inwards towards the center of the defect the contour lines become circular in shape. This would indicate different characteristic distances for the variation of scalar order parameter in two different directions. Thus, we chose to explore the effect of elastic anisotropy on the core of $+\frac{1}{2}$ defect for planar polar texture in two different directions. These two characteristic directions and the nomenclature used are explained in the caption for figure 60.

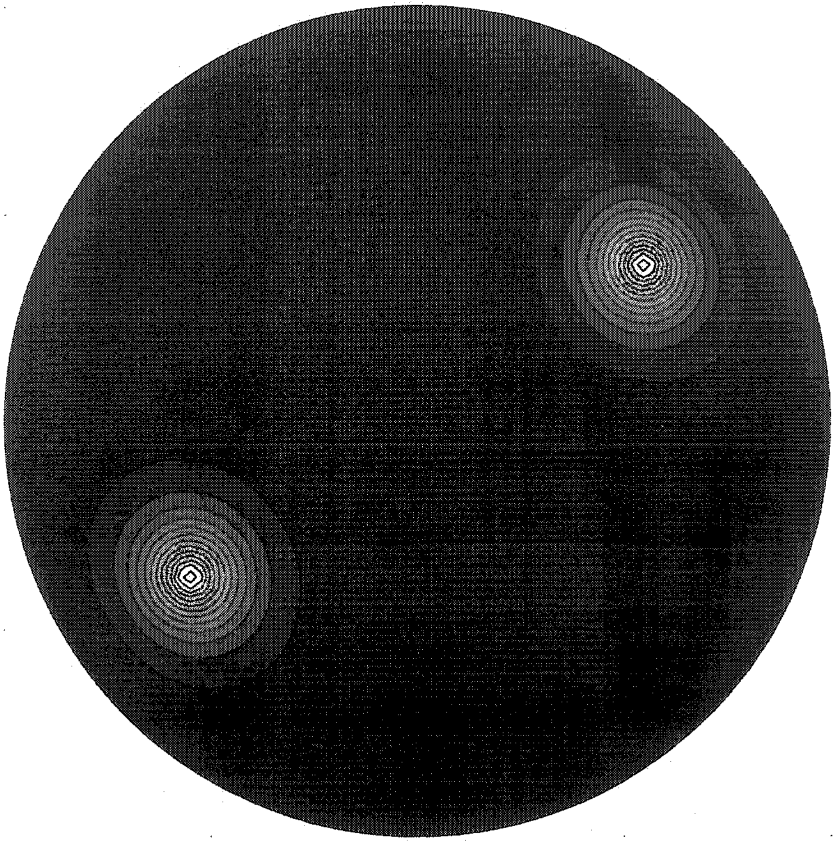

Figure 59: Contour plot of the variation of scalar order S for a planar polar texture. The elliptical shape of the contours is clearly visible far away from the defect center. As we move towards the center of the defect the contours take circular shape.

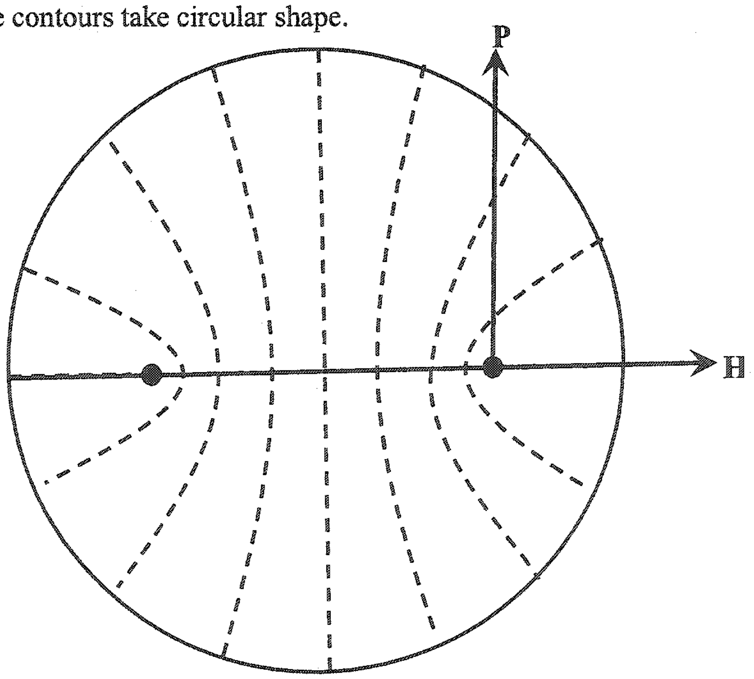

Figure 60: Schematic showing the two characteristic directions that we use to explore the effect of elastic anisotropy (L_2) for planar polar texture. The line starting from one end and joining the two defects is taken as horizontal direction represented by H and the direction perpendicular to this direction is taken as the perpendicular direction represented by P.

The line joining the two $+\frac{1}{2}$ defects in the planar polar texture is taken as the horizontal direction and represented by H in figure 60. The other direction P is perpendicular to the horizontal direction H and passing through one of the defects as shown. Now we start the analysis of the planar polar texture by presenting a plot of the set of three eigenvalues of the tensor order parameter for three different values of elastic anisotropy parameter (L_2).

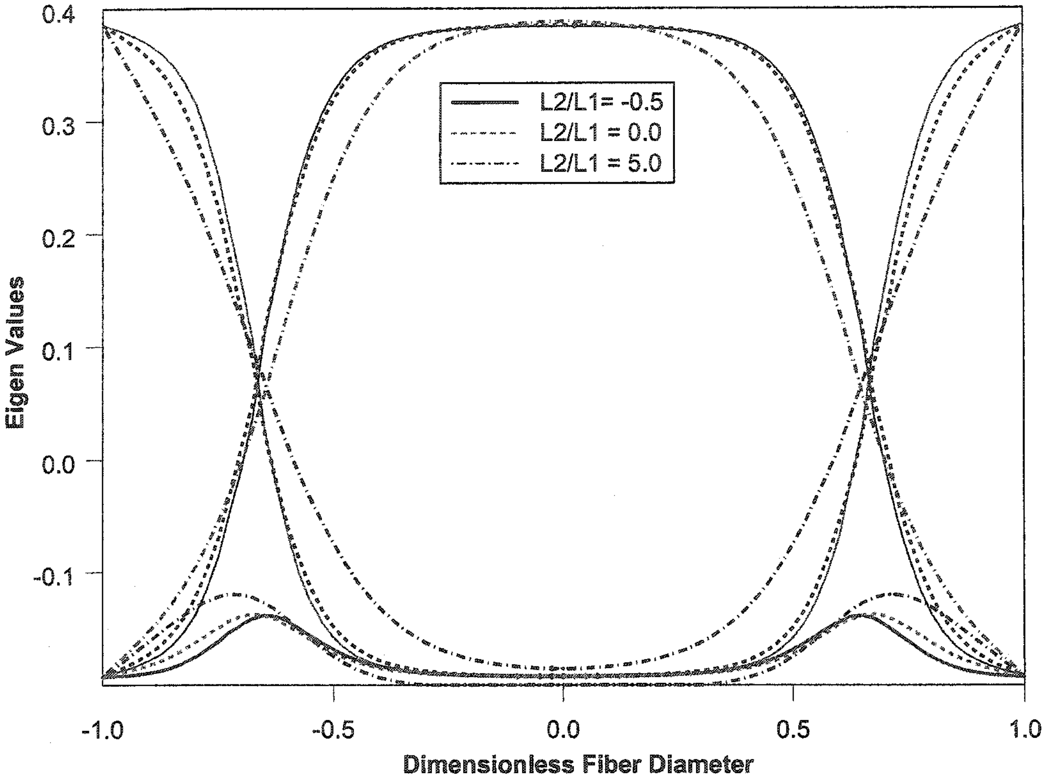

Figure 61: Plot showing the variation of the three eigenvalues across the fiber diameter for a planar polar texture. With increasing value of L_2 the three eigenvalues indicate an increase in defect core radius and increase in biaxial region similar to that for +1 defect of the PR texture but with an important difference that the scalar order parameter values S and P at the defect center do not change with changes in L_2.

The variation of eigenvalues in the horizontal direction for planar polar texture for three different values of elastic anisotropy parameter (L_2), as shown in figure 61, indicates two phenomena similar to that seen for the planar radial (+1 defect) texture namely an increase in the defect core radius and an increase in the biaxial region around the defect with an increase in the value of L_2. In addition, there is an important difference in that the values of scalar order parameters S and P at the defect center do not change with a change in the value of L_2. Using equation (2.18) of Chapter 3 the term relating to the elastic anisotropy contribution in the long-range free energy for $+\frac{1}{2}$ defect can be written in cylindrical coordinates as:

$$\left[\frac{\partial S}{\partial r}\left(\frac{\cos\theta}{2}+\frac{1}{6}\right)-\frac{1}{3}\frac{\partial P}{\partial r}\left(\frac{1}{2}+\frac{\cos\theta}{2}\right)+\frac{1}{r}\left(S-\frac{P}{3}\right)\left(\frac{\cos\theta}{2}\right)\right]^2 + \left[\frac{\partial S}{\partial r}\left(\frac{\sin\theta}{2}\right)-\frac{1}{3}\frac{\partial P}{\partial r}\left(\frac{\sin\theta}{2}\right)+\frac{1}{r}\left(S-\frac{P}{3}\right)\left(\frac{\sin\theta}{2}\right)\right]^2 \tag{4.2}$$

In the above expressed term as $r \rightarrow 0$ S and P are independent of the azimuthal direction and only depend on r. The above term, unlike that for +1 defect, depends on the gradient of the biaxial order parameter P in the radial direction in addition to the gradient of S. This term contains the sum of the squares of these two gradients $\left(\left(\frac{\partial S}{\partial r}\right)^2 \text{ and } \left(\frac{\partial P}{\partial r}\right)^2\right)$ and a decrease in the gradient of S will lead to an increase in the gradient of P to fulfill the uniaxiality of the tensor order parameter at the center of the defect. Therefore, in the case of $+\frac{1}{2}$ defect, the system does not realize any benefit by changing the scalar order parameter values at the defect core. The only effects of increasing L_2 are therefore an increase in the defect core and the biaxial region around the defect, as shown in the plot of the biaxiality parameter in the horizontal direction in figure 62(In the figure the biaxiality parameter does not reach zero at the defect core due to lack of computation precision) for three different values of L_2. Another interesting phenomenon that is not apparent by looking at the variation the eigenvalues (but is clearly visible from the biaxiality parameter plot) along the horizontal direction is that increase in the defect core and the biaxial region is unidirectional. In other words, there is no perceptible increase in the defect core and the biaxial region that is closer to the carbon fiber boundary but all the changes in the defect core and biaxial region occur towards the center region of the fiber. This is due to the fact that we have used a fixed boundary condition (strong anchoring at the boundary). This does not allow the effects on the defect core structure to diffuse towards the boundary and limits them to only one side.

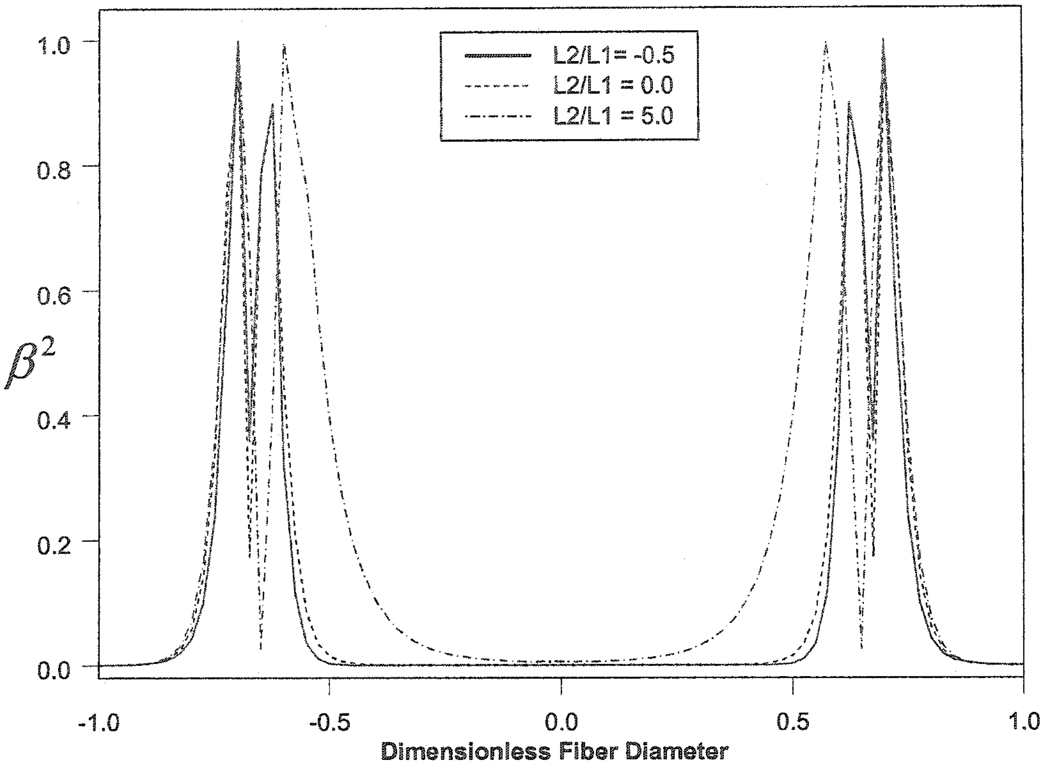

Figure 62: Plot showing the effect of elastic anisotropy parameter L_2 on biaxial region around a defect of strength $+\frac{1}{2}$ for a planar polar texture. We can clearly observe that all the effects on the defect core due to increase in the value of L_2 from -0.5 to 5.0 are confined to only one side of the defect.

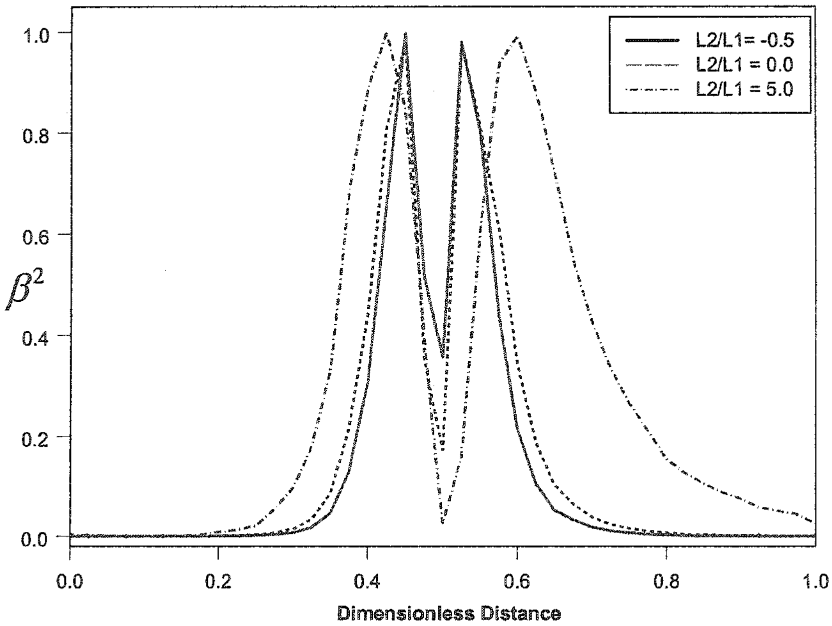

Figure 63: Plot showing the effect of elastic anisotropy parameter L_2 in the perpendicular direction of the defect of strength $+\frac{1}{2}$ for a planar polar texture. The effects of the changes in L_2 from -0.5 to 5.0 are more even about the defect in this direction.

In contrast, the effects of the increase in elastic anisotropy parameter L_2 are more symmetrical about the defect in the perpendicular direction as compared to the horizontal direction due to the fact that boundary effects become less pronounced in the perpendicular direction. The plot of the biaxiality parameter β^2 in the perpendicular direction is given in figure 63. This completes our analysis of the effect of elastic anisotropy parameter L_2 the defect core of defects of strength $+1$ (planar radial texture) and $+\frac{1}{2}$ (planar polar texture). We end this chapter by summarizing our results.

4.3 Conclusions

A basic nanoscopic analysis of the effects of elastic anisotropy (L_2) has been performed for both the planar radial and planar polar textures. The two main effects observed for increased elastic anisotropy are increase in the defect core size as well as increase in the biaxial region around the defect for defects of both strength $+1$ (planar radial texture) and $+\frac{1}{2}$ (planar polar texture). Both these effects are due to the increased cost of elastic deformation as a result of increase in elastic anisotropy. The increase in the scalar order parameter (S and P) has been explained for $+1$ defect. On the contrary, the scalar order parameter values at the defect core do not change for defects of strength $+\frac{1}{2}$ due to the fact that the system does not gain any advantage by increasing these values. Although this is in no way a complete analysis of the elastic anisotropy effects on the defect core due to the computation limitations involved, we expect that the observations made from the above results hold true in a more general sense. More detailed analysis would serve to add more details to these observations.

Chapter 5

Conclusions

A multi-scale model of texture formation in mesophase carbon fibers based on the Landau de-Gennes equations has been formulated, solved, and validated. The model is able to reproduce frequently observed textures in the industrial spinning of mesophase carbon fibers. The solution to our model predicts two commonly observed textures, namely planar radial (PR) and planar polar (PP). A phase diagram showing the regions of stability for the PR and PP texture has been constructed. A comprehensive analysis of the transient process of texture formation reveals three different pathways to the formation of planar polar textures: (a) defect splitting, (b) direct nucleation of two defects, and (c) multiple defect annihilation. These findings provide a means to predict and control the cross-section of mesophase carbon fibers through control of temperature, time and fiber radii. A comprehensive analysis of the defect core structure for a defect of strength +1 has also been undertaken and the results are in conformance with the published literature. The effects of temperature and fiber radii on the defect core texture of a +1 defect have been well characterized, the main effects being that the defect core radius increases with increase in the fiber radii. Temperature has no effect on the defect core for thinner fibers whereas for thicker fibers the defect core increases with increase in temperature. A basic analysis of the effect of elastic anisotropy on the defect core texture of defects of strength +1 and $+\frac{1}{2}$ has also been performed. This analysis has provided us with some interesting insights that could form the basis for future work involving a much more detailed analysis of the defect core texture for various types of defects. Although the Landau de-

Gennes mesoscopic model has worked well for our simulations, it is not without its drawbacks. The model contains a coupling of the form:

$$f_{\text{bulk}} + \left(\frac{\xi}{\mathrm{H}}\right)^2 \times f_{\text{elastic}} \tag{5.1}$$

Where ξ is the intrinsic length scale and H is the geometric length scale of the model, and f_{bulk} and f_{elastic} are namely the ordering potential and elastic forces contributions. Therefore for $\frac{\xi}{\mathrm{H}} \rightarrow 0$ the system becomes ill-conditioned as there is no elasticity, no penalty associated with spatial variations in the director field. Only the ordering potential remains, which only coerces a certain degree of order. Another aspect that needs more attention is the choice of numerical methods. Although implicit numerical schemes are the natural choice for stiff problems such as the one we deal with in this work, they have an inherent computational cost that prevents a high spatial resolution. On the other hand, the explicit numerical methods require relatively low computational power but suffer from stability concerns, which render them ineffective for stiff problems. Thus a good compromise would be to have the best of both the worlds i.e. stability and low computation cost. For this purpose a stabilized explicit method like Runga Kutta Chebyshev would enable us to increase the performance of our integration scheme (time and space). This would enable us to do a more comprehensive analysis for certain aspects of our work where we have faced computational limitations.

The numerical results obtained from this work provide a better understanding of the texture transformation in carbon fibers of circular cross-section. This knowledge should enable us to better control transient evolution and the final fiber texture. This work also lays the foundation for more detailed future work into defect core texture and the effects of various parameters on the defect core texture with better and more refined numerical schemes that reduce our computational cost. This work could also act as a stepping stone for texture analysis of the newly emerging field of nano fibers and nano scale phenomena in carbon fibers.